

LBL--14774

DE83 003395

**HIGH-RESOLUTION ELECTRON-ENERGY-LOSS SPECTROSCOPY AND
PHOTOELECTRON-DIFFRACTION STUDIES OF THE GEOMETRIC STRUCTURE
OF ADSORBATES ON SINGLE-CRYSTAL METAL SURFACES**

Daniel Henry Rosenblatt

Ph.D. Thesis

**Materials and Molecular Research Division
Lawrence Berkeley Laboratory
and
Department of Chemistry
University of California
Berkeley, California 94720**

November 1982

DISCLAIMER

This report was prepared as an account of work sponsored by an agency of the United States Government. Neither the United States Government nor any agency thereof nor any of their employees, makes any warranty, express or implied, or assumes any legal liability or responsibility for the accuracy, completeness, or usefulness of any information, apparatus, product, or process disclosed, or represents that its use would not infringe privately owned rights. Reference herein to any specific commercial product, process, or service by trade name, trademark, manufacturer, or otherwise, does not necessarily constitute or imply its endorsement, recommendation, or favoring by the United States Government or any agency thereof. The views and opinions of authors expressed herein do not necessarily state or reflect those of the United States Government or any agency thereof.

This work is supported by the Director, Office of Energy Research, Office of Basic Energy Sciences, Chemical Sciences Division of the U. S. Department of Energy under Contract No. DE-AC03-76SF00098. It was performed in part at the Stanford Synchrotron Radiation Laboratory, which is supported by the NSF through the Division of Materials Research.

DISTRIBUTION OF THIS DOCUMENT IS UNLIMITED

TABLE OF CONTENTS

ABSTRACT.	vii
I. INTRODUCTION.	1
A. Electron Energy Loss Spectroscopy	3
B. Photoelectron Diffraction	8
References.	20
Figure Caption.	22
Figure.	23
PART I. ELECTRON ENERGY LOSS SPECTROSCOPY	24
II. DESIGN AND PERFORMANCE OF A HIGH RESOLUTION ELECTRON ENERGY LOSS SPECTROMETER	25
A. Design Criteria	25
B. Description of the EELS Spectrometer.	27
1. Vacuum Chamber and Shielding.	27
2. Electron Monochromator.	31
3. Electron Energy Analyzer.	38
4. Power Supplies.	43
5. Pulse Counting and Data Acquisition Electronics .	48
6. Tuning Procedure.	49
7. Software and Spectrum Generation.	54
C. Performance	56
References.	59
Tables.	60
Figure Captions	62
Figures	63

III. EELS STUDY OF OXYGEN ADSORBED ON Cu(001)	74
A. Introduction	74
B. Experimental	75
C. Results and Discussion	76
References	85
Figure Captions.	87
Figures.	88
 PART II. PHOTOELECTRON DIFFRACTION	 90
IV. NORMAL PHOTOELECTRON DIFFRACTION OF c(2x2)O(1s)-Ni(OCl) AND c(2x2)S(2p)-Ni(001), WITH FOURIER-TRANSFORM ANALYSIS.	91
A. Introduction	91
B. Experimental	92
C. Results and Discussion	95
1. The c(2x2) Oxygen Overlayer.	96
2. The c(2x2) Sulfur Overlayer.	103
D. Fourier-Transform Analysis	105
E. Conclusions.	111
References	112
Figure Captions.	116
Figures.	117
V. NORMAL PHOTOELECTRON DIFFRACTION STUDIES OF SELENIUM AND SULFUR OVERLAYERS ON Ni(011) and Ni(111)	129
A. Introduction	129
B. Experimental	130
C. Theory	132

D. Results and Discussion	132
1. Selenium Overlayers on Ni(111).	132
2. The c(2x2) Selenium and Sulfur Overlayers on Ni(011)	139
E. Conclusions.	141
References	142
Figure Captions.	144
Figures.	145
VI. OFF-NORMAL PHOTOELECTRON DIFFRACTION STUDY OF THE c(2x2) SELENIUM OVERLAYER ON Ni(001)	152
A. Introduction	152
B. Experimental	153
C. Theory	154
D. Results and Discussion	156
E. R-Factor Analysis.	160
F. Conclusions.	161
References	163
Figure Captions.	165
Figures.	166
VII. STRUCTURAL DETERMINATION OF A MOLECULAR OVERLAYER SYSTEM WITH NORMAL PHOTOELECTRON DIFFRACTION: c(2x2)CO-Ni(001).	171
A. Introduction	171
B. Experimental and Theory.	171
C. Results and Discussion	173
References	177
Figure Captions.	178
Figures.	179

VIII. CONCLUDING REMARKS.	183
A. Recommendations for the Future: Electron Energy Loss Spectroscopy	183
B. Recommendations for the Future: Photoelectron Diffraction	190
References.	194
Table	196
ACKNOWLEDGEMENTS	197

HIGH RESOLUTION ELECTRON ENERGY LOSS SPECTROSCOPY AND
PHOTOELECTRON DIFFRACTION STUDIES OF THE GEOMETRIC STRUCTURE
OF ADSORBATES ON SINGLE CRYSTAL METAL SURFACES

Daniel Henry Rosenblatt

Materials and Molecular Research Division
Lawrence Berkeley Laboratory
and
Department of Chemistry
University of California
Berkeley, CA 94720

ABSTRACT

Two techniques which have made important contributions to the understanding of surface phenomena are high resolution electron energy loss spectroscopy (EELS) and photoelectron diffraction (PD). EELS is capable of directly measuring the vibrational modes of clean and adsorbate covered metal surfaces. In this work, the design, construction, and performance of a new EELS spectrometer are described. The initial experiment carried out with the spectrometer was a study of submonolayer coverages of oxygen on Cu(001). A complex evolution of the O-Cu stretching vibration peak was observed as a function of coverage. These results are discussed in terms of possible structures of the O-Cu(001) system. Recommendations for improvements in this EELS spectrometer and guidelines for future spectrometers are given.

PD experiments provide accurate quantitative information about the geometry of atoms and molecules adsorbed on metal surfaces. In an energy-dependent PD experiment, the angle-resolved photoemission cross-section of a core level on an adsorbate atom is measured as a func-

tion of photon energy. The technique has advantages when used to study disordered overlayers, molecular overlayers, multiple site systems, and adsorbates which are weak electron scatterers. Four experiments were carried out which exploit these advantages. In three of the experiments, data were collected normal to the sample face. First, the structure of the $c(2 \times 2)$ oxygen and sulfur overlayers on Ni(001) was determined. R-factor analysis was used to verify the precision of the results. Fourier-transform analysis was also carried out to obtain certain structural parameters. Second, the structure of selenium on Ni(111) and on Ni(011) was ascertained for the first time. The third normal emission study yielded the structure of carbon monoxide adsorbed on Ni(001). Finally, a study of $c(2 \times 2)$ Se on Ni(001) was done at emission angles away from the normal direction. The derived structure was the same as the result of an earlier study at normal emission. A comparison between PD and other techniques is made and a discussion of very recent developments in PD is given.

I. INTRODUCTION

The field of surface science has been growing rapidly for the last ten years. One of the areas which has been extremely active is that of surface structure determination. Most of the recent work has concentrated on the determination of highly accurate geometric structures of atoms and very small molecules on metal single crystal surfaces. The bulk of our knowledge of these surface structures has been obtained using the techniques of low energy electron diffraction (LEED),¹ surface extended x-ray absorption fine structure (SEXAFS),² and photoelectron diffraction (PD).³ In addition to the quantitative studies, there has also been a great deal of emphasis on qualitative structural techniques which are often able to provide information about bonding sites and molecular orientation without actually yielding bond distances. An example of a qualitative structural technique is electron energy loss spectroscopy (EELS).⁴ Often, EELS can be used to partially corroborate or even complement the information obtained from LEED, SEXAFS, and PD. It can be especially useful in cases where the surface structure is complex, e.g., multiple site adsorption, surface oxidation, and the adsorption of large molecules such as hydrocarbons. EELS is also quite sensitive to the presence of hydrogen on the surface, unlike the other techniques mentioned. Recently, EELS has been used to obtain quantitative structural information,⁵ but it is uncertain whether it will be widely used to determine accurate structures in the future.

In this thesis, I report the results of some accurate structural studies using photoelectron diffraction and some electron energy loss

spectroscopy work which has provided some insight into the structure of a controversial adsorbate/substrate system. The bulk of the work described here is experimental in nature. Consequently, a great deal of attention will be paid to experimental details, with a lesser emphasis on theory. The rest of Chapter I will be devoted to a description of the EELS and PD techniques and the motivation behind the experiments in the succeeding chapters.

The main body of this thesis is divided into two parts. Part I (Chapters II and III) is concerned with electron energy loss spectroscopy. In Chapter II, the design and construction of a high-resolution electron energy loss spectrometer is described in detail. Special attention is paid to the design criteria and performance of this new spectrometer. In Chapter III, the initial experiment carried out with the EELS spectrometer is described. In that experiment, system of oxygen adsorbed on Cu(001) was studied in the specular and off-specular scattering directions.

In Part II (Chapters IV through VII), results obtained from photoelectron diffraction experiments carried out at the Stanford Synchrotron Radiation Laboratory (SSRL) are presented. In Chapter IV, the determination of the surface structure of c(2x2) overlayers of oxygen and sulfur on Ni(001) by normal photoelectron diffraction (NPD) is discussed. The case of oxygen on Ni(001) is emphasized due to the present controversy over its structure. Chapter V contains a description of NPD studies of two adsorbate/substrate systems with hitherto unknown structures: selenium on Ni(111) and on Ni(011). Chapter VI presents the first structure determination by off-normal emission,

energy-dependent photoelectron diffraction. The system chosen for this off-normal study was $c(2 \times 2)\text{Se-Ni}(001)$, which has a well-known structure. In Chapter VII, the use of NPD to determine the structure of a molecular adsorbate (carbon monoxide) on $\text{Ni}(001)$ is described. In Chapter VIII, some conclusions about this research are given. Most of the chapter is devoted to a discussion of the futures of PD and EELS from both a general (the field as a whole) and a specific (our research group's experimental effort) standpoint.

A. ELECTRON ENERGY LOSS SPECTROSCOPY

The technique of electron energy loss spectroscopy of metal surfaces has provided a great deal of information about vibrations of the surface lattice as well as those of adsorbed species.⁴ Both surface phonons and adsorbate vibrations occur in the infrared energy range, which is 25–400 meV or 200–3200 cm^{-1} ($1 \text{ meV} = 8.0655 \text{ cm}^{-1}$). Surface vibrational transitions can be observed with optical infrared spectroscopy, EELS, or several other techniques. Due to the high surface sensitivity of electron spectroscopy and improvements in the design of electron optics, EELS has become widely used in recent years.

To briefly describe the EELS technique, I will discuss the mechanics of the electron scattering experiment. A schematic of our EELS experimental setup is shown in Fig. 1. The experiment is carried out in an ultra-high vacuum chamber to maintain a high degree of sample purity during data collection. A number of power supplies are used to provide focusing voltages to the spectrometer. A beam of electrons is generated by a filament and monochromatized by an electron monochrom-

ator. The well-collimated, monoenergetic beam then impinges on the sample, which is usually a single crystal metal surface which may be clean or adsorbate covered. The monochromatic beam reflects off the sample, and in the process of scattering, some of the electrons lose a small amount of their energy by exciting vibrational modes of the surface. The portion of the beam which scatters at a particular angle (determined by the experimenter) enters the electron energy analyzer. A spectrum is taken by scanning the kinetic energy of electron detection and counting the number of electrons detected at each kinetic energy sampled. The generation of digital EELS spectra is controlled by a dedicated LSI-11/2 microprocessor. The microprocessor is interfaced to a number of data storage and display devices referred to here as the data acquisition electronics.

Much of the development of high resolution EELS as an important technique in surface science has been accomplished by Ibach and co-workers.⁴ Ibach has contributed significantly to the experimental development of EELS in general. In particular, he has utilized the 127° cylindrical sector to obtain high resolution (4-5 meV FWHM in the elastic peak) and extremely low background.⁶ The major theoretical advances have been made by Mills and co-workers. Evans and Mills have shown that specular (angle of incidence equals angle of reflection) inelastic scattering is dominated by the interaction of the incident electron with the long-range dipole moment of the oscillating surface vibrational modes.⁷ This leads to the so called "dipole selection rule," which states that only those vibrations with a component of their dynamic dipole moment normal to the surface can be excited

during specular scattering. This is because the vibrating perpendicular dipole creates an image dipole in the substrate which reinforces it. Parallel dipole transitions are forbidden, because the dipole field due to the dynamic dipole moment parallel to the surface is effectively cancelled by its image dipole field in the surface. Consequently, this selection rule may be used to determine adsorbate symmetry with respect to the surface. The theory of Evans and Mills also indicates that dipole scattering is strongly peaked in the specular direction.

More recent experimental⁸ and theoretical⁹ work has shown that there is a short-range "impact scattering" mechanism in addition to the long-range dipole interaction. Impact scattering transitions are better observed at non-specular scattering angles, although they are usually present with roughly the same intensity on specular. If care is taken to correctly assign all observed modes as dipole or impact in nature, qualitative information about bonding geometry, such as adsorption sites, can be obtained in favorable cases. In addition to the symmetry information which can be derived from the dipole selection rule, selection rules are believed to operate in the impact scattering regime as well.⁹ These rules may allow the experimenter to assign parallel vibrations to one of two mutually orthogonal directions parallel to the surface, leading to further structural information.

A quantitative structural determination has resulted from theoretical work by Rahman, Black, and Mills.⁵ They developed a lattice-dynamical model of the $p(2 \times 2)$ and $c(2 \times 2)$ overlayers of oxygen on

Ni(001), and used this model to calculate EELS spectra of these two oxygen on Ni(001) systems for various trial geometries. For both the p(2x2) and c(2x2) cases, they were able to determine the oxygen-nickel perpendicular distance by varying the adsorbate geometry in their calculations until they optimized the fit between theoretical and experimental EELS spectra. This work represents the first attempt at a structure determination using EELS data, and demonstrates its potential as an accurate structure-sensitive tool. Their results disagree with those from three diffraction techniques, however (see Chapter IV).

The first experiments which provided surface vibrational information were done with infrared light. Many of these early experiments measured the infrared transmission spectrum of carbon monoxide adsorbed on high surface area metal samples supported on silica.¹⁰ Infrared absorption by the CO stretching vibrational mode was observed, but lower frequency modes were completely hidden because of light absorption by the support. Later experiments on single crystals and evaporated films had to be carried out in the reflection mode. In an infrared reflection spectroscopy (IRS) experiment, it is necessary to measure small changes (due to absorption) in the infrared intensity reflected off the surface. Consequently, background noise has obscured most vibrational absorption peaks in many IRS experiments. Most of the successful IRS experiments have been carried out on carbon monoxide monolayers, as CO has a strong infrared-active stretching vibration. Recent IRS studies of CO adsorbed on single crystalline metals have observed the CO stretch with very high resolution but have been unable to resolve the carbon-nickel stretching vi-

bration ($<500 \text{ cm}^{-1}$) or any other low frequency vibrational mode.¹¹ Recent improvements in IRS and other optical techniques should help to overcome these difficulties. In IRS experiments, both wavelength and polarization modulation have been used to reduce the effects of fluctuations in the infrared beam and to improve surface sensitivity.¹² Recently, Richards and co-workers¹³ have developed a thermal detection spectrometer capable of measuring small absorptions in the frequency range $1000\text{--}3000 \text{ cm}^{-1}$. Thermal emission of infrared radiation from a vibrational mode of CO adsorbed on Ni has been observed as well.¹⁴ Surface Raman scattering¹⁵ is also promising, especially if multichannel optical detection is used to improve sensitivity.¹⁶

In EELS, only a small fraction of the reflected electrons have caused vibrational transitions. These inelastically scattered electrons leave the sample with a different energy than the rest of the beam, and can be isolated from the elastic electrons by the energy analyzer. Therefore, the signal-to-background ratio of the inelastic losses is quite high. This has enabled EELS spectrometers to measure loss peaks over the entire infrared frequency range. The spectrum can be taken by scanning the entire infrared region electronically, without having to change gratings and other optical equipment. EELS is also more surface sensitive than any optical technique, due to the short mean-free-path of low energy electrons. EELS is capable of detecting less than .001 monolayer of carbon monoxide on a surface.

A major disadvantage of EELS is that the best resolution obtained to date (28 cm^{-1}) is roughly a factor of 10 worse than the typical theoretical resolution in IRS. This complicates the process of re-

solving closely spaced vibrational modes. In many cases, however, spectral linewidths are considerably wider ($10\text{-}20\text{ cm}^{-1}$) than the instrumental resolution in infrared spectroscopy. This is usually attributed to the finite lifetime of the excited vibrational state or to inhomogeneous broadening due to residual disorder in the surface. The presence of the huge elastically scattered peak in EELS can obscure very low frequency loss modes, especially if the spectrometer has a large scattered background of electrons due to either poor design or lack of tuning. Another possible disadvantage could arise if the electron beam current were high enough to damage the adsorbed layer. Fortunately, typical electron beam currents are on the order of 10^{-10} A so that EELS is considered to be a non-destructive technique.

The main objectives in the design of our EELS spectrometer were high resolution, high sensitivity, and flexibility in the experimental geometry. The spectrometer allows the scattering angle to be changed quite readily, facilitating experiments probing the angular dependence of EELS. Since most published EELS work has dealt only with specular scattering, a major goal of this project is to study off-specular scattering. The motivation behind these off-specular studies is to explore the potential of EELS as a structural tool, and to add to the understanding of the angular dependence of dipole- and impact-active scattering.

B. PHOTOELECTRON DIFFRACTION

Photoelectron diffraction is a recently developed technique which has been used to make accurate structural determinations of adsorbate

covered metal surfaces. Energy dependent photoelectron diffraction (EDPD) has been pioneered in our research group, with the first experiments described in the doctoral thesis by S. D. Kevan.³ In a EDPD experiment, the probe is energy-tunable synchrotron radiation, which we obtain at the Stanford Synchrotron Radiation Laboratory (SSRL).¹⁷ X-ray photons are emitted by electrons stored in the Stanford Positron Electron Accelerating Ring (SPEAR). All PD experiments described in this thesis were carried out on Beam Line I-1, which delivers monochromatized photons in the energy range 64-1000 eV to our experimental vacuum chamber, where they impinge upon the single crystal sample.

The PD process can be broken down into two steps. The first step occurs when a photon strikes the surface. The photon, carrying a quantum of energy $h\nu$, can excite an electron in a localized bound state of an adsorbate atom on the surface. This bound state, or core level, is characterized by a binding energy BE, and if $h\nu$ is greater than BE, the electron will be excited into an unbound state and can leave the crystal. The kinetic energy KE imparted to the newly created photoelectron is determined by the Einstein equation $KE = h\nu - BE$. This step is referred to as the atomic photoemission step because of its close relationship to photoemission from a gas phase atom.

The second step in PD is the key to its structural sensitivity. The photoelectron can propagate to the angle-resolved electron detector, which has a small solid angle of acceptance and is located above the surface. The photoelectron wave can travel to the detector directly or first undergo one or more scatterings off neighboring atoms. These two components of the final-state photoelectron are referred to

as the direct and the scattered waves, respectively. Direct and scattered waves are emitted coherently, so that their phase relationship at the detector will contain information about the location of the emitting atom with respect to nearby scatterers. At a given kinetic energy, the components of the electron wave emitted from a core level localized on an adsorbate atom may interfere constructively or destructively, depending on the scattering pathlength, the electron wavelength, and the scattering potential. As a result of this interference, the intensity of photoemission will either be enhanced or reduced.

In order to obtain structural information about the location of the adsorbate on the surface, a constant-initial-state (CIS) experiment must be carried out. From the Einstein relation, it is clear that elastic photoemission from a core level initial state with binding energy BE can be observed if the photon energy and detected kinetic energy obey the condition that $BE = h\nu - KE$. Thus, we can observe emission from a constant initial state at a series of kinetic energies if and only if we use a tunable photon source like synchrotron radiation in conjunction with an electron energy analyzer. By stepping the photon energy and kinetic energy by equal amounts, the angle-resolved intensity of the core level can be mapped out. In 1978, Kevan et al., carried out a CIS measurement on the Se(3d) level of the $c(2 \times 2)\text{Se-Ni}(001)$ system.¹⁸ The resulting relative photoemission intensity versus energy (IE) curve showed large modulations superimposed on a smooth atomic-like background. These modulations were the result of the final-state interference, or diffraction, effect described

above. This was the first observation of PD from a core level. Many examples of IE curves can be found in Chapters IV through VII of this thesis.

A special case of EDPD is normal emission photoelectron diffraction, or NPD. Here, the angle-resolved detector is set to accept photoelectrons normal to the surface. This experimental geometry was found to yield very large PD oscillations (up to ≈ 50 percent) so most EDPD structural determinations have been made using only NPD data. Two exceptions are the off-normal study of $c(2 \times 2)\text{Se-Ni}(001)$ (Chapter VI) and the recent work carried out by J. J. Barton, C. C. Bahr, and other members of the Shirley research group.¹⁹

PD can also be observed by varying final-state parameters other than the kinetic energy. C. S. Fadley and co-workers have developed the technique of azimuthal photoelectron diffraction (APD),²⁰ in which the azimuthal angle of photoelectron detection is varied while the photon energy, kinetic energy, and polar angle of detection are held constant. Using the APD technique, they have observed diffraction modulations in the photoelectron intensity of core levels as a function of azimuthal angle, and used them to make structure determinations.

The possibility that PD might be observed and be used to determine surface structure in a manner similar to LEED was first suggested by Liebsch.²¹ The first experimental PD data to yield a structure (measured by Kevan et al¹⁸) were taken after preliminary calculations by Li and Tong.²² They calculated NPD curves for Se(3d) emission from the $p(2 \times 2)$ and $c(2 \times 2)$ selenium overlayers on Ni(001) at

many different values of d_{\perp} , the perpendicular spacing between the adsorbate layer and the top substrate layer, for each possible high-symmetry adsorption site. Their theory of PD was based upon existing LEED multiple scattering theories.²³ The value of d_{\perp} was determined by comparing the experimental NPD curve to all theoretical curves and choosing the best fit based on visual judgment. This method has proven to be successful and has led to a fruitful collaboration between Tong's group and ours.

A shortcoming of the visual judgment method of establishing the best theory-to-experiment fit arises from the fact that this method is subjective and thereby not as quantitative as one would like. As a result, R-factor analysis,²⁴ which is a quantitative method, has been applied in some of the structural determinations discussed below. In an R-factor analysis, the quality of the fit is mathematically evaluated, yielding a reliability factor or R factor for each trial geometry. The R-factor analysis is superior to visual analysis because it is both objective and quantitative.

At this point, I turn to the relationship between PD and other techniques. The most widely applied technique for accurate surface structure determination to date has been LEED. In a LEED experiment,¹ a beam of electrons impinges on an adsorbate/surface complex and is diffracted by two-dimensionally ordered layers into beams leaving the surface at various angles. These angles can be predicted using the conservation of momentum and energy conditions. The intensity of each LEED beam leaving the surface is dependent on the interference between the backscattered waves from the individual layers. This interference

leads to modulations in the intensity versus voltage (IV) curves which can be obtained by changing the incident kinetic energy and measuring the intensity of a particular diffracted beam. The IV curve can be fitted to calculated curves for various trial geometries to make the structure determination. LEED has provided a wealth of information about surface structure and had become well established by 1978, when the first PD and SEXAFS studies were carried out. Perhaps the greatest advantage of LEED is the ease with which an experiment can be carried out relative to the other structural techniques. This is because LEED may be done in any laboratory while EDPD and SEXAFS presently require synchrotron radiation, which is available only at a very small number of facilities in the United States and several other nations.

Despite the experimental disadvantages of EDPD relative to LEED, there are a number of reasons why EDPD experiments are extremely worthwhile. An examination of published LEED and EDPD data on low atomic number (weak scattering) adsorbates indicates that adsorbate-induced modulations remain strong over a wide energy range (at least 200 eV) in EDPD IE curves but not in LEED IV curves. The following explanation of this observation has been proposed by Tong.²⁵ In a LEED IV curve for the (00) beam, which is the specularly reflected component of the incident beam, the diffraction interference between adsorbate and substrate is obscured by intensity modulations which are derived totally from the substrate layers. The (00) beam intensity can be written

$$I_{(00)} \cong R_s^2 + 2f_0 R_s \cos(2ikd_1 + \psi_s - \phi_0) + f_0^2 + \dots \quad (1)$$

where f_0 and R_S are the backscattering amplitudes from the adsorbate layer and the substrate layer, respectively, ϕ_0 and ψ_S are their respective phases, k is the electron wave-vector, and d_\perp is the perpendicular distance defined above. The leading term in Eq. (1), (R_S^2) , is the (00) beam IV curve for the clean substrate. It is strongly oscillatory, but contains no dependence on d_\perp . For a weak scatterer such as carbon, nitrogen, or oxygen, we have $f_0 \ll R_S$. The second term contains d_\perp but is a factor of $2f_0/R_S$ smaller than the first term. Thus, for the LEED (00) beam, a small sinusoidal term which depends on d_\perp is superimposed on the clean substrate (00) beam intensity. At low energies, the second term is still large enough to produce extra features on top of the clean (00) beam IV curve. At higher energies, the backscattering from the adsorbate (f_0) decreases more rapidly than R_S , so the clean substrate IV curve is measured. If, on the other hand, an adsorbate-induced spot such as the $(\frac{1}{2}\frac{1}{2})$ beam is studied, its intensity is given by:

$$I_{(\frac{1}{2}\frac{1}{2})} \cong 2R_S f_\theta^0 f_{\pi-\theta}^0 \cos(2ikd_\perp + \psi_S + \psi_\theta - \psi_{\pi-\theta}) + (R_S f_\theta^0)^2 + \dots \quad (2)$$

where θ is the angle between the surface normal and the $(\frac{1}{2}\frac{1}{2})$ beam. The first term of $I_{(\frac{1}{2}\frac{1}{2})}$ does depend on d_\perp , so its IV curve will be quite sensitive to the adsorbate position. However, this term includes two scattering amplitude terms: f_θ^0 (backscattering) and $f_{\pi-\theta}^0$ (large-angle forward scattering). Both of these terms die off quickly with increasing energy, so that the half-order LEED beams have strong intensities only at low energies. Thus, it is often difficult to compare these curves to theory over a wide energy range, which complicates the structure determination.

Unlike LEED, there are no diffraction beams in PD. In a PD measurement, the detector is placed at a fixed angle with respect to the sample and left at that angle while the IE curve is generated. A great advantage of PD is that the leading modulation term is sensitive to d_{\perp} and produces large oscillations superimposed on a smooth atomic background over a wide energy range. For example, for emission normal to the surface (NPD), Tong has derived the angle-resolved photoelectron intensity:²⁵

$$I_{\text{NPD}} \cong A_0^2 + 2A_0^2 \sum_{\alpha=1}^N R_{\alpha} \cos \{ 2k[d_{\perp} + (\alpha-1)b] + \phi_{\alpha} + \phi^{+} - \phi^{-} \} \quad (3)$$

where A_0 is the atomic emission amplitude, b the substrate interplanar spacing, R_{α} and ϕ_{α} the backscattering amplitude and phase of the α th substrate layer, and ϕ^{+} and ϕ^{-} the phases of emission in and out of the solid. Since the $I_0 = A_0^2$ atomic intensity term in Eq. (3) is a smooth function, it can be subtracted from I_{NPD} to yield the cosine modulations, whose frequency depends on d_{\perp} . The normalized modulation term is

$$\chi(k) = \frac{I_{\text{NPD}} - I_0}{I_0} \cong 2 \sum_{\alpha=1}^N R_{\alpha} \cos \{ 2k[d_{\perp} + (\alpha-1)b] + \phi_{\alpha} + \phi^{+} - \phi^{-} \}. \quad (4)$$

It is clear that the modulations in NPD IE curves depend mainly on backscattering off the substrate, due to the absence of the adsorbate backscattering factor f_0 . This equation predicts substantial oscillations in NPD curves of overlayer systems over a wide range (at least 500 eV). Such oscillations have been observed and then used to make

accurate structure determinations. According to Tong's theory, a Fourier transform (FT) of the function $\chi(k)$ in Eq. (4) will give peaks related to the perpendicular distances $d_{\perp} + (\alpha-1)b$, $\alpha = 1, 2, 3, \dots$. This allows an explicit structure determination. A single scattering approach to PD has been developed by Barton, et al.¹⁹ which leads to a different interpretation of the FT results. This approach is compared to Tong's in Chapter IV.

Another difference between LEED and PD is that in LEED, the sample must have good long-range surface order to observe LEED spots and measure IV curves. This is not a requirement in PD, where the phase of the emitted photoelectron wave (the PD analog of the incident LEED beam) is fixed so that the direct and scattered waves from a single adsorbate atom add coherently and produce diffraction. Therefore disordered overlayer systems may be studied with PD. The only surface order requirement in PD is that the substrate must be ordered in the immediate region (the photoelectron's mean-free-path) surrounding each adsorbate atom. The coherent nature of PD also makes it a good candidate for studying multiple-adsorption-site overlayers (Chapter V).

A consequence of the phase coherence of PD is its atom specificity. The existence of a different set of core levels for each element enables the generation of a separate IE curve for each atomic species of a molecular adsorbate. For example, in a PD study of CO bonded to a metal surface, IE curves can be generated for both the C(1s) and O(1s) levels (Chapter VII). Since the core level is localized on one atomic species, a structural determination can be carried out on that species alone. This is not true in LEED, where the IV curve for each beam

contains scattering events originating from all atomic species in the adsorbate.

A final shortcoming of electron bombardment techniques such as LEED is the potential for electron beam damage of the adsorbate layer. This problem has been largely overcome in a recent experiment in which LEED data are collected in a pulse-counting mode.²⁶ In any case, PD has the advantage of being a non-destructive technique.

It is also useful to compare EDPD with SEXAFS. In most SEXAFS experiments, the intensity of Auger electrons originating from a core level on an adsorbate is monitored as a function of incident photon energy. The principle of the Auger-SEXAFS method² is the same as that in transmission-EXAFS, i.e., the photoabsorption cross-section of the excited atom is modulated by interference between outgoing and backscattering photoelectron waves. Because the photoabsorption process eventually results in emission of secondary decay products such as Auger electrons and x-rays, the intensity of these products is proportional to the absorption cross-section. Due to several experimental considerations, it is most convenient to measure SEXAFS by the Auger technique. A SEXAFS spectrum consists of small oscillations ($\pm 5\%$) superimposed on the atomic photoabsorption cross-section. Fourier-transform analysis is then used to derive structural information from the data.

There are several similarities between EDPD and SEXAFS. With the recent advent of Fourier-transform PD, both methods are direct structural techniques. Both require synchrotron radiation and involve the measurement of a photoelectron interference effect as a function of

photon energy. For Fourier-transform analysis to succeed, data must be obtained over a wide energy range. The two techniques share the advantage of being atom specific.

The most important difference between the two techniques is in the mode of final state detection: PD is an angle-resolved method while SEXAFS is angle-integrated. As a consequence, PD is most sensitive to distances from the adsorbate to individual substrate atoms located near the line determined by the angle-resolved detector and the adsorbate atom on the surface. SEXAFS, on the other hand, is sensitive to radial distances from the adsorbate to neighboring coordination spheres of atoms. In both cases phase shifts limit the accuracy of the determined structure. While both PD and SEXAFS phase shifts include a contribution due to backscattering by a substrate atom, only the SEXAFS phase shift includes an emitter or central atom contribution as well. A disadvantage of SEXAFS is that its modulation term decreases rapidly (it goes as R^{-2}) with the distance R from adsorbate to neighboring substrate atoms. As a result, SEXAFS data generally yield the first nearest neighbor and occasionally the second while in PD, up to four inequivalent neighbor distances can be obtained.¹⁹ In addition, the size of the modulations in PD (≈ 50 percent) are usually about a factor of 10 larger than those in SEXAFS (≈ 5 percent), making the reduction of PD data considerably easier.

Both techniques can yield even more information if one takes the measure of varying the experimental geometry. In PD, much more structural information can be obtained by taking IE curves at several well-chosen photoemission angles at which the adsorbate atom, a nearby sub-

strate atom, and the detector are lined up. Using the FTPD method, Barton et al.¹⁹ have shown that this strategy can produce distances from the adsorbate to individual neighbor atoms, leading to an unambiguous and extremely accurate structure. Their theoretical approach to the PD process is different than Tong's, and will be discussed in Chapter IV. In SEXAFS, one can take advantage of the polarization dependence of the SEXAFS amplitude function. By measuring the SEXAFS at different photon polarization directions with respect to the surface, Citrin et al.²⁷ have shown that the coordination number of the nearest neighbor, and therefore the adsorption site, can be obtained. The polarization-dependence of SEXAFS is particularly useful when it is not possible to obtain the second-nearest neighbor distance directly.

On the basis of this comparison of PD to LEED and SEXAFS, it is clear that PD is particularly useful in the study of disordered overlayers, molecular overlayers, multiple site systems, and adsorbates which are weak electron scatterers. It is a very large effect, facilitating the use of Fourier-transform analysis. The angle-resolved nature of PD makes it possible to collect data at many different emission angles. Consequently, off-normal EDPD data may be used to complement NPD data when making a structure determination. Every one of the experiments described in Chapters IV through VII has exploited at least one of these advantages.

REFERENCES

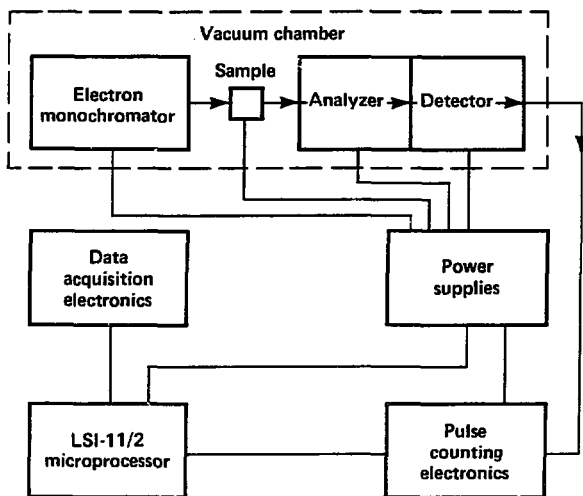
1. F. Jona, J. Phys. C 11, 4271 (1978).
2. P. A. Lee, P. H. Citrin, P. Eisenberger, and B. M. Kincaid, Rev. Mod. Phys. 53, 769 (1981).
3. S. D. Kevan, Appl. Opt. 19, 3974 (1980); Ph.D. thesis, University of California, Berkeley, 1980, unpublished.
4. H. Ibach and D. L. Mills, Electron Energy Loss Spectroscopy and Surface Vibrations (Academic Press, New York, 1982).
5. T. S. Rahman, J. E. Black, and D. L. Mills, Phys. Rev. Lett. 46, 1469 (1981); Phys. Rev. B 25, 883 (1982).
6. S. Lehwald, H. Ibach, and H. Steininger, Surf. Sci. 117, 342 (1982).
7. E. Evans and D. L. Mills, Phys. Rev. B 5, 4126 (1972); Surf. Sci. 48, 59 (1975).
8. W. Ho, R. F. Willis, and E. W. Plummer, Phys. Rev. Lett. 40, 1463 (1978).
9. S. Y. Tong, C. H. Li, and D. L. Mills, Phys. Rev. Lett. 44, 407 (1980); Phys. Rev. B 21, 3057 (1980); Phys. Rev. B 24, 806 (1981).
10. R. P. Eischens, S. A. Francis, and W. A. Plisken, J. Phys. Chem. 60, 194 (1956).
11. J. C. Campuzano and R. G. Greenler, Surf. Sci. 83, 301 (1979).
12. W. G. Golden, D. S. Dunn, and J. Overend, J. Catal. 71, 395 (1981); R. Ryberg, Chem. Phys. Lett. 83, 423 (1982).
13. R. B. Bailey, T. Iri, and P. L. Richards, Surf. Sci. 100, 626 (1980).
14. S. Chiang, R. G. Tobin, and P. L. Richards, unpublished.

15. P. N. Sanda, J. M. Warlaumont, J. E. Demuth, J. C. Tsang, K. Christmann, and J. A. Bradley, *Phys. Rev. Lett.* 45, 1519 (1980).
16. A. Campion, J. Keenan Brown, V. M. Grizzle, *Surf. Sci.* 115, L153 (1982).
17. H. Winick and S. Doniach, editors, Synchrotron Radiation Research (Plenum, New York, 1980).
18. S. D. Kevan, D. H. Rosenblatt, D. Denley, B.-C. Lu, and D. A. Shirley, *Phys. Rev. Lett.* 41, 1565 (1978).
19. J. J. Barton, C. C. Bahr, Z. Hussain, S. W. Robey, J. G. Tobin, L. E. Klebanoff, and D. A. Shirley, unpublished.
20. P. J. Orders, R. E. Connelly, N. F. T. Hall, and C. S. Fadley, *Phys. Rev. B* 24, 6163 (1981); and references therein.
21. A. Liebsch, *Phys. Rev. Lett.* 32, 1203 (1974).
22. C. H. Li and S. Y. Tong, *Phys. Rev. Lett.* 42, 901 (1979).
23. M. A. Van Hove and S. Y. Tong, Surface Crystallography by LEED (Springer-Verlag, Berlin, 1979).
24. E. Zanazzi and F. Jona, *Surf. Sci.* 62, 61 (1977).
25. S. Y. Tong, W. M. Kang, D. H. Rosenblatt, J. G. Tobin, and D. A. Shirley, unpublished.
26. P. C. Stair, *Rev. Sci. Instrum.* 51, 132 (1980).
27. P. H. Citrin, P. Eisenberger, and R. C. Hewitt, *Phys. Rev. Lett.* 41, 309 (1978).

FIGURE CAPTION

Figure 1. Schematic of the EELS experimental setup described in this thesis.

EELS EXPERIMENTAL OVERVIEW



XBL 827-7122

Fig. 1

PART I.

ELECTRON ENERGY LOSS SPECTROSCOPY

II. DESIGN AND PERFORMANCE OF A HIGH RESOLUTION ELECTRON ENERGY LOSS SPECTROMETER

In this chapter, the design and performance of a high resolution EELS spectrometer will be described. The general criteria used in designing the spectrometer are discussed in Section A. In Section B the machine is discussed in detail, with subsections devoted to the vacuum chamber and shielding, the electron monochromator, the electron energy analyzer, the power supplies, the pulse counting and data acquisition electronics, the tuning procedure, and the software used for spectrum generation. In Section C the performance of the spectrometer is evaluated.

A. DESIGN CRITERIA

The two most important factors in the design of an EELS spectrometer are resolution and sensitivity. Unfortunately, it is difficult to improve the resolution without losing sensitivity, or vice versa, by changing a single design parameter. Therefore, one must make trade-offs between resolution and sensitivity in order to obtain a high-resolution spectrum in a reasonable amount of time. A third criterion is the capability for angular motion of the electron monochromator, crystal, and electron analyzer. Two of these three components of the spectrometer must be movable to enable many types of experiments to be carried out, as well as to facilitate the difficult tuning up process.

The major contributions to the full-width at half maximum (FWHM) resolution of the elastic beam in EELS are included in the expression

$$\Delta E_{\text{total}} = [(\Delta E_{\text{mono}})^2 + (\Delta E_{\text{anal}})^2 + (\Delta E_{\text{non-ideal}})^2]^{1/2} \quad (1)$$

where ΔE_{mono} and ΔE_{anal} refer to the theoretical FWHM resolution of the monochromator and analyzer, respectively, and $\Delta E_{\text{non-ideal}}$ represents the contribution of non-ideal effects. Included in $\Delta E_{\text{non-ideal}}$ are factors such as stray magnetic and electric fields, power supply noise, lack of tuning or non-ideal behavior in the electron optics, lack of sample cleanliness and order, contact potential differences due to presence of different materials along the electron path, and fields created by charging of insulators. If careful attention is not paid to each of these non-ideal effects, the contribution of $\Delta E_{\text{non-ideal}}$ may dominate ΔE_{total} and degrade the spectrometer resolution considerably.

EELS spectrometers are invariably judged by their FWHM resolution. A more important property is the base resolution, or more specifically, the width of the inelastic tail on the low kinetic energy side of the elastic peak. This tail must fall off quite rapidly if the weakest loss features are to be observed. Therefore, it is important to design the monochromator and analyzer to have as little tailing as possible in their transmission functions, and a low background of scattered electrons.

The best published FWHM resolution to date¹ is about 28 cm^{-1} (3.5 meV). It is more difficult to quote the base width resolution or background of EELS spectrometers, since there is no generally accepted way of expressing these quantities, and it is very difficult to obtain

information about them from published spectra. Comparisons between EELS spectrometers are, as yet, partially non-quantitative in nature.

B. DESCRIPTION OF THE EELS SPECTROMETER

1. Vacuum Chamber and Shielding.

The EELS vacuum chamber is an ultra-high vacuum compatible, stainless steel cylinder which is 45.72 cm in diameter and 55.88 cm long. A diagram of the chamber is shown in Fig. 1. There are three horizontal planes: the sample preparation plane, the EELS plane, and the utility plane.

The sample is mounted on a high precision manipulator (Vacuum Generators HPT2-RD2S/SM2 EXTZ-CLN2-EBH) with extended travel capability (150 mm) which allows the sample to be moved between the sample preparation and the EELS planes. The manipulator has a sample plate which has space for at least three single crystal samples, which are typically 1 cm by 1 cm in size. The sample plate is electrically isolated from the rest of the manipulator to allow the sample to be biased with respect to ground during an EELS experiment. Samples can be resistively heated to about 1000 K, which is sufficient for cleaning copper and nickel single crystals. Sample temperatures are measured with a chromel-alumel thermocouple which is spot welded to the tantalum sample plate. The sample can be rotated about the manipulator shaft axis by 360° (polar angle rotation) and about the sample normal by 180° (azimuthal angle rotation). A liquid nitrogen sample cooling system has been designed and built, but has yet to be installed. This system

was tested on another manipulator and is capable of cooling samples to below 120 K.

The sample preparation plane contains: (1) LEED/Auger optics (Varian 981-0127) and electron gun (Varian 981-2125) for sample characterization with low energy electron diffraction and Auger electron spectroscopy, (2) a viewport for examination of LEED patterns, (3) an argon ion sputtering gun (Physical Electronics 04-161) for sample cleaning, (4) an effusive beam doser, which reduces chamber contamination by a factor of 80 (relative to ambient dosing) when positioned 1 cm away from the sample,² and (5) a viewport which may be used for lining up the sample with either the sputtering gun or the beam doser.

The most important chamber plane is the EELS plane, which contains: (1) the electron monochromator (described in Subsection 2), (2) the electron energy analyzer (described in Subsection 3), which is actually mounted on the bottom flange of the chamber but accepts electrons in the EELS plane, and (3) three viewports for lining up the scattering geometry of the EELS experiment. This plane contains an extra port where an ultraviolet photon source was mounted for earlier photoemission studies.

The lowermost plane is a utility plane which contains: (1) a nude ionization gauge (Varian 971-5008), (2) a residual gas analyzer (Inficon IQ-200 quadrupole mass spectrometer), which is quite useful for adsorbate characterization and leak testing, (3) viewports, (4) a bakeable valve for external pumping, and (5) a large port for the internal pumps, which are a 220 liter/sec ion pump (Varian 912-7014) and a 800 liter/sec water-cooled titanium sublimation pump (Varian 916-0009).

The base pressure of the chamber is about 1.5×10^{-10} torr. This pressure can be obtained by baking the chamber at 475 K for 36 hrs.

The reduction of all magnetic fields and those electric fields external to the electron optics is essential during an EELS experiment.³ This required an extensive system of magnetic and electric shielding. The sources of magnetic field were found to be the earth's field (500 mG), the Bevatron accelerator at LBL (50 mG), and the ion pumps (15 mG). Magnetic fields were measured with a milliammeter (Hewlett-Packard 4288R) or an oerstedmeter (Magnaflex FM-204), and associated probes.

A system of Helmholtz coils, which encircles the vacuum chamber, has been employed to compensate for the magnetic fields of the earth and the Bevatron. A photograph of the spectrometer and Helmholtz coil system is shown in Fig. 2. The earth's field is relatively constant with time and can be compensated for fairly easily. A system of Hall probes is set up to measure the field in three mutually orthogonal directions which correspond to the three axes of the Helmholtz coils. The compensating current in each of the three independent coils is then adjusted until the coils produce a field equal in magnitude and opposite in direction to that of the earth. When the Bevatron is not running, the coils need only occasional adjustment. Unfortunately, the Bevatron is located in close proximity to the EELS spectrometer (~ 200 m), and its field is much more difficult to deal with because it pulses with a very short period, usually 6 sec. This dynamic field necessitates the activation of a dynamic compensation system in the direction perpendicular to the earth's surface, which is by far the

largest component of the Bevatron field. The dynamic compensation is able to continuously react to the changing Bevatron field with a fast time constant (0.1 sec), reducing the magnitude of the dynamic field to less than 1 mG at the Hall probes. Unfortunately, the electron path covers an area which is larger than the field free region created by the coils, resulting in small fields at the extremities of the spectrometer. To alleviate this problem, the vacuum chamber was lined with two layers of .36 mm thick μ metal (separated by about 1 mm). This static μ metal shielding by itself is unable to compensate for the dynamic field produced by the Bevatron, but the combination of Helmholtz coils and μ metal reduces the penetration of external fields inside the chamber to extremely low levels.

The two ion pumps used to evacuate the chamber were positioned sufficiently far from the EELS region that the field they produce in the absence of shielding (15 mG) was reduced to negligible levels after shielding was installed.

Magnetic fields inside the vacuum chamber were minimized by utilizing non-magnetic materials such as copper, molybdenum, and tantalum wherever possible and very low permeability stainless steel (Type 316) elsewhere. All slits and apertures, which come into close proximity with the electron beam, were constructed from molybdenum or tantalum. Finally, the magnetic field due to the filament leads, which carry 2A of DC current, was minimized by twisting the leads into a non-inductive winding.

Electrostatic shielding is considerably easier to accomplish. The principle task is to shield the low energy electron beam from the high voltage detector leads. This was accomplished by mounting pieces of stainless steel sheet between these leads and the interaction (sample) region. The beam was also shielded from all ceramic and other insulator parts as well as possible.

2. Electron Monochromator.

The purpose of the electron monochromator is to fire a well-focused beam of monoenergetic electrons at the sample. Most electron monochromator assemblies consist of an electron source, a focusing and collimating lens, an energy selector, and an output lens which transports the monochromatic beam to the sample. The electron source is typically a tungsten filament. The lenses are usually multielement cylinder or aperture lenses whose focusing properties can be predicted from published calculations. The most common energy selectors are electrostatic deflectors such as the 180° hemispherical sector,^{4,5} the 127° cylindrical sector,^{6,7} and the cylindrical mirror deflector.¹ It is important that the energy spread of the beam be as narrow as possible and that the background of scattered electrons be extremely small. A cross-sectional view of the monochromator assembly is shown in Fig. 3. Components constructed out of metal are cross-hatched while insulators are shaded. Names of all components are indicated, as well as the corresponding power supply voltage labels, which are designated by capital letters in parentheses. A photograph of the monochromator and mounting

flange is shown in Fig. 4, and a close-up view of the monochromator itself is shown in Fig. 5.

The most important part of any electron monochromator assembly is the energy selector. The 180° hemispherical sector was chosen as the energy selector in this spectrometer primarily because of its superior theoretical resolution. In fact, the theoretical FWHM resolution of a 180° hemispherical sector is a factor of two greater than that of a 127° cylindrical sector of the same mean radius.⁸⁻¹⁰ Since magnetic field and spatial considerations in the vacuum chamber always limit the size of an energy selector, it was necessary to use the 180° hemispherical sector to optimize resolution. The energy resolution (FWHM) of a 180° hemispherical sector is (neglecting aberrations)

$$\Delta E_{1/2}/E_0 = w/2R_0 \quad (2)$$

where $\Delta E_{1/2}$ is the FWHM of the triangular transmission function of the sector, w is the width of the entrance and exit slits, R_0 is the mean radius between the inner and outer hemispheres, and E_0 is the pass energy, or the kinetic energy with which electrons will travel through the sector in a path defined by the mean radius.^{9,11} The pass energy is determined by the voltages placed on the hemispheres (see below). It is clear from Eq. (2) that in order to minimize $\Delta E_{1/2}$, one must attempt to maximize R_0 and minimize w and E_0 . As mentioned above, the choice of as large an R_0 as possible is restricted by magnetic field and spatial considerations. As w or E_0 is decreased, the total output current of the monochromator is auto-

matically reduced due to space-charge limitations on the maximum current which can be transported through a small slit at low kinetic energy.¹¹ As E_0 is decreased, the effects of inhomogeneities in the focusing electric field of the sector, contact potential and charging problems, and stray magnetic fields become more problematical. Consequently, one must be cautious in making the choices of R_0 , w , and E_0 when designing a hemispherical sector. It is important to remember that R_0 and w are fixed physical dimensions while E_0 can be varied with the power supply.

EELS places especially strong demands on energy selectors such as the hemispherical sector, because the background of scattered electrons should be less than .01 percent of the maximum intensity in the elastic peak. Therefore, the triangular transmission function of the sector must have as little tailing as possible at its base. The origin of the tailing is the pencil half angle α of acceptance of the sector, which is determined by the input lens. Kuyatt and Simpson^{9,11} chose $\alpha^2 = w/4R_0$ in the design of their lens system, which leads to a theoretical base width of the transmission function of:

$$\Delta E_{\text{base}}/E_0 = (w/R_0) + \alpha^2 = (5w/4R_0) = 2.5 (\Delta E_{1/2}/E_0). \quad (3)$$

With ideal behavior, the transmission function of this sector would go to zero at 2.5 times the FWHM resolution.

Unfortunately, electrons scattered by the surfaces of slits, lens elements, and hemispheres can result in a substantial background signal. Elimination of much of the background can be accomplished by placing a pre-filter, or pre-monochromator, before the monochromator.

We chose an identical hemispherical sector to be the pre-monochromator (see Fig. 3). Passing the electron beam through two hemispherical sectors reduces the scattered background significantly.

Both the pre-monochromator and the monochromator were chosen to have a mean radius (R_0) of 2.54 cm and a gap between inner and outer hemispheres of 0.76 cm. The entrance aperture of the pre-monochromator is 0.78 mm in diameter, and both the entrance and exit slits of the monochromator are 0.15 mm wide by 1.57 mm long. The entrance slit of the monochromator simultaneously serves as the exit slit of the pre-monochromator. Because the aperture diameter of the pre-monochromator is 6 times larger than the slit width of the monochromator, its resolution is worse by the same factor. The theoretical FWHM resolution of the monochromator is .30 percent from Eq. (2) and consequently $\Delta E_{1/2}$ is .0030 times the pass energy. Following Kuyatt and Simpson, the maximum allowable angular acceptance of the monochromator is $\alpha = (w/4R_0)^{1/2} = .035$ or about 2° half angle. This condition is physically enforced by the input lens and the pre-monochromator regardless of pass energy. The pass energy (E_0) of the monochromator can be calculated if the potential difference, ΔV , between inner and outer hemispheres is known:¹¹

$$E_0 = e\Delta V(R_{in}R_{out}/2R_0\Delta R) = 1.629 e\Delta V \quad (4)$$

where e is the charge of the electron, R_{in} (2.16 cm) and R_{out} (2.92 cm) are the radii of the inner and outer hemispheres, respectively, $R_0 = (R_{in} + R_{out})/2$ is the mean radius and $\Delta R = (R_{out} - R_{in})$ is the gap between hemispheres. Since ΔV is usually measured in volts, pass energy is generally expressed in units of electron volts. All four hemispheres

in the complete assembly were constructed from OFHC copper, and were machined to a radial tolerance of $\pm 10 \mu\text{m}$ on a numerical control lathe (Lawrence Livermore National Laboratory). All hemispherical surfaces were coated with a thin layer of graphite (Acheson Aquadag) to reduce the background of scattered electrons. In fact, all electron optical surfaces in the lenses and hemispherical sectors were coated with graphite to provide a constant contact potential for the electron beam during its entire trajectory.

Now that we have discussed the choice of the hemispherical sectors, let us turn to the other components of the electron monochromator assembly. This discussion will begin with the electron source and continue with the other parts of the monochromator assembly in the order in which the electron beam passes through them.

The electron source is a hot (2800K) tungsten (W) hairpin filament (Japan Electron Optics Limited 417003) which is normally used in electron microscopes. A high-brightness lanthanum hexaboride (LaB_6) cathode (Kimball Physics ES-423) cathode was also tried, but did not appreciably increase the output current from the monochromator. This observation indicates that the output current is space-charge limited by the monochromator entrance slit.¹¹ In addition, the LaB_6 cathode provided a very unstable emission current, and is much more fragile than a W filament due to the necessarily tenuous mounting of the LaB_6 single crystal on its graphite holder. Consequently, after some initial experimentation with the LaB_6 cathode, a decision was made to use a W filament. The filament produces electrons with a thermal spread of energies (about 0.6 eV FWHM).^{11,12}

Electrons emitted by the filament are focused onto the entrance aperture of the pre-monochromator by lens A, a three element asymmetric lens. The center of the filament (the object) is located close to the focus of a spherical repeller, resulting in a well-collimated beam. The repeller (power supply voltage REPELLER) is usually biased negatively with respect to the filament center potential. The beam is then accelerated, deflected and focused by the three split aperture lens elements of the A lens. The lens elements are 4.37 cm outer diameter by 0.25 mm thick tantalum disks. They had 3.18 mm diameter holes drilled through them before they were split in half. They are spaced 0.76 mm apart and held in place by ceramic insulators. The first (voltages $\Delta A1$ LEFT and $\Delta A1$ RIGHT) and third ($\Delta A3$ LEFT and $\Delta A3$ RIGHT) pairs of lens elements are horizontal deflectors while the middle pair is a vertical deflector ($\Delta A2$ UPPER and $\Delta A2$ LOWER). Generally, voltages on the A1 and A3 lens elements are quite low (within a few volts of the monochromator reference (MONO. REFERENCE), which is the potential at which electrons emitted by the filament have zero kinetic energy). Most of the acceleration of the electrons coming off the filament is accomplished by the A2 elements. The potential difference between each pair of split deflectors is usually less than 2 volts, but its application can result in orders of magnitude higher monochromator output current than could be obtained without deflectors. Therefore, deflectors must be included in the A lens to properly focus the beam onto the entrance aperture of the pre-monochromator. The total distance between filament center and entrance aperture is 6.2 mm. Due to the close proximity of the A lens elements, their voltages are

carried by tantalum wires which are spot welded to the elements. All other monochromator voltages are carried by copper wires which are held in contact with lens elements by small screws.

Electrons which successfully traverse the entrance aperture of pre-monochromator are well-collimated unless they have scattered off a lens element or hemisphere. Their kinetic energy has been retarded to approximately the pass energy by the entrance aperture potential (MONO. SLIT). Once inside the pre-monochromator sector, electrons are deflected by the R^{-1} potential between hemispheres, which is established by placing the voltages PREMONO. INNER and PREMONO. OUTER on the inner and outer hemispheres, respectively. Those electrons selected by the pre-monochromator travel through the monochromator entrance slit (voltage MONO. SLIT) into the monochromator and are deflected by its electric field, created by the voltages MONO. INNER and MONO. OUTER. They are then subjected to the more stringent monochromatization of this second energy selector when they reach the monochromator exit slit, which is at the voltage MONO. SLIT.

After exiting the monochromator, the remaining electrons must be accelerated to the sample. This is accomplished by the B lens, another three element asymmetric lens. The B lens was designed using theoretical focal length data for three element aperture lenses compiled by Harting and Read.¹³ Both this lens and the C lens have close to unit magnification and constant transmission during normal operation. The first two elements of the B lens are split deflectors, while the third element is simply an aperture at ground (it receives a high quality ground voltage from the power supply). The first element is a vertical

deflector (voltages $\Delta B1$ UPPER and $\Delta B1$ LOWER). The middle element of the lens is a horizontal deflector (voltages $\Delta B2$ LEFT and $\Delta B2$ RIGHT). The B1 and B2 deflectors allow the beam to be moved in any direction with respect to the sample. The third element (GROUND) provides a field-free region between the B lens and the sample, which is usually at ground. However, the sample can be biased above or below ground using the CRYSTAL BIAS voltage produced by the power supply. The B lens elements are constructed from 0.25 mm thick molybdenum sheet, have 7.87 mm diameter apertures, and are spaced 7.92 mm apart.

The pre-monochromator and monochromator hemispheres and the A and B lenses are all held in place by the hemisphere mounting plate. The mounting plate is connected, by a series of stainless steel supports, to a 203 mm O.D. Conflat flange (visible in Fig. 4). Monochromator voltages are fed into the chamber by two 10-pin feedthroughs (Varian 954-5033) and then carried to the lens elements with copper or tantalum wires insulated with ceramic beads.

The electron beam is then scattered off the sample into the analyzer, which is described next.

3. Electron Energy Analyzer.

The electron energy analyzer is used to measure the number of electrons reflected from the sample per unit time into a small solid angle at a kinetic energy which has been chosen by the experimenter. A spectrum can then be taken by measuring the count rate at a series of kinetic energies over a wide energy range. A typical analyzer consists of an input lens, an energy selector, and a detector. The input

lens and energy selector are often quite similar to those used in electron monochromators. The detector is an electron multiplier. A cross-sectional view of our analyzer is shown in Fig. 6, with metal components cross-hatched and insulators shaded. Component names and their corresponding power supply voltage labels are indicated.

As in the case of the electron monochromator, the most critical choice in electron analyzer design is that of the energy selector. In EELS, the electron analyzer must be designed with the same goals as the electron monochromator: high resolution, low scattered background, and high sensitivity. Our analyzer also has the additional requirement of extensive motion about the sample. The need for high resolution again resulted in the selection of the 180° hemispherical sector as the energy selector. Unfortunately, the need for analyzer mobility prevented the use of a pre-analyzer. Instead, the number of scattered electrons was reduced by placing a double exit slit on the analyzer.

The optimization of the physical and operating parameters for the hemispherical sector (slit width, mean radius, angular acceptance, and pass energy) has been discussed in the previous subsection with reference to the electron monochromator, and will not be discussed here. The analyzer was chosen to have a mean radius of 5.40 cm and a gap between hemispheres of 1.27 cm. The entrance and exit slits are 0.25 mm wide by 3.18 mm long. The resolution can then be calculated to be $\Delta E_{1/2}/E_0 = .0023$ using Eq. (2). The maximum angular acceptance, determined by the input lens, was $\alpha = 5^\circ$ half angle during the time that the data in this thesis were measured. In the near future, α will be reduced to 2° to conform to the criteria of Kuyatt and Simpson, which

were discussed earlier. The pass energy is given by

$$E_0 = e\Delta V(R_{in}R_{out}/2R_0\Delta R) = 2.096 e\Delta V \quad (5)$$

where e is the charge of the electron, ΔV is the potential difference between inner and outer hemispheres, and the other quantities were defined after Eq. (4). The two hemispheres were constructed from OFHC copper and coated with graphite.

Note that the resolution of the analyzer is roughly equal to that of the monochromator. If both are operated at about the same pass energy (E_0) they will then contribute about equally to the combined theoretical spectrometer-induced linewidth. In the absence of non-ideal behavior,

$$\Delta E_{1/2}^{\text{spect}} = [(\Delta E_{1/2}^{\text{mono}})^2 + (\Delta E_{1/2}^{\text{anal}})^2]^{1/2}, \quad (6)$$

so that if $\Delta E_{1/2}^{\text{mono}} = \Delta E_{1/2}^{\text{anal}}$, then $\Delta E_{1/2}^{\text{spect}}$ will be a factor of $\sqrt{2}$ greater than that of its two contributing parts. Under these conditions, both monochromator and analyzer can be expected to approach theoretical behavior to the same extent.

Now, the other components of the analyzer assembly will be described. After scattering off the sample, electrons are collected by lens C, which is a three element asymmetric lens with known properties.¹³ The electron beam is retarded by this lens and focused onto the entrance slit of the analyzer. The design of the C lens is quite similar to that of the B lens at the exit of the electron monochromator. The first aperture is not split in half and is at ground potential, so that electrons will not experience any electric field in

travelling from the sample to the analyzer. The middle aperture is a split horizontal deflector (voltages $\Delta C1$ RIGHT and $\Delta C1$ LEFT), and the third aperture is a split vertical deflector ($\Delta C2$ UPPER and $\Delta C2$ LOWER). The C lens elements are made from 0.25 mm thick molybdenum sheet, have 6.35 mm diameter apertures, and are spaced 3.05 mm apart.

All electrons which pass through the entrance slit of the analyzer have been retarded by the entrance slit potential (ANAL. SLIT). Those electrons at the desired kinetic energy (chosen by the experimentalist) will be deflected along the mean radius of the analyzer (travelling at the pass energy) and pass through the exit slit. The R^{-1} potential required for this deflection is set up by the voltages ANAL. INNER and ANAL. OUTER on the inner and outer hemispheres, respectively. After passing through the exit slit (voltage ANAL. SLIT), electrons must pass through a second, identical slit located 1.0 mm behind the first slit. This slit, which is at the same potential as the first slit, only accepts electrons which entered the first slit with a pencil half angle of less than 14° . The double exit slit eliminates many electrons scattered by the lens and analyzer surfaces. Most significantly, it eliminates the acceptance of electrons which have taken one bounce off the outer hemisphere and then passed through the first slit. Electrons taking this path have been shown to be a source of spurious peaks in other EELS spectrometers.⁶

One problem encountered with any deflection-type energy selector is that of field termination at the entrance and exit of the deflector. In a hemispherical sector, the R^{-1} field which exists in the interior portion of the sector becomes distorted at its extremities. To help

preserve the field at the analyzer exit, a series of field termination wires was installed. Originally, five wires, equally spaced between the inner and outer hemispheres, were used, with each wire set at a voltage corresponding to the R^{-1} potential function at that particular radius. Later, the middle wire was removed, as field termination was found to be least necessary at the middle of the gap. This left the configuration shown in Fig. 6, with four wires being placed across the analyzer exit. The power supply voltages on these wires are VS1, VS2, VS4, and VS5.

After energy analysis, electrons are detected by a Spiraltron electron multiplier (Galileo SEM 4219) which is positioned about 1.5 mm behind the double exit slit. Post-acceleration of the electrons into the multiplier cone was found to degrade the analyzer resolution by as much as 20 percent, so the cone section (power supply voltage INPUT) was kept at the slit potential. This resulted in a decrease in count rate of less than a factor of 2. The multiplier high voltage produces a gain of 10^6 - 10^7 , and the resulting pulses at the exit end of the multiplier (power supply voltage OUTPUT) are swept to a metal collector (BIAS) by an additional accelerating potential of 200 volts. The pulses are then individually counted by the pulse counting electronics, which will be described in Subsection 5.

In order to attain large flexibility in the electron detection angle with respect to the sample, it was necessary to mount the entire analyzer assembly on a two circle goniometer. This goniometer has been described elsewhere,⁴ and will not be discussed in detail here. Briefly, the analyzer is mounted so that it can be rotated on a verti-

cal circle by 90° and on a horizontal circle by 180° , with the center of both circles being the center of the vacuum chamber, where the sample is positioned for EELS work. Both motions are driven by rotary motion feedthroughs at the base of the analyzer mounting flange, which is the 419 mm diameter flange at the bottom of the chamber. This allows for positioning of the analyzer at any location in the entire 2π steradians of solid angle below the EELS plane. This flexibility, combined with the capability to translate, rotate, and tilt the sample provided by the high precision manipulator, allows the experimenter to work with virtually any experimental geometry he wishes.

4. Power Supplies.

An EELS experiment cannot be carried out without a number of interconnected power supplies. A schematic of our power supply system is shown in Fig. 7. The heart of this system is the hemispherical EELS supply, which provides all of the lens voltages.

The main requirements for a power supply for use in high-resolution EELS are high stability and low noise. If the theoretical energy resolution of the spectrometer is 5 meV and one desires to have 10 energy channels in each peak, the energy width per channel will be 0.5 meV. In order to resolve individual channels, all spectrometer voltages must have less than 0.5 mV of ripple and noise. If one desires an extremely accurate kinetic energy scale during any given scan, and reproducibility in kinetic energies over many scans, the drift in any voltage must be less than 0.1 mV over the course of a multiple scan spectrum. The time constant for settling of the energy sweep supplies must be much

faster than the time spent taking data at each channel, to avoid a large percentage of "dead time" needed for power supply settling during data acquisition periods. Finally, the supply must be set up in a manner which facilitates the tuning up process.

The hemispherical EELS supply now being used, which was designed and fabricated at LBL,¹⁴ meets all of the above criteria. The important characteristics of the supply's performance are: (1) less than 0.5 mV peak-to-peak high-frequency noise, (2) less than 0.5 mV peak-to-peak 60 Hz ripple, (3) a time constant of 0.003 seconds, (4) a maximum of 0.003 mV drift per 1 hour period, and (5) 100 second stabilization time after start-up. Technical details of the supply's construction (voltage references, operational amplifiers, etc.) can be found elsewhere.¹⁴

The supply has two reference voltages: a monochromator reference (MONO. REFERENCE), upon which all monochromator voltages float, and an analyzer reference (ANAL. REFERENCE), which itself floats on the monochromator reference, and upon which all analyzer voltages float. All hemispherical sector voltages are set up so that the potential difference between inner and outer hemispheres is controlled with a single adjustment. This allows for a direct method of changing the pass energy. All hemispherical sector slit voltages are variable over a wide energy range. Split lens element (deflector) voltages have a convenient two stage control system, which consists of: (1) a lens supply which provides a coarse adjustment of the voltage of both elements simultaneously, and (2) a delta supply, which allows for fine adjustments so that the voltage of each half of the deflector can be inde-

pendently varied either positively or negatively with respect to the lens supply voltage.

The front panel of the supply is set up for convenient adjustment (10-turn and 22-turn potentiometers) and measurement (test points) of all lens potentials. A photograph of the front panel is shown in Fig. 8. The front panel also indicates the relationship of each voltage to the reference potentials and a label indicating the range of all voltages. The panel is color-coded so that the test points and traces for the monochromator and the analyzer are colored blue and gold, respectively. This fact is not obvious from the black-and-white photograph shown here. Another feature of the front panel is the capability to measure the current collected by any lens element. This can be very helpful during the tuning up process. The current measurement is accomplished by disconnecting the lens element from its voltage supply by means of the three sets of rocker switches at the bottom of the front panel. A picoammeter or current amplifier can then be placed in series between that lens element's test point on the upper portion of the front panel (connected to the voltage supply) and its test point at the extreme bottom of the front panel (connected to the spectrometer lens element).

A description of the function of all spectrometer elements has already been given in the previous two subsections. The voltage label corresponding to each element is shown in Fig. 3 (monochromator) and Fig. 6 (analyzer). The voltage ranges available can be gleaned from the photograph of the front panel (Fig. 8). The range of possible voltages available from the hemispherical supply is quite wide, but

after initial tune-up, only small changes are necessary. Note that the supply provides certain voltages which are not spectrometer voltages. The most important of the non-spectrometer voltages are reference voltages (MONO. REFERENCE, which is called IMPACT ENERGY on the front panel) and ANAL. REFERENCE, upon which all monochromator and analyzer voltages are floated. Certain other voltages are used in tuning up spectrometer voltages (Δ PREMONO., Δ MONO., Δ ANAL., PREMONO. LEVEL, MONO. LEVEL, ANAL. LEVEL, A1, A2, A3, B1, B2, C1, C2) but are not directly connected to any lens element on the spectrometer. A discussion of the tune-up procedure and a table of typical operating voltages is given in Subsection 6.

Although the hemispherical EELS supply provides the bulk of the voltages needed in the experiment, several other power supplies are also required (Fig. 7). These are the filament supply, the electron multiplier supply, and the high voltage divider box. The pulse counting electronics will be discussed in Subsection 5.

To provide the necessary sweep voltage for taking an EELS spectrum, a voltage step is provided by the digital-to-analog converter (DAC) board of the LSI-11/2 microprocessor. This voltage step is added linearly to each of the analyzer voltages. The DAC is configured to provide 4096 increments of 2.5 mV each, for a total range of 0 to +10.24 V. This step is attenuated by an operational amplifier whose gain may be changed by adjusting a 22-turn potentiometer on the front panel. For all work in this thesis, the gain was set to 0.04959, resulting in a voltage step size of 0.1240 mV per DAC channel. This corresponds to an energy step size in the EELS spectra of 1.000 cm^{-1} per DAC channel.

Larger step sizes, in integral multiples of 1 cm^{-1} , can then be set up using software instructions.

The filament supply (LAMBDA LP-520-FM) provides 0 to 10 V, 0 to 5 A output, and can be operated in either the voltage or current limited mode. It is used to power the filament in the electron monochromator, which usually requires about 2.8 V and 2 A to operate optimally. The inputs from the filament supply to the hemispherical EELS supply are FIL+ and FIL-. The filament level (the voltage half way between FIL+ and FIL-) can be floated with respect to the monochromator reference by adjusting the FILAMENT LEVEL pot on the front panel of the hemispherical supply. In normal operation, FILAMENT LEVEL is set at the same voltage as MONO. REFERENCE. The filament supply has been found to be extremely clean and stable, and thus provides a constant level of filament emission current over time. This fact removes the need for the emission stabilization circuit which is built into the hemispherical supply, but is not currently being used.

The electron multiplier supply (Hewlett-Packard Model 6110A) is rated at 0-3000 V, 0-6 mA, and has two SHV output connectors, PLUS AND MINUS. These two voltages are carried to the high voltage divider box, where they are used to produce operating voltages for the Spiraltron electron multiplier. The multiplier INPUT voltage is actually set on the hemispherical supply. The high voltage divider box has a string of resistors and zener diodes which distribute the PLUS voltage in order to create the other two multiplier voltages, OUTPUT and BIAS. OUTPUT equals (PLUS-200) volts above INPUT, and BIAS equals PLUS volts above INPUT. The BIAS voltage actually carries the electron pulses

from the collector located directly behind the electron multiplier. The pulses are then decoupled from the high voltage and counted.

5. Pulse Counting and Data Acquisition Electronics.

In this section, the electronics which take pulses from the electron multiplier, count them, and accumulate, store and display the resulting data will be described. An overview of these electronics is presented in Fig. 9.

After leaving the vacuum chamber, pulses (5 mV average amplitude) are isolated from the BIAS voltage in the pulse decoupling box. The pulses are then fed into the pulse counting pre-amp, a box which contains a voltage sensitive pre-amplifier, a discriminator, and a shaper, which produces a square wave with 4 volts amplitude. The output of this pre-amp box is fed into a digital ratemeter (Ortec 776 counter-timer). Accumulation of counts is controlled by the LSI-11/2 micro-processor, which reads the ratemeter by means of a 16-bit parallel I/O board at the completion of a counting period. The timing of data acquisition is controlled by the clock board in the microprocessor backplane.

The process of spectrum generation, including the necessary software, will be described in Subsection 7. Here, the microprocessor hardware and the peripheral devices used in data acquisition will be described briefly. A summary of each LSI-11/2 board, including its commercial name, position in the backplane, function, associated peripheral device (if any), and base address (if any) is given in Table 1. Some of the boards (DAC, parallel I/O, clock) have already been men-

tioned. Many of the computer boards are used to interface the microprocessor with other devices (called peripherals). At present, these peripheral devices are: (1) a terminal with video graphics and hard-copy capabilities (DEC VT55-FE), through which the experimenter communicates with the microprocessor, (2) a floppy diskette drive (Data Systems Design 440), which is used for data storage, (3) a line printer (DEC LA 120), used to generate printed copies of the digital data, (4) a point plotter (Hewlett-Packard 7220A) for high quality spectral plots, and (5) two display scopes (Tektronix 620 and Hewlett-Packard 143A), which are used for continuous viewing of spectra during and after accumulation and during tune-up. The use of two scopes allows the spectrum to be viewed while working at the vacuum chamber as well as at the power supply. This is particularly useful during tune-up.

6. Tuning Procedure.

Tuning up a high resolution EELS spectrometer has been compared by some to a bad dream. It certainly requires the patience of Job.¹⁵ The most difficult aspect of tuning up is the initial attempt to get current from the filament to travel through the entire spectrometer into the detector. Tuning up is much easier if one finds the beam with high pass energies in the monochromator and analyzer (3-4 eV) and then "tunes down" to operating pass energies (0.5-1.0 eV) without losing the beam in the process. This strategy can result in a tremendous savings of time, compared with finding the beam at operating pass energies.

Before tuning up, it is necessary to bake out the spectrometer and vacuum chamber and to clean and anneal the sample. The filament and power supplies must be turned on and allowed to settle, and the sample brought into proper position in the EELS plane. Monochromator voltages are then set to reasonable initial values. At this point, the impact energy (the kinetic energy of the beam incident on the sample) is selected by adjusting the MONO. REFERENCE voltage. MONO. REFERENCE is referred to as IMPACT ENERGY on the front panel. This is because the crystal is usually at ground, so that the voltage difference between MONO. REFERENCE and ground attracts electrons from the filament to the sample, causing them to hit the sample with a kinetic energy of $e(\text{GROUND} - \text{MONO. REFERENCE})$, where e is the charge of the electron. The current to the pre-monochromator entrance slit is then maximized by adjusting voltages on the A lens and the repeller. Currents to the various lens elements are measured with a current amplifier (Keithley 427) combined with a digital voltmeter (Keithley 179). With the pre-monochromator and monochromator pass energies set to about 3 eV, the current collected by the outer hemisphere of the monochromator is then tuned for a maximum. During each step of the tuning process, all voltages seen by the beam prior to its arrival at the present tuning location must be readjusted. Next, current to the crystal is optimized using primarily the hemisphere and A lens voltages. At this high pass energy, currents of approximately 1 nA can usually be attained. Unfortunately, this measurement is sensitive to current hitting anywhere on the sample mounting plate, not just a 0.1 mm^2 spot on the crystal. Consequently, considerable retuning is sometimes re-

quired to get current into the C (analyzer) lens. At this point, it is very important to ensure that the monochromator is producing a well-tuned, monoenergetic beam. This can be checked in two ways. First, as the filament current is increased, the current to the sample should go through a maximum in the region of 1.9-2.1 A filament current and then drop sharply. Second, the sample current should also go through a sharp maximum as a function of each hemisphere voltage.

Now that a monochromatic beam is being delivered to the sample, the next step is to move the sample and analyzer to the proper angles so that the analyzer lens is accepting the specularly reflected beam. The sample can be lined up with the X and Y horizontal-positioning micrometers, the Z vertical position drive, the θ rotary position mechanism, and the tilt micrometers. The analyzer can be moved in both the vertical and horizontal planes using the rotary motion feed-throughs. The rotary position of the sample and the horizontal and vertical position of the analyzer are especially critical, as over 99 percent of the scattered elastic intensity in EELS is found within a few degrees of specular reflection. With the analyzer set at a high pass energy, the next step is to turn on the Spiraltron electron multiplier and try to get current through the hemispherical analyzer and the exit slits, at which point counts will be observed. The count rate is then maximized by tuning up all spectrometer voltages and re-positioning. At any point, the crystal may be biased above or below ground, but it is generally wise to keep the crystal grounded until the final tune-up. Caution must be observed at this stage because count rates may significantly exceed 100-200 kHz in the elastic chan-

nel at these high pass energies, causing a substantial decrease of multiplier gain. This can be avoided by turning down the electron multiplier supply voltage.

Once the maximum count rate is observed, the pass energies can be turned down. This must be done gradually, to ensure that the beam is not lost. Decreasing the pass energies is usually carried out first in the monochromator, then in the analyzer, by turning down the delta pots on the front panel (Δ PREMOND., Δ MONO., Δ ANAL.). These pots set the potential difference between hemispheres, which is proportional to pass energy. The slit voltages, and the MONO. LEVEL and ANAL. LEVEL voltages, which determine how high the hemisphere voltages float above their respective reference voltages (MONO. REFERENCE and ANAL. REFERENCE), must also be turned down at this stage. At operating pass energies, the current to the sample is about 2×10^{-10} A, and the count rate measured at the detector may be as high as 300 kHz (equivalent to 5×10^{-14} A).

Once the pass energies have been reduced to their final settings (ca. 0.75 eV), the last stage of tuning up begins. Here we attempt to simultaneously maximize the intensity in the elastic peak and minimize both the elastic peak width and the inelastic background. At this stage, an effort is made to reduce the potential difference between split deflector pairs, mostly in the B and C lenses. The crystal bias may also be used to compensate for work function differences, especially after adsorbate gas exposures. To assist with the final tune up, a computer program (named TUNE) has been written. TUNE allows the entire spectrum or any part of it to be continuously scanned and dis-

played while voltages, and sample and analyzer positions, are varied. The spectrum can be displayed on either a log or a linear scale. Once maximum count rate in the elastic channel has been obtained, TUNE is used to minimize the width of the elastic peak, hopefully without sacrificing the optimized count rate. It is then used to suppress the inelastic tail and the widths of inelastic peaks. The entire tuning process, including the use of the TUNE program, is an iterative procedure. Frequently, one finds many local optimizations of operating conditions before reaching a global optimization. In fact, there may be many sets of optimization conditions which yield almost identical resolution and count rate. The log scale display is particularly useful, as many inelastic losses are 2-4 orders of magnitude weaker than the elastic peak, and do not show up on the linear scale.

For off-specular EELS experiments, the spectrometer must first be tuned up in the specular direction. Then the analyzer (or sample) is rotated by a specified amount to the desired geometry. A modified tune up procedure is then undertaken at the new experimental geometry. Generally, it is fairly easy to retune at off-specular angles. It is, however, important to be aware that the intensity in the elastic peak drops by a factor of $\sim 10^3$ at 10° away from the specular direction.

Consideration must also be paid to dark counts, because even a few dark counts per second may obscure a weak loss feature. The electron multiplier itself can be a significant source of dark counts, but we have chosen a Spiraltron which produces less than 0.1 count per second in the absence of external electron sources. The Spiraltron, as well as the entire path of the electron beam, must be well shielded from

electrons (from external sources such as the ion pump, the ion gauge and the tungsten filament) which bounce off the spectrometer or vacuum chamber walls.

Typical values of all monochromator, analyzer, and sample voltages are listed in Table 2. It is convenient to reference all voltages in this table to the voltage of the filament center (MONO. REFERENCE), which is the voltage at which electrons have zero kinetic energy.

7. Software and Spectrum Generation.

The main FORTRAN computer programs used to run the EELS spectrometer are SINGLE, which is the data acquisition program, and SINBK1, which is the data reduction program. The TUNE subroutine, described above, is part of the SINGLE program. All assembly language routines are included in a MACRO routine called ELSSP1. During data acquisition periods the microprocessor is operated in the foreground/background mode. The SINGLE program is the foreground job, and controls all steps in the generation of spectra. While the ratemeter is accumulating counts (usually over 99 percent of the time during spectrum generation), the foreground job can be suspended and the background job activated. During these periods, data analysis can be done by the SINBK1 program in the background job. At the completion of each accumulation period, the real-time clock interrupts the background job and restarts the foreground job again. This process is repeated throughout the generation of a spectrum.

A brief description of the SINGLE program will now be given. The program begins with the subroutine ARPIN, in which the following spec-

tral parameters are entered: the number of channels (NCH), the number of wave numbers per channel (MEVPCH), the memory divisor (MD), the number of scans (NS), the number of milliseconds per channel (NMSEC), four parameters describing the sample and analyzer positions (ANALHO, ANALVE, RP, ZPOS), and the monochromator and analyzer voltage references and pass energies (XMR, XAR, XMPE, XAPE). The number of wave numbers per channel has been set to 1.000 on the hemispherical power supply. Entering a memory divisor of an integer greater than one will set up larger step sizes. Consequently, the new control parameters are $NCH=NCH'/MD$ channels and $MEVPCH=MEVPCH'*MD$ wave numbers per channel, where NCH' and MEVPCH' are the parameters originally entered. The ARPIN subroutine then clears the spectral array (SPEC) and returns to the main program.

In the main program, two nested do loops are used to collect a spectrum. The outer loop carries out NS repetitions of a single scan and the inner loop controls the accumulation of data into NCH channels during each scan. The accumulation of one scan proceeds in the following manner. The ratemeter is cleared and counting is enabled by the real-time clock. The spectrum accumulated thus far is displayed on the scopes and the foreground job is suspended, activating the background job. This status continues until the clock times out after NMSEC milliseconds, at which point the foreground job is restarted, counting is stopped, and the ratemeter is read into the proper channel of the spectral array. The analyzer voltages are then stepped by MEVPCH wave numbers by the DAC, and the whole process, starting with clearing the ratemeter, is repeated NCH times to accumulate one scan.

After the completion of NS scans, the program offers the choice of starting a new spectrum, taking more scans of the present spectrum, or storing the present spectrum in a temporary file on a floppy diskette. If the latter option is chosen, the data may then be read into the background job (SINBK1). Here, one can print, plot, display or manipulate the spectrum or store it permanently on a floppy diskette.

Analyzer voltages are stepped in a positive direction, meaning that the highest kinetic energy region (around the elastic peak) will be found in the initial portion of the spectrum and the inelastic losses later on. The voltage step can be added linearly to all analyzer voltages over the entire range of the spectrum, because the entire energy region of interest in EELS ($4000 \text{ cm}^{-1} \approx 0.5 \text{ eV}$) is so small that the focusing and transmission properties of the C lens do not change appreciably over this range. This is quite different from high resolution photoelectron spectroscopy, where spectra are taken with much larger energy ranges and programmable power supplies are sometimes needed to maintain constant lens transmission.⁵

C. PERFORMANCE

Perhaps the best way to describe the performance of the spectrometer is to show a typical spectrum obtained during the course of an experiment. A spectrum of clean Cu(001) is shown in Fig. 10 as an example. The pass energies used for this spectrum were 0.65, 0.65 and 1.30 eV in the pre-monochromator, monochromator and analyzer, respectively. This corresponds to a total theoretical FWHM resolution, of 3.6 meV, or 29 cm^{-1} . The observed resolution is 32 cm^{-1} , very close

to theoretical, indicating that the spectrometer is operating quite well and that the effects of non-ideal behavior on the FWHM resolution have been minimized. This spectrum was taken in the specular direction with a total scattering angle of 130° between monochromator and analyzer. The count rate in the elastic channel was 50 kHz, but could have been over 300 kHz had the gain on the electron multiplier been turned up to its maximum level. Using lower pass energies, a few spectra were obtained with a resolution of 28 cm^{-1} . Note that the FWHM resolution is about equal to the best observed to date.¹

The most important feature of this spectrum is the region of the inelastic tail, as this region contains the inelastic loss peaks which will be present after chemisorption (see Chapter III). The ratio between background intensity and elastic peak intensity is plotted on a logarithmic scale in Fig. 11. At an energy loss of 200 cm^{-1} , for example, this ratio is about .001. It continues to drop until about 700 cm^{-1} below the elastic peak, at which point it levels off at about .00004. Most of the background between 100 cm^{-1} and 700 cm^{-1} is due to scattering from the surfaces of lenses and hemispheres.

The spectrometer was originally designed with a FWHM resolution of about 8 cm^{-1} assuming that we could operate at pass energies of 0.5 eV and with a theoretical $(\Delta E_{1/2}/E_0)$ resolution of .0014 in both the monochromator and analyzer. This requires particularly small slit widths (.07 mm) in the monochromator. At this time, these operating conditions have yet to be realized. Distortions in the electric fields in the hemispherical sectors become quite serious at pass energies below 0.75 eV, so that little or no improvement in resolution is obtained at

lower pass energies. In addition, a substantial decrease in count rate would be expected if the slit widths were reduced from their present values (0.15 mm in the monochromator, 0.25 mm in the analyzer) to the size needed to obtain 8 cm^{-1} resolution (0.07 mm monochromator, 0.13 mm analyzer). Fortunately, our count rate has been so high under present conditions that it may still be acceptable after this change is made.

The purpose of this section is to evaluate the current performance of the spectrometer. Recommendations for further improvements are given in the concluding chapter of this thesis.

REFERENCES

1. S. Andersson and M. Persson, Phys. Rev. B 24, 3659 (1981);
S. Andersson and J. Harris, Phys. Rev. Lett. 48, 545 (1982).
2. J. G. Tobin, private communication.
3. D. Roy and J. D. Carette, Top. Cur. Phys. 4, 13 (1977).
4. S. D. Kevan and D. A. Shirley, Phys. Rev. B 22, 542 (1980); S. D. Kevan, Ph.D. thesis, University of California, Berkeley, 1980, unpublished.
5. J. E. Pollard, D. J. Trevor, Y. T. Lee, and D. A. Shirley, Rev. Sci. Instrum. 52, 1837 (1981); J. E. Pollard, Ph.D. thesis, University of California, Berkeley, 1982, unpublished.
6. H. Froitzheim, H. Ibach, and S. Lehwald, Rev. Sci. Instrum. 46, 1325 (1975).
7. L. H. Dubois, Ph.D. thesis, University of California, Berkeley, 1980, unpublished.
8. D. Roy, A. Delage, and J. D. Carette, J. Phys. E 8, 109 (1975).
9. C. E. Kuyatt and J. A. Simpson, Rev. Sci. Instrum. 38, 103 (1967).
10. S. Lehwald, H. Ibach, and H. Steininger, Surf. Sci. 117, 342 (1982).
11. C. E. Kuyatt, Electron Optics Lectures, 1967, unpublished.
12. J. A. Simpson and C. E. Kuyatt, J. Appl. Phys. 37, 3805 (1966).
13. E. Harting and F. H. Read, Electrostatic Lenses (Elsevier, Amsterdam, 1976).
14. J. E. Katz, P. W. Davies, J. E. Crowell, and G. A. Somorjai, Rev. Sci. Instrum. 53, 785 (1982).
15. Old Testament, Book of Job.

Table 1. LSI-11/2 microprocessor boards, in order of their position in the backplane.

	<u>Name</u>	<u>Function</u>	<u>Peripheral Device</u>	<u>Base Address</u>
1.	KD11-HA	LSI-11/2 CPU	-----	-----
2.	MSC 4601	32K RAM	-----	-----
3.	KWV11-A	clock	-----	170420
4.	AAV11-A	4-channel DAC	step, display scope	170440
5.	DSD440-L11	DMA I/O	diskette drive	177170
6.	DRV11	16 bit I/O	counter	177770
7.	DLV11-J	4-channel serial I/O	terminal, plotter, printer	176500
8.	DT2762-DI	8-channel ADC	lock-in amplifier	170400

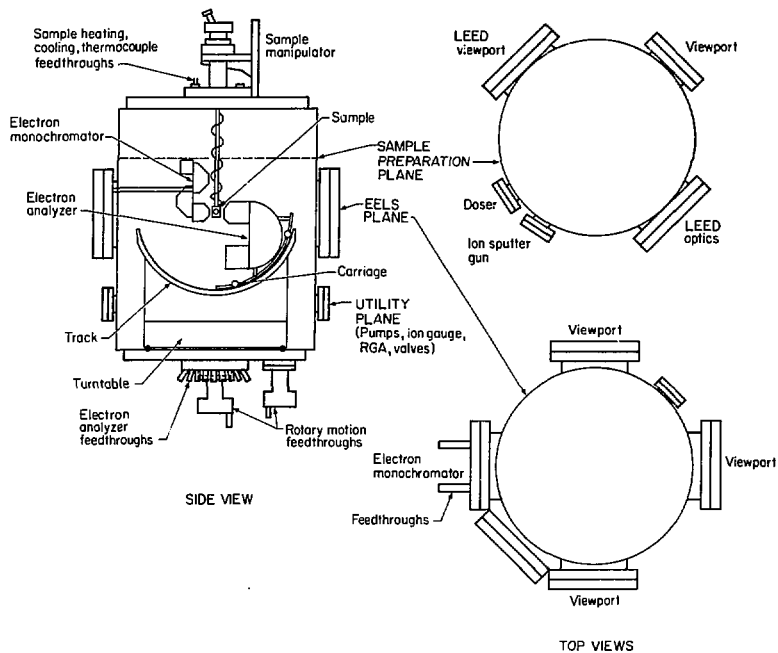
Table 2. Typical voltage settings used in the EELS spectrometer. All voltages are with respect to MONO. REFERENCE, the voltage of the filament center, at which electrons have zero kinetic energy. The pass energies corresponding to these settings are 0.65, 0.65, and 1.30 eV in the pre-monochromator, monochromator, and analyzer, respectively.

<u>Monochromator (19)</u>	<u>Analyzer (15)</u>
FIL+ = + 1.4	COMMON (GROUND) = + 2.000
FIL- = - 1.4	$\Delta C1$ LEFT = + 4.061
REPELLER = - 0.018	$\Delta C1$ RIGHT = + 3.910
$\Delta A1$ RIGHT = + 10.424	$\Delta C2$ UPPER = + 1.157
$\Delta A1$ LEFT = + 9.018	$\Delta C2$ LOWER = + 1.110
$\Delta A2$ UPPER = + 41.776	ANAL. SLIT = + 0.255
$\Delta A2$ LOWER = + 39.796	ANAL. INNER = + 1.011
$\Delta A3$ LEFT = - 3.913	ANAL. OUTER = + 0.391
$\Delta A3$ RIGHT = - 3.190	VS1 = + 0.909
MONO. SLIT = - 0.163	VS2 = + 0.802
PREMONO. INNER = + 0.359	VS4 = + 0.602
PREMONO. OUTER = - 0.039	VS5 = + 0.495
MONO. INNER = + 0.273	INPUT = + 0.682
MONO. OUTER = - 0.126	OUTPUT = + 2400.
$\Delta B1$ UPPER = - 0.301	BIAS = + 2600.
$\Delta B1$ LOWER = - 0.201	
$\Delta B2$ LEFT = - 0.323	<u>Sample</u>
$\Delta B2$ RIGHT = - 0.974	CRYSTAL BIAS = + 2.000
COMMON (GROUND) = + 2.000	

FIGURE CAPTIONS

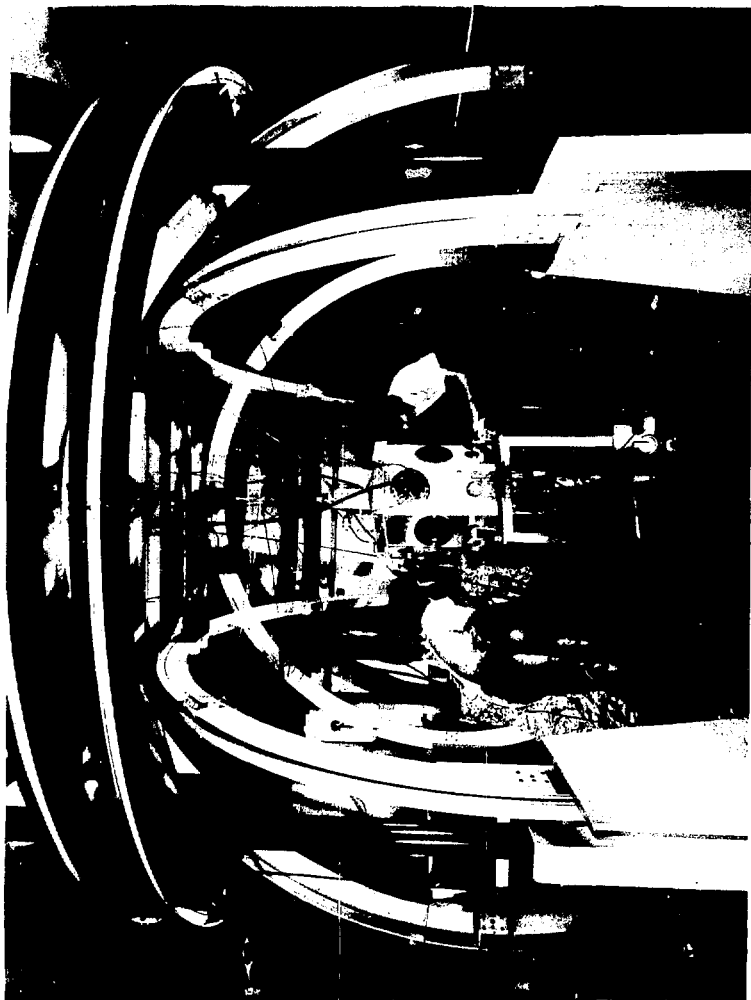
- Figure 1. Schematic of the EELS vacuum chamber, exhibiting an overall side view and top views of the sample preparation and EELS planes.
- Figure 2. Photograph of the vacuum chamber positioned in the center of the Hemholtz coils.
- Figure 3. Cross-sectional illustration of the electron monochromator.
- Figure 4. Photograph of the electron monochromator and mounting flange.
- Figure 5. Close-up photograph of the electron monochromator.
- Figure 6. Cross-sectional illustration of the electron energy analyzer.
- Figure 7. Schematic of the power supplies.
- Figure 8. Photograph of the front panel of the hemispherical power supply.
- Figure 9. Schematic of the pulse counting and data acquisition electronics.
- Figure 10. EELS spectrum of clean Cu(001) taken in the specular direction.
- Figure 11. Plot of the ratio of background intensity (I_{back}) to elastic peak intensity (I_{elastic}) as a function of electron energy loss, for the spectrum in Fig. 10.

EELS SPECTROMETER



XBL 828-11332

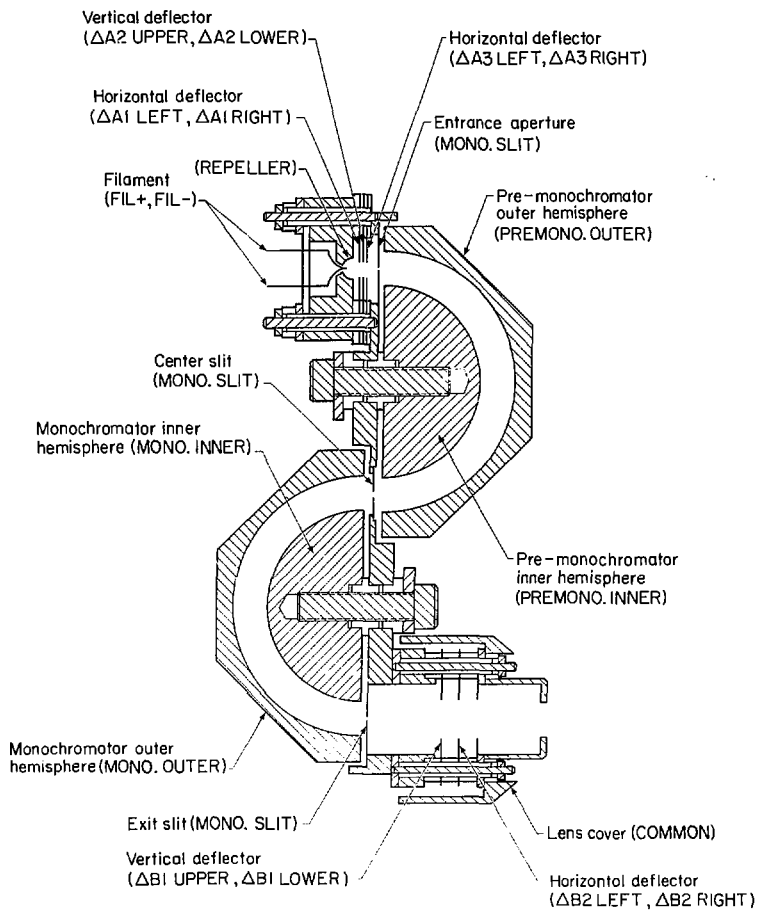
Fig. 1



CBB 827-6028

Fig. 2

EELS ELECTRON MONOCHROMATOR



XBL 827-7116

Fig. 3

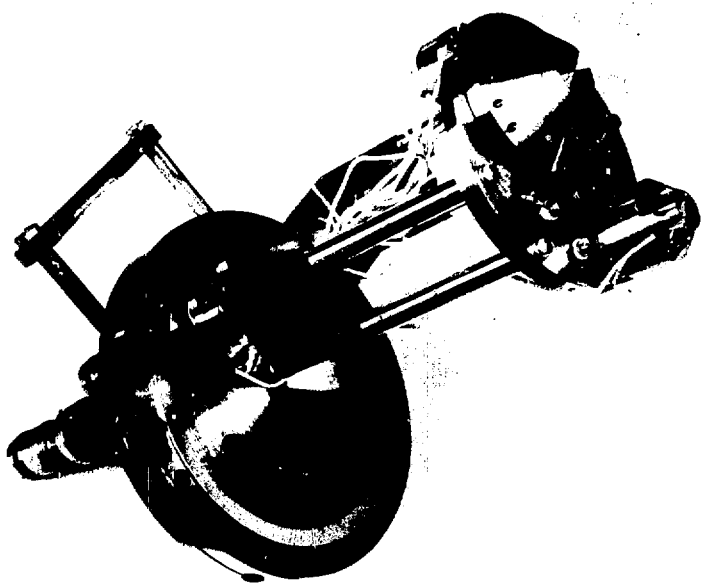


Fig. 4

CBB 827-6020

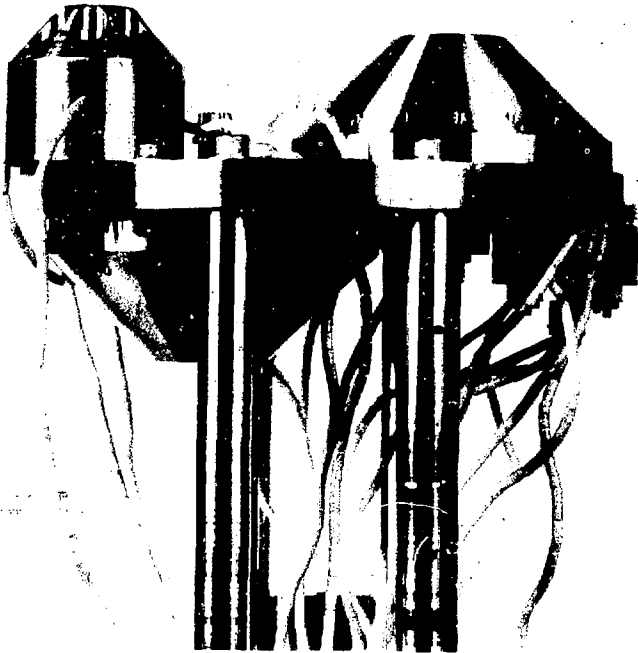
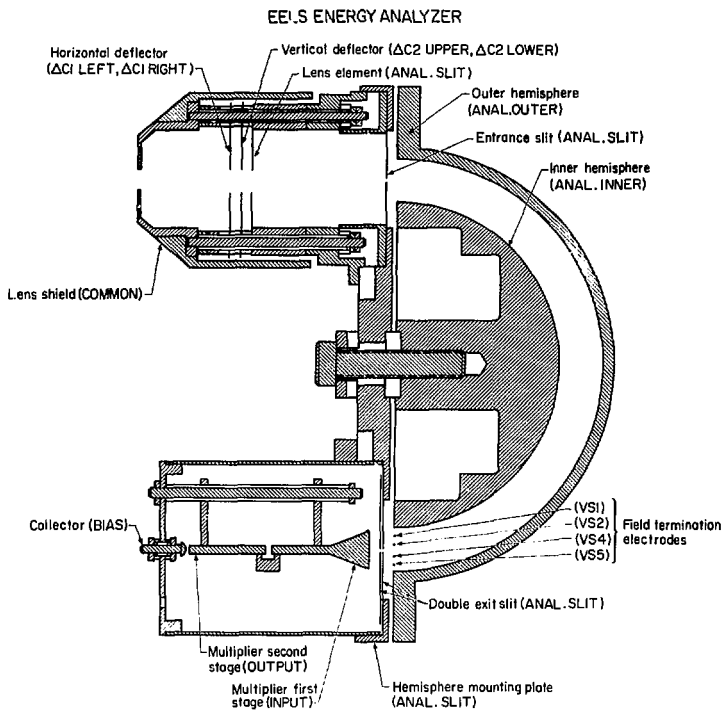


Fig. 5

CBB 827-6026



XBL 827-7115

Fig. 6

EELS POWER SUPPLIES

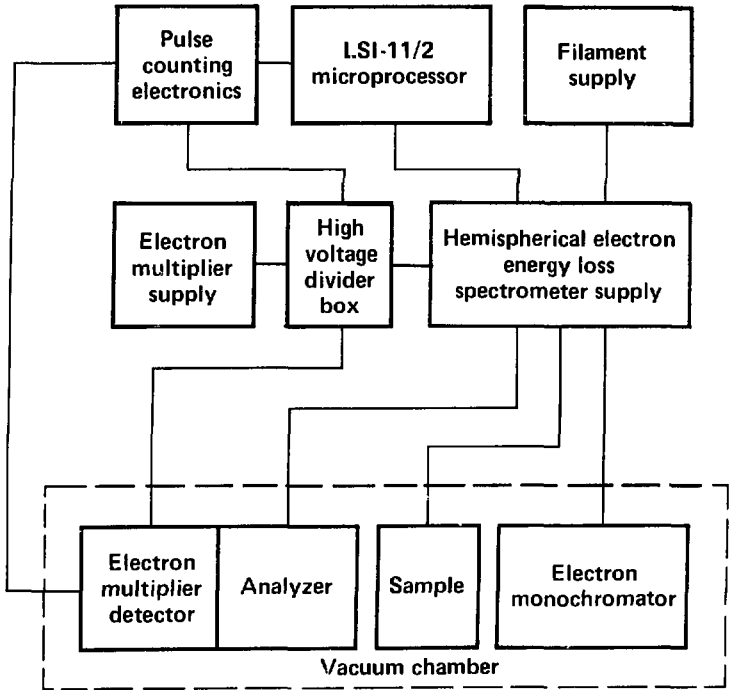


Fig. 7

XBL 827-7123

PULSE COUNTING AND DATA ACQUISITION ELECTRONICS

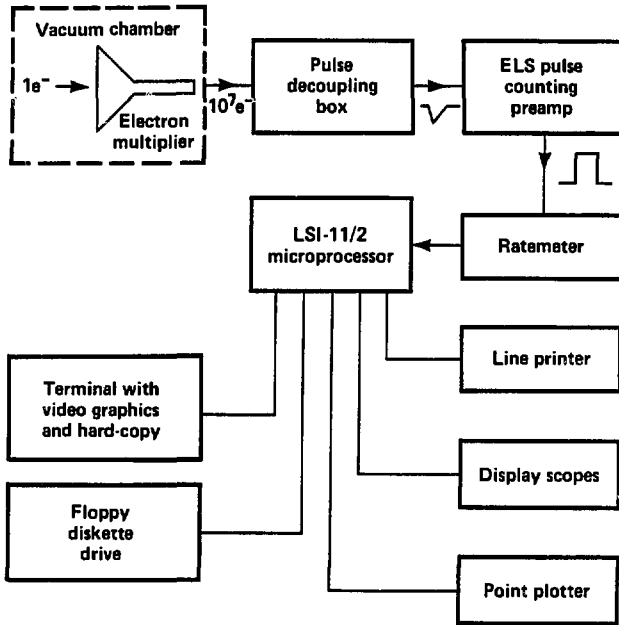
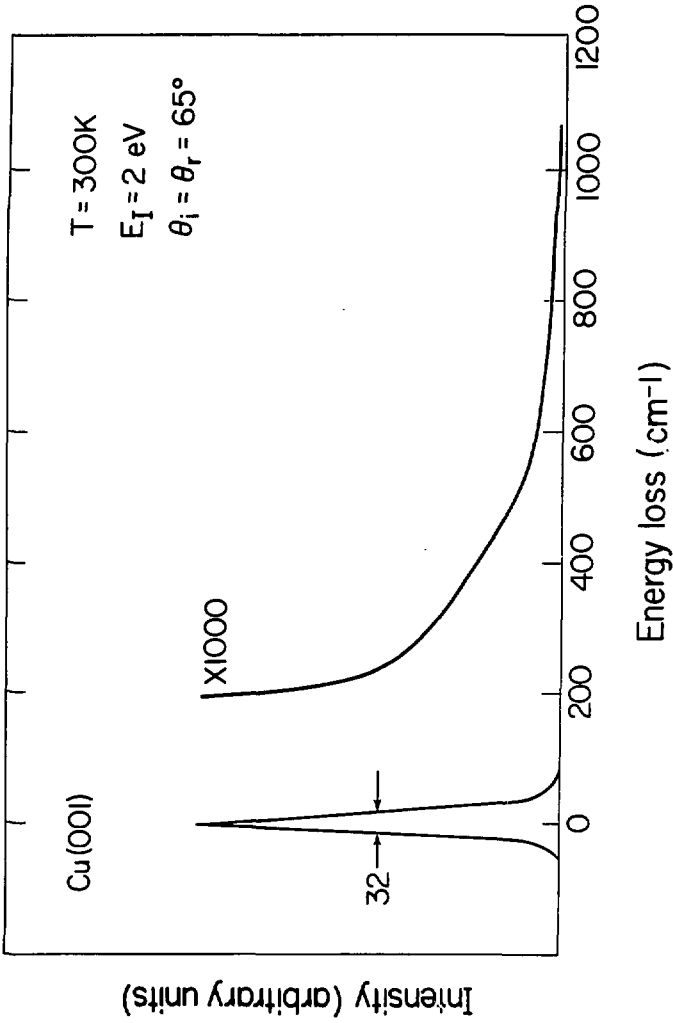


Fig. 9

XBL 827-7121



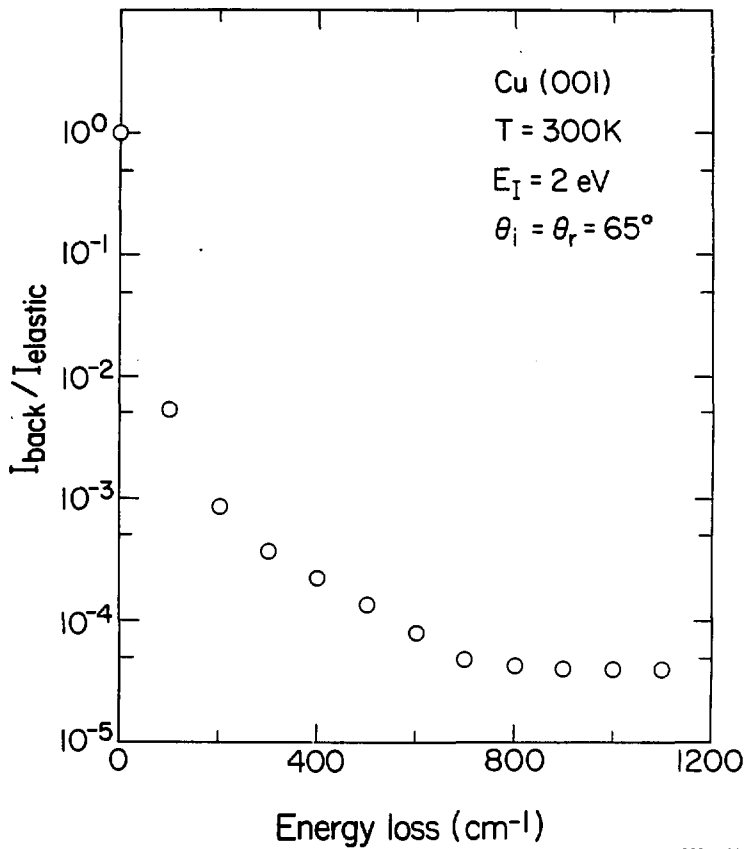


Fig. 11

XBL 829-4620

III. HIGH RESOLUTION ELECTRON ENERGY LOSS SPECTROSCOPY OF OXYGEN ADSORBED ON Cu(001)

A. INTRODUCTION

The surface structure of oxygen adsorbed on Cu(001) has been the object of much controversy in recent years. Oxygen atoms form two ordered overlayers on Cu(001), which are the $c(2 \times 2)$ or $(\sqrt{2} \times \sqrt{2})R45^\circ$ at low exposures and the $(\sqrt{2} \times \sqrt{2})R45^\circ$ at higher exposures. Most of the accurate structural studies have concentrated on the $c(2 \times 2)$ oxygen overlayer. Four studies of this overlayer, each done by a different technique, have yielded four different surface structures. The results of these experiments can be summarized as follows, where d_\perp refers to the perpendicular spacing between O and Cu layers: normal photoelectron diffraction (NPD) - hollow site, $d_\perp = 0.80 \pm 0.05 \text{ \AA}$;¹ azimuthal photoelectron diffraction (APD) - hollow site, $d_\perp = 0.0 \pm 0.1 \text{ \AA}$;² low energy electron diffraction (LEED) - bridge site, $d_\perp = 1.4 \text{ \AA}$;³ and angle resolved secondary ion mass spectroscopy (ARSIMS) - hollow site, $d_\perp = 1.2 - 1.5 \text{ \AA}$.⁴ It is important to note that the discrepancy between the various results may be partially due to the procedures used to prepare the $c(2 \times 2)$ overlayer. In particular, care must be taken to compare the oxygen exposures and annealing procedures used.

The oxygen on Cu(001) system has also been studied by electron energy loss spectroscopy (EELS). By providing vibrational frequencies of some of the surface modes, EELS often yields qualitative structural information. Sexton published EELS spectra of two different coverages of oxygen on Cu(001), resulting from exposures of 50 and 1500 L of

oxygen gas with the crystal at 470 K.⁵ He did not have an in situ LEED capability at the time of the experiment. Both EELS spectra showed a single loss peak, which was measured to be at 330 cm^{-1} for the low coverage overlayer and 290 cm^{-1} for the high coverage structure. These spectra were taken in the specular direction, and the single loss peak was assigned to the stretching vibration of the oxygen atom perpendicular to the surface. The observation of an intense peak at these low frequencies as well as evidence from other techniques indicates that oxygen is atomically adsorbed on Cu(001) at all coverages.⁵

In this chapter, we present an extension of Sexton's measurements to other coverages and to the off-specular direction. In Section B, experimental details are given. In Section C, we present the EELS data and a discussion of the vibrational frequencies observed.

B. EXPERIMENTAL

EELS spectra were measured with the spectrometer described in Chapter II. The base pressure of the vacuum chamber was 2×10^{-10} torr during all measurements. The Cu(001) crystal was oriented to within 1° of the [001] direction. The crystal was cleaned by hot (900 K) and room temperature cycles of argon-ion sputtering and then annealed to 800 K, after which Auger electron spectroscopy showed only trace amounts of carbon and no other impurities. The crystal exhibited a sharp (1x1) LEED pattern after annealing. Oxygen exposures of 400 and 4000 L (1 L = 10^{-6} torr-sec) were made using an effusive beam doser which was brought to within 1 cm of the sample, producing a

localized oxygen pressure which is a factor of 80 greater than the ambient pressure of the vacuum chamber.^{1,5} Consequently, the chamber pressure was never higher than 3×10^{-8} torr during the beam-dosed oxygen exposures. Exposures between 0.5 and 200 L were made by conventional ambient dosing at pressures between 1×10^{-8} and 8×10^{-8} torr with the chamber ion pump on. The sample was briefly annealed to 475 K at the completion of the exposures to promote ordering of the overlayer. Exposures of 200 and 4000 L were necessary to obtain $c(2 \times 2)$ and $(\sqrt{2} \times 2\sqrt{2})R45^\circ$ LEED patterns, respectively. All spectra were taken with the sample at 300 K. For all spectra shown below, the spectrometer was operated with pass energies of 0.65 eV in the pre-monochromator and monochromator and 1.30 eV in the analyzer. This corresponds to a theoretical FWHM resolution of 29 cm^{-1} . The observed resolution of individual spectra ranged from 31 to 36 cm^{-1} . The count rates were typically 50–75 kHz in the elastic channel, 100–1000 Hz for the inelastic loss peaks, and $< 25 \text{ Hz}$ for the background in the region of the O–Cu stretching vibration. The impact energy used was 2 eV, and spectra were taken in the specular scattering direction with a total scattering angle of 130° except for the two off-specular spectra (see below).

C. RESULTS AND DISCUSSION

In this section, results of the oxygen on Cu(001) EELS study are presented. Spectra were taken in the specular direction for a series of oxygen exposures ranging from 0.2 L to 4000 L. Some of the spectra are shown in Fig. 1. The oxygen exposure, the observed LEED pattern, and a rough estimate of the fractional coverage of oxygen atoms corre-

sponding to each spectrum is given. For exposures less than 80 L, only a (1x1) LEED pattern, characteristic of the substrate lattice, was observed. The estimate of oxygen coverage was obtained in the following manner. First, the intensity (peak area) of the O-Cu stretching loss peak, normalized to the intensity of the elastically scattered peak, is determined for each spectrum. Then, we assumed that the normalized O-Cu stretching intensity for the c(2x2) overlayer (200 L exposure) corresponds to a one-half monolayer coverage ($\theta = .50$). The fractional coverage of all other overlayers is then obtained by scaling their normalized O-Cu stretching intensity to that of the c(2x2) overlayer. A correlation between the normalized energy loss intensity and the oxygen KLL Auger intensity (normalized to a copper Auger peak) has been observed for this system,⁵ so this method should provide a rough estimate of the coverage θ .

In Fig. 1, a complex shift of the O-Cu stretch towards lower frequency with increasing oxygen exposure (and coverage) is observed. At very low coverages, there is a single peak at a frequency of about 350 cm^{-1} . It shifts gradually to about 340 cm^{-1} for a surface exposed to 5 L of O_2 , corresponding to about a one-quarter monolayer coverage. Cu(001), unlike the (001) faces of Ni and Rh, does not yield a p(2x2)0 LEED pattern.⁷ As the oxygen exposure is further increased, a complex change in the spectra between 5 L and 50 L is observed. A second peak at 310 cm^{-1} appears after an exposure of 10 L, and this peak grows in intensity as the exposure is increased, while the 340 cm^{-1} peak becomes weaker. By 50 L, the higher frequency peak is gone and the 310 cm^{-1} peak has become sharp. Unfortunately, our

instrumental resolution of 32 cm^{-1} , as well as inhomogeneous broadening of the spectral peaks, makes it difficult to resolve these two features, but it is clear that there are two peaks present in the 10 and 20 L spectra, as well as other spectra not shown here. The 50 L spectra has nearly a one-half monolayer of oxygen coverage. At around 80 L, $c(2 \times 2)$ LEED spots start to appear, and by 200 L, the $c(2 \times 2)$ pattern is sharp. The frequency has shifted further to 300 cm^{-1} . At higher coverages, the $c(2 \times 2)$ pattern develops weak extra spots characteristic of a $(\sqrt{2} \times \sqrt{2})R45^\circ$ overlayer, and by 4000 L, all adsorbate-induced spots are equally intense and sharp, indicating that the formation of the $(\sqrt{2} \times \sqrt{2})R45^\circ$ overlayer is complete. The frequency at this point has downshifted slightly to 290 cm^{-1} . An ideal $(\sqrt{2} \times \sqrt{2})R45^\circ$ overlayer has a coverage of three-quarters of a monolayer; at 4000 L we calculate roughly $\theta = .84$. No attempt was made to produce a bulk copper oxide on Cu(001), because large exposures (10^7 L) are required,⁸ which would create both vacuum problems and large spectrometer work function changes.

The existence of two different O-Cu stretching frequencies at intermediate coverages is quite interesting. At least four explanations are possible. First, these results might be interpreted in terms of oxygen atoms in two different adsorption sites. Other explanations do not require a change in site. Let us assume that oxygen bonds in the fourfold hollow site on Cu(001), as this is the result from three out of the four structural studies of the $c(2 \times 2)O$ overlayer and is also the site for O-Ni(001). A second possible interpretation is that oxygen atoms are bonded with two different d_{\perp} spacings. For example, in

the $\theta = .25$ overlayer, oxygen atoms could be bonded significantly above the surface, while in the $c(2 \times 2)$ overlayer, they could have moved closer to the surface, leading to a decreased frequency.^{2,9,10} The spectra for 5 - 50 L oxygen exposure would then indicate the presence of both sites, with a continuous shift in their relative population as a function of coverage. A third possibility is that oxygen in fourfold hollow sites could draw its four nearest neighbor copper atoms closer together at low coverages. As more oxygen was added to the surface, adjacent hollow sites would be filled in, pulling the copper atoms back to the original positions they occupied on the clean surface. This would change the O-Cu bond length without changing d_L , and could lead to a frequency shift. Small changes in the top substrate layer probably would not alter the (1×1) LEED pattern seen below $\theta = .5$ substantially. The final possibility to be discussed is that the bonding geometry does not change and that the frequency shift is due to some other factor which changes the vibrational force constant. At $\theta = .25$, each copper in the hollow site has, on the average, only one nearest-neighbor oxygen atom. The oxygen atoms are far enough apart so that each Cu_4O cluster is isolated from the nearby complexes. In the $c(2 \times 2)$ overlayer, however, each copper is bonded to two oxygen atoms, and simultaneously participates in two O-Cu stretching vibrations perpendicular to the surface. This could lead to a smaller force constant and consequently a lower vibration frequency without any structural change. At coverages between $\theta = .25$ and $\theta = .50$, both singly- and doubly-oxygen-bonded copper atoms are present on the surface. This could explain why two peaks are observed in the vibrational spectrum.

Lehwald and Ibach¹¹ have obtained similar coverage dependent results for oxygen adsorbed on Ni(001). For the p(2x2)0 overlayer, a single peak at 430 cm^{-1} was observed. At higher coverages, this peak gradually decreased in size while a new peak at around 330 cm^{-1} grew in. Upon the development of a sharp c(2x2) LEED pattern, only a peak at 310 cm^{-1} was present in the spectrum. The 120 cm^{-1} shift in stretching frequency between p(2x2) and c(2x2) oxygen overlayers on Ni(001) is much larger than the shift we observe for O on Cu(001), but the evolution of the O-Ni(001) spectra as a function of coverage is remarkably similar to our results. In addition, the results of structural studies of the p(2x2)0 and c(2x2)0 overlayers on Ni(001) with the techniques of LEED, NPD, and SEXAFS (see Chapter IV and references therein) indicate that the geometric structure of these two overlayers is the same; i.e., the oxygens are located at $d_{\perp} = 0.8 - 0.9 \text{ \AA}$ above the fourfold hollow sites on Ni(001). To explain the large EELS frequency shift without a change in d_{\perp} , the force constant for O-Ni vibrations has to decrease significantly from the p(2x2) to the c(2x2) overlayer. However, no lattice dynamical theory has been able to predict such a decrease without a corresponding change in d_{\perp} spacing.^{9,10,12} This may be due to the fact that the theoretical models used to date rely on clusters of single oxygen atoms with many nickel atoms. Unfortunately, the effect of neighboring oxygen atoms on the O-Ni stretching frequency has not been studied. Bauschlicher, *et al.*,¹² have proposed to model the c(2x2)O-Ni(001) system by placing several oxygen atoms on a large nickel cluster and performing an *ab initio* calculation of the potential energy function and the vibrational frequency.

This calculation may be able to explain the large frequency shift using the surface structures derived from the diffraction techniques.

The O-Ni(001) EELS interpretation has a strong bearing on the O-Cu(001) system, as the data are so similar. Due to uncertainties about the structure of c(2x2)O-Cu(001), it is difficult to conclude that the observed frequency shift in our data is occurring without a change in d_1 spacing. The possibility does remain, however that the two peaks in the 10 and 20 L spectra correspond to vibrations of copper atoms with one and two nearby oxygen atoms, respectively, where O is located in the fourfold hollow site in both cases.

The NPD study of the O-Cu(001) bonding geometry alluded to above¹ concluded that the $(\sqrt{2} \times \sqrt{2})R45^\circ$ and c(2x2)O overlayers both have the same structure; i.e., oxygen is situated about 0.8 Å above the surface, in the hollow site. The EELS spectra for these overlayers in Fig. 1 both exhibit a peak at about 290-300 cm^{-1} . This tends to support the NPD result, as a change in d_1 or site as the overlayer changes from c(2x2) to $(\sqrt{2} \times \sqrt{2})R45^\circ$ would probably be accompanied by a shift in the energy of the loss peak. In addition, the existence of only one peak for the $(\sqrt{2} \times \sqrt{2})R45^\circ$ overlayer indicates that it is unlikely that even a small percentage of the oxygen atoms are located in a second site.

The low frequency region ($< 250 \text{ cm}^{-1}$) of the spectra in Fig. 1 is also of interest due to the possibility of observing metal surface phonon modes. Andersson and Persson¹³ have demonstrated that information about adsorption sites can be obtained from EELS spectra if one investigates the region below the maximum bulk phonon energy.

In particular, they studied various adsorbates on Cu(001) in the region $110\text{--}240\text{ cm}^{-1}$, which is where bulk phonon modes have been observed by neutron scattering.¹⁴ For a $p(2\times 2)$ S overlayer on Cu(001), two loss peaks at 128 and 188 cm^{-1} frequency (relative intensity $\sim 3:1$) were observed,¹³ which were assigned to two surface phonon modes predicted by a Cu(001) slab calculation.¹⁵ These modes are not seen in the clean Cu(001) EELS spectrum but can be excited if submonolayer amounts of gases are adsorbed into fourfold hollow sites.

We observe similar low frequency modes in the EELS spectra for certain coverages of O on Cu(001). In general, there appears to be at least one peak in the region of 150 cm^{-1} in the 5, 10, 20, and 50 L spectra. Other spectra for both lower and higher exposures show either no peak at all or a much smaller peak at this frequency. Unfortunately, the background of our spectrometer is substantially higher than that of Andersson's at 150 cm^{-1} , so our peaks appear on top of a steeply sloping inelastic tail. This mode could be due to a copper surface phonon, analogous to the phonon-derived peak at 128 cm^{-1} observed by Andersson for $p(2\times 2)$ S-Cu(001) and similar peaks in the $p(2\times 2)$ O-Ni(001) data.¹¹ The coverages at which the low frequency mode is present in our spectra are in the range $\theta = .25\text{--}.46$. Although no $p(2\times 2)$ O overlayer is formed on Cu(001), overlayers in this coverage range should contain small patches which have the basic $p(2\times 2)$ two-dimensional structure with respect to the surface. This would cause excitation of the surface phonons for these intermediate coverages but not at higher coverages like $c(2\times 2)$ or $(\sqrt{2}\times\sqrt{2})R45^\circ$, where the symmetry properties of the overlayer have changed and the probability of exci-

tation of those particular modes has decreased greatly.¹³ The possibility that this mode is due to a vibration involving the oxygen atom cannot be ruled out, however.

Finally, spectra were taken of the $(\sqrt{2} \times \sqrt{2})R45^\circ$ overlayer on Cu(001) at off-specular angles. In Fig. 2, spectra are shown for scattering in the specular direction and 5° and 10° off specular. The angle of incidence (θ_i) of the electron beam was 65° with respect to the sample normal in all three cases. The electron monochromator and the sample were kept stationary while the electron analyzer was rotated from an angle of reflection (θ_r) of 65° with respect to the sample normal to $\theta_r = 60^\circ$ and 55° . The three spectra look very similar; all have a single peak at 290 cm^{-1} , which is assigned to the normal O-Cu stretching vibration. Otherwise, there are no other discernable losses out as far as 2200 cm^{-1} from the elastic peak. The main difference in the spectra is that the count rate in both the elastic peak and the inelastic loss peak dropped by a factors of about 10 and 100 when the analyzer was rotated away from the specular direction by 5° and 10° , respectively. In addition, the intensity of the loss peak (normalized to the elastic peak) was about a factor of 2 higher in the $\theta_r = 60^\circ$ spectrum than in the other two spectra. This may be due to diffraction effects, which have been shown to produce modulations in the loss intensity as a function of angle and impact energy.¹⁶

The main objective of taking off-specular EELS data is to search for losses due to impact-excited modes which are usually vibrations parallel to the metal surface.¹⁶ Observation of these modes may lead to a more complete description of the normal modes of the surface and

may yield qualitative structural information.¹⁷ Unfortunately, all impact modes observed to date have involved the vibration of an H atom with substrate atoms (e.g. H-W(001)¹⁶) or have been C-C or C-H vibrations in a hydrocarbon adsorbate.¹⁸ No impact modes due to vibrations of a surface with an adsorbed atom other than H have been observed. In this work we failed to observe any new modes in the off-specular scattering direction. The existence of impact modes for heavier atoms has been predicted, but the intensity of these modes is expected to be so weak that they would be difficult to resolve even with the best spectrometer available today.¹⁹

In conclusion, the O-Cu(001) system was studied as a function of oxygen exposure. At low coverages, a single peak at 340 cm^{-1} , assigned to the O-Cu stretching vibration, is present. At intermediate coverages, ($\theta > .25$) a second peak at 310 cm^{-1} grows in and gradually replaces the original peak. At the $c(2 \times 2)$ ($\theta = .5$) coverage, the 310 cm^{-1} peak has shifted to 300 cm^{-1} and is the only peak present in the spectrum. At higher coverages, the $(\sqrt{2} \times \sqrt{2})R45^\circ$ overlayer is present and the spectrum exhibits a peak at 290 cm^{-1} . These EELS data are consistent with earlier NPD structural results for O-Cu(001). Off-specular EELS data fail to provide any new insight into the surface structure of this system.

REFERENCES

1. J. G. Tobin, L. E. Klebanoff, D. H. Rosenblatt, R. F. Davis, E. Umbach, A. G. Baca, D. A. Shirley, Y. Huang, W. M. Kang, and S. Y. Tong, unpublished.
2. S. Kono, S. M. Goldberg, N. F. T. Hall, and C. S. Fadley, Phys. Rev. B 22, 6085 (1980).
3. J. H. Onuferko and D. P. Woodruff, Surf. Sci. 95, 555 (1980); D. J. Godfrey and D. P. Woodruff, Surf. Sci. 105, 459 (1981).
4. S. P. Holland, B. J. Garrison, and N. Winograd, Phys. Rev. Lett. 43, 220 (1979).
5. B. A. Sexton, Surf. Sci. 88, 299 (1979).
6. J. G. Tobin, private communication.
7. G. A. Somorjai and M. A. Van Hove, Adsorbed Monolayers on Solid Surfaces (Springer-Verlag, Berlin, 1979), pp. 71-76.
8. C. Benndorf, B. Egert, G. Keller, and F. Thieme, Surf. Sci. 74, 216 (1978).
9. T. H. Upton and W. A. Goddard, III, Phys. Rev. Lett. 46, 1635 (1981).
10. T. S. Rahman, J. E. Black, and D. L. Mills, Phys. Rev. Lett. 46, 1469 (1981); Phys. Rev. B 25, 883 (1982).
11. S. Lehwald and H. Ibach, in Vibrations at Surfaces, ed. R. Caudano, J. M. Gilles, and A. A. Lucas (Plenum, New York, 1982), p. 137.
12. C. W. Bauschlicher, Jr., S. P. Walsh, P. S. Bagus, and C. R. Brundle, unpublished.
13. S. Andersson and M. Persson, Phys. Rev. B 24, 3659 (1981).

14. E. C. Svensson, B. N. Brockhouse, and J. M. Rowe, Phys. Rev. 155, 619 (1971).
15. R. E. Allen, G. P. Alldredge, and F. W. de Wette, Phys. Rev. B 4, 1661 (1971).
16. W. Ho, R. F. Willis, and E. W. Plummer, Phys. Rev. B 21, 4202 (1980).
17. S. Y. Tong, C. H. Li, and D. L. Mills, Phys. Rev. Lett. 44, 407 (1980); Phys. Rev. B 21, 3057 (1980); Phys. Rev. B 24, 806 (1981).
18. A. M. Baro, S. Lehwald, and H. Ibach, in Vibrations at Surfaces, ed. R. Candano, J. M. Gilles, and A. A. Lucas (Plenum, New York, 1982), p. 215.
19. W. A. Goddard, III, private communication.

FIGURE CAPTIONS

Figure 1. EELS spectra of O-Cu(001) as a function of O_2 exposure, taken in the specular direction with both an angle of incidence (θ_i) and an angle of reflection (θ_r) of 65° , and an impact energy of 2 eV. The spectra were taken at 300 K after a brief annealing to 475 K. The magnitude of the exposure, observed LEED pattern (if different from (1x1)), and a rough estimate of fractional oxygen coverage are given for each spectrum.

Figure 2. EELS spectra of the $(\sqrt{2} \times \sqrt{2})R45^\circ$ -O-Cu(001) overlayer as a function of angle of reflection (θ_r). The angle of incidence was $\theta_i = 65^\circ$; the angle of reflection was (a) $\theta_r = 65^\circ$ (specular), (b) $\theta_r = 60^\circ$ (5° off specular), (c) $\theta_r = 55^\circ$ (10° off specular). Other conditions were the same as for Fig. 1.

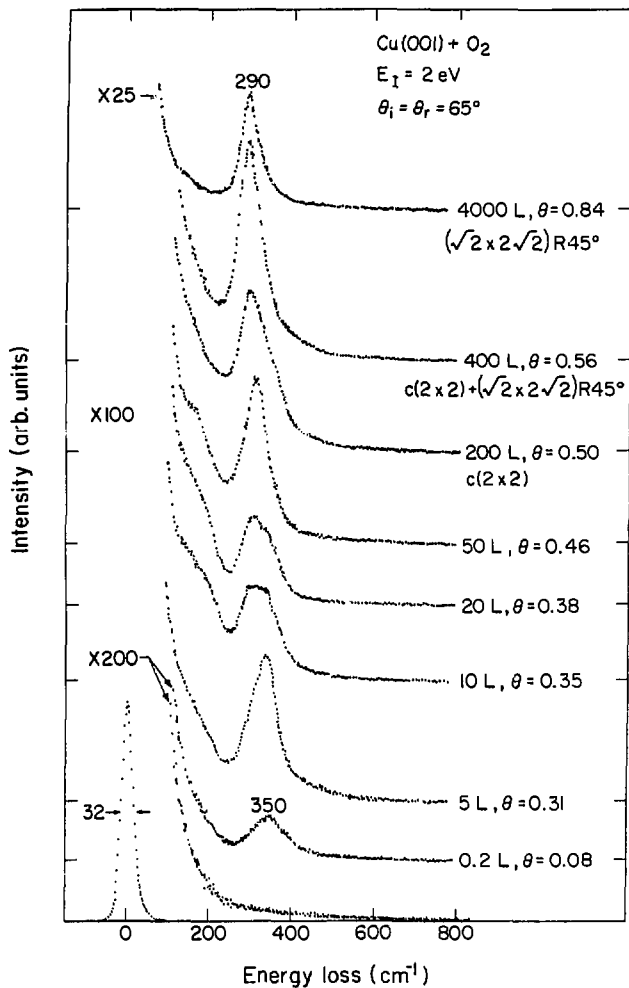


Fig. 1

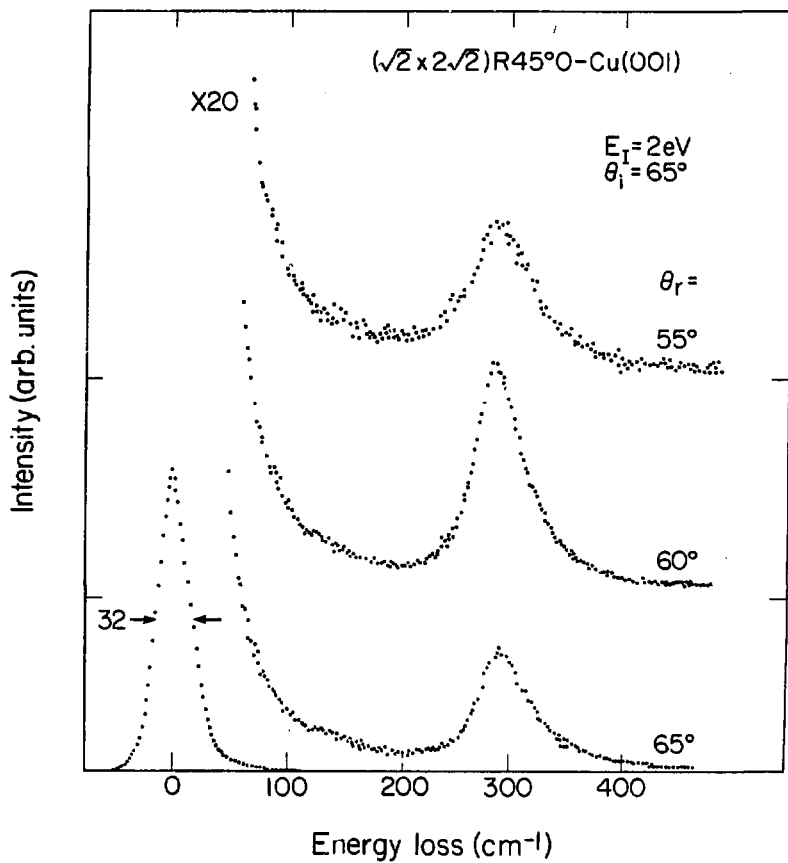


Fig. 2

PART II.

PHOTOELECTRON DIFFRACTION

IV. NORMAL PHOTOELECTRON DIFFRACTION OF $c(2 \times 2)0(1s)-Ni(001)$
AND $c(2 \times 2)S(2p)-Ni(001)$, WITH FOURIER-TRANSFORM ANALYSIS*

A. INTRODUCTION

Normal photoelectron diffraction (NPD) is now established as a method for accurate structure determinations of ordered overlayers of atoms^{1,2} and molecules,³ as well as of disordered atomic overlayers,² on metal surfaces. In an NPD experiment the photoemission intensity of an adsorbate core level is measured normal to the surface as a function of photon, and consequently photoelectron energy. The intensity-kinetic energy curve thus generated is compared to theoretical calculations to make the structure determination. Both experiment and theory bear resemblance to dynamical low energy electron diffraction (LEED), and for all systems in which both methods have been tried to date, the same structure has been obtained. However, existing NPD theories,⁴ based on earlier LEED formalisms, require extensive calculations which thereby limit the method.

Recently, it has been suggested that NPD can be compared with extended x-ray absorption fine structure (EXAFS).⁵ The important structural parameter in NPD, an angle-resolved experiment in which intensity data are taken normal to the crystal face, is d_{\perp} , the perpendicular spacing between the adsorbate layer and the surface layer, whereas EXAFS, an angle-integrated technique, yields the nearest neighbor distance R_{nn} . An inspection of the NPD curves calculated for a series of d_{\perp} distances shows that the peaks move to lower energies as d_{\perp} is increased, resulting in an increased frequency of the

NPD oscillations.⁶ The same effect is observed in EXAFS as a function of nearest neighbor distance, since the oscillations go as $\sin(2kR_{nn})$. This effect was also observed experimentally for the system $p(2 \times 2)\text{Se-Ni}(001)$, where a low temperature form (probably H_2Se) causes a systematic shift in the NPD peaks.⁵ These observations have been borne out by recent theoretical work by Tong and Tang.⁷

In this chapter, we present NPD structure determinations of two additional atomic adsorbate systems, the $c(2 \times 2)$ oxygen and sulfur overlayers on $\text{Ni}(001)$. Again we obtain the same results as the LEED intensity analyses. We also present additional experimental evidence that NPD is similar to EXAFS: We show that experimental NPD data can be Fourier transformed to directly yield interlayer distances along the surface normal. The results of the Fourier transforms are analyzed in light of a new photoelectron diffraction (PD) theory by Barton, et al.⁸

Section B contains the experimental information. In Section C we present NPD data, an R-factor analysis, and a discussion of the surface structures which are derived. In Section D, the first application of the Fourier transform to experimental NPD data is reported. Section E contains some conclusions about this work.

B. EXPERIMENTAL

All data reported here were obtained with an angle resolved photoemission (ARP) spectrometer, described elsewhere.⁹ The spectrometer has low energy electron diffraction (LEED) and Auger electron spectroscopy (AES) capabilities, as well as an adsorbate introduction

system which allows for both ambient dosing and effusive beam dosing. The nickel crystal was oriented to within $1/2^\circ$ of the (001) face. It was cleaned by hot (1025 K) and room temperature cycles of argon-ion sputtering followed by annealing to 875 K, resulting in a surface essentially clean of impurities with a sharp (1x1) LEED pattern. The three ordered structures which have been observed during oxygen adsorption on Ni(001) are the p(2x2) overlayer (~ 0.25 monolayer), the c(2x2) overlayer (~ 0.50 monolayer), and nickel oxide (> 1 monolayer). The real space structure and the reciprocal space LEED pattern for these three overlayers, as well as for clean Ni(001), are shown in Fig. 1. In Fig. 2, a bar graph indicating the observed LEED patterns as a function of oxygen exposure is shown. Clearly, there is considerable overlap between different patterns at certain coverages. Most notable is the overlap between c(2x2) and NiO patterns in the exposure range 60 to 125 Langmuirs ($1\text{L} = 10^{-6}$ torr-sec). This has led to some ambiguity about the characterization of the c(2x2) structure (see the discussion in Section C). We have chosen to study the c(2x2) overlayer at the coverage which produces the sharpest LEED pattern. To obtain this c(2x2) oxygen overlayer, the crystal was exposed to an ambient pressure of 2×10^{-8} torr O_2 . The LEED pattern was continuously monitored during the exposures. After an exposure of ~ 20 L, the last evidence of p(2x2) spots disappeared and the c(2x2) pattern became extremely sharp. The sharpness of the LEED pattern steadily decreased as the exposure was increased above 20 L. Consequently, all $\text{O}(1s)$ data in this chapter were taken from surfaces which were exposed to 20-25 L of O_2 . The c(2x2) sulfur overlayer was prepared by di-

recting an effusive beam of H_2S at the nickel surface. Effusive beam dosing was used to maintain vacuum integrity. An exposure of 20-30 L produced a sharp $c(2 \times 2)$ LEED pattern. All exposures of O_2 and H_2S were made with the sample at 300 K. The base pressure of the chamber was 2×10^{-10} torr.

The experiments were performed on Beam Line I-1 at the Stanford Synchrotron Radiation Laboratory (SSRL). The oxygen experiment was done during a dedicated SSRL run, with a stored ring current of 45-90 mA. The high photon flux available with dedicated running was necessary because of the low photoemission cross section of the $O(1s)$ level. Experiments in the region above the oxygen K-edge (binding energy 537 eV with respect to the vacuum level) are hampered by the high percentage of scattered light, the loss of intensity to absorption by carbon contamination on the optical elements, and the poor resolution of the grasshopper monochromator. The theoretical resolution of the monochromator with a 1200 line/mm grating installed is $\Delta E = 8 \times 10^{-6} E^2$ (eV), or 3.1 eV at a photon energy of 620 eV. The $O(1s)$ natural linewidth for this system at $h\nu = 1487$ is known to be less than 1.5 eV.¹⁰ The resolution of our electron analyzer is less than 0.5 eV at 80 eV pass energy. Assuming a 1.5 eV natural linewidth, a combination of these three factors should give an $O(1s)$ peak width of about 3.5 eV. However, the observed FWHM for $O(1s)$ in this experiment at 620 eV is 7 eV under these conditions. We conclude that the monochromator resolution is about a factor of two worse than theoretical above the oxygen edge. Scattered light was estimated to be about 20 percent in the region above the oxygen edge.⁹

The NPD on the S(2p) level (binding energy 170 eV with respect to the vacuum level) did not require dedicated time because, averaged over the energy range studied, the S(2p) cross section for c(2x2)S-Ni(001) is about five times as large as that of the O(1s) cross section for c(2x2)O-Ni(001). The stored ring current was 10-15 mA during this experiment. Measurement of the relative S(2p) intensity was severely hampered by the sharp dropoff in monochromatized light at and above the carbon K-edge (284 eV), due to absorption by the carbon contamination on the optical elements of the monochromator. The photon flux was monitored continuously during these experiments by measuring the photoyield from a 90 percent transmitting gold mesh placed in the path of the beam.

The O(1s) and S(2p) differential (angle-resolved) relative intensities were mapped out by taking a series of low resolution ARP spectra normal to the (001) sample face in the region of the core level peak. A smooth background was subtracted before calculation of the peak area. The area was then adjusted for photon flux and analyzer transmission. Spectra were taken at intervals of 3 eV in photon energy to generate the NPD curve.

C. RESULTS AND DISCUSSION

In spite of its poor resolution at the higher energies, the grasshopper monochromator, with a 1200 line/mm grating, provides adequate intensity and resolution to permit NPD studies on adsorbate core levels with binding energies in the 100-600 eV range. In this section we report separately on the oxygen and sulfur adsorbate systems.

1. The c(2x2) Oxygen Overlayer.

The c(2x2)O on Ni(001) system is a very interesting case because studies using different techniques have produced three conflicting results for d_{\perp} , the spacing between the oxygen layer and the topmost nickel layer. The controversy over the surface structure of this system motivated us to study it with NPD.

In Fig. 3 we show the experimental NPD curve of the O(1s) level for the c(2x2)O overlayer on Ni(001) with the geometry shown in the inset. The curve was taken with the sample at room temperature, and was reproducible with an increased peak/valley ratio after cooling the sample to 120K. Peaks in the O(1s) intensity lie at the following kinetic energies (with respect to the vacuum level): 37, 66, 99, 155, and 193 eV.

Due to the possibility of the near coplanar adsorption site for O on Ni(001), Kang and Tong developed a method which allows calculation of emission and diffraction processes in layers having any d_{\perp} spacing, including the coplanar geometry. The method is based on the combined space formulation¹¹ and its details are presented elsewhere.¹² NPD curves for d_{\perp} values from 0.0 to 0.4 Å were calculated in steps of 0.05 Å and from 0.5 to 1.2 Å in steps of 0.1 Å. Five phase shifts are used in the calculation. The inner potential used was 11.2 eV. The comparisons between calculated curves and measured data are shown in Figs. 3 and 4. Starting with the best agreement near 0.9 Å, the agreement worsens as d_{\perp} is decreased. At $d_{\perp} = 0.5$ Å, all five experimental peaks are in disagreement with theory. Poor agreement exists over the range $d_{\perp} = 0.2$ to 0.6 Å. As d_{\perp} is further decreased, agree-

ment improves somewhat in the low energy range. However, even at $d_1 = 0.0 \text{ \AA}$, the agreement is poor above 80 eV. Thus, from visual analysis the best theory-experiment fit is in the region of 0.8-0.9 \AA .

In order to verify this result, we carried out an R-factor analysis, the results of which are shown in Fig. 5. We use a normalized R factor (R_N) based on putting weights on six individual R factors defined by Van Hove, Zanazzi and Jona, and Pendry, and discussed elsewhere.^{13,14} The R factors R_1, \dots, R_6 and R_N are defined as:

$$R_1 = A_1 \times \frac{\text{energy range with slopes of opposite signs}}{\text{total energy range}} \quad (1)$$

$$R_2 = A_2 \times \int (I_e - cI_t)^2 dE, \quad (2)$$

$$R_3 = A_3 \times \int (I_e' - cI_t')^2 dE, \quad (3)$$

$$R_4 = A_4 \times \int (I_e'' - cI_t'')^2 dE, \quad (4)$$

$$R_5 = A_5 \times \int \frac{|I_e' - cI_t'| \times |I_e'' - cI_t''|}{|I_e| + \max |I_e|} dE, \quad (5)$$

$$R_6 = A_6 \times \frac{\int (Y_e - Y_t)^2 dE}{\int (Y_e^2 + Y_t^2) dE} \quad (6)$$

$$R_N = \frac{1}{6} (R_1 + R_2 + R_3 + R_4 + R_5 + R_6) \quad (7)$$

Here, I_e are the experimental intensity data, and I_e' and I_e'' refer to the first and second derivatives of I_e with respect to energy. I_t , I_t' and I_t'' are the corresponding quantities for the calculated intensities.

Also,

$$c = \frac{\int I_e dE}{\int I_t dE}, \quad (8)$$

$$y_{e,t} = \frac{I'_{e,t}/I_{e,t}}{1 + v_I^2 \left(\frac{I'_{e,t}}{I_{e,t}} \right)^2}, \quad (9)$$

$$v_I = 3.8 \cdot \left(\frac{E + V_0}{90 + V_0} \right)^{1/3}, \quad (10)$$

where V_0 is the inner potential and E is the electron energy, in electron volts, above the vacuum level. The weights A_1, \dots, A_6 are chosen such that the average value of each R factor over the geometries considered in this work is the same. This ensures that the influence of each R factor is roughly the same, and in taking the overall average, no one R factor dominates the others. In other works^{13,14} the average of each R factor over all geometries considered has been set to unity. In this work, in order to give R_N a quantitative meaning, we set each average equal to the average of the Zanazzi-Jona R factor over all geometries tried ($d_{\perp} = 0.0$ through 1.2 \AA).¹⁵ The Zanazzi-Jona R factor is the same as our R_5 , except for a different scaling coefficient A_5 . Since the Zanazzi-Jona R factor is widely used, the R_N obtained here can be directly compared to the values of the Zanazzi-Jona R factor found in other works. The R_N has the advantage of including all the additional features contained in the other five R factors (R_1, R_2, R_3, R_4, R_6).

In the R-factor plot (Fig. 5), we note a deep minimum between 0.8 Å and 0.9 Å, in agreement with the previous discussion based on visual analysis. The minimum of the R factor curve occurs at 0.85 Å. The value of R_N is a maximum at $d_{\perp} = 0.5$ Å. As d_{\perp} is further decreased, the value of R_N becomes smaller. However, at $d_{\perp} = 0.0$ Å the value of R_N is larger than 0.2, a value presently considered as the upper bound for a good fit between theory and experiment. In the full range of spacings, $R_N \leq 0.2$ only in the region $d_{\perp} = 0.78$ Å - 0.9 Å. We also varied the inner potential in steps of 1 eV between 8.2 eV and 13.2 eV and found no improvement on the values of the R factor. We conclude from the R factor analysis that $d_{\perp} = 0.85$ Å.

In order to estimate the accuracy of the d_{\perp} value determined by NPD, one must contend with uncertainties in both experiment and theory. The rms peak energy reproducibility in the experimental data is estimated to be ± 1.0 eV. The theoretical accuracy in peak energy position is more difficult to determine because of the use of the inner potential (V_0) as a parameter in the calculation. The inner potential is roughly the average potential felt by an excited electron leaving the solid, so that a change in V_0 produces a corresponding shift in the kinetic energy scale of an NPD theoretical curve. For this reason, the uncertainty in the theoretical data must be estimated by observing the shift in the energy difference between two peaks (ΔE) as a function of d_{\perp} , rather than the shift in absolute position of a single peak. The rms shift in ΔE is estimated to be 40 eV/Å for these data, and the experimental uncertainty in this quantity is ± 1.5 eV. This yields a value of ± 0.04 Å for the accuracy of the determination of

$d_{\perp} = 0.85 \text{ \AA}$ by NPD for the system $c(2 \times 2)0(1s)\text{-Ni}(001)$. With further improvements, an accuracy of $\pm 0.01 \text{ \AA}$ should be possible.

The $c(2 \times 2)0\text{-Ni}(001)$ system has been the object of numerous studies with other techniques. Early LEED I-V studies, based on the data of Demuth and Rhodin,¹⁶ gave evidence for three different structures. Andersson, et al.¹⁷ and Demuth, et al.,¹⁸ found the oxygen to sit above the fourfold hollow site with d_{\perp} values of 1.5 \AA and 0.9 \AA , respectively. Duke, et al.,¹⁹ concluded that the oxygen atoms form a reconstructed Ni-O square lattice which sits on the Ni(001) surface. In the past few years the structure predicted by Demuth, Jepsen and Marcus has become generally accepted; i.e., the $c(2 \times 2)$ overlayer of oxygen atoms is believed to occupy the fourfold hollow site at $d_{\perp} = 0.9 \text{ \AA}$.^{20,21} Rapid LEED intensity measurements by Hanke et al., have confirmed this structure.²² Until recently, however, LEED analysis was not carried out for distances below 0.9 \AA . Tong and Lau¹³ extended the analysis to $d_{\perp} = 0.0 \text{ \AA}$, and found some similarity between the 0.9 \AA and 0.0 \AA theoretical curves, but they concluded that 0.9 \AA still produced the best fit. Brongersma, et al.,²³ used ion scattering spectroscopy (ISS) to determine that oxygen sits in the fourfold hollow site, 0.9 \AA above the surface. Stohr et al.,²⁴ have studied both the $p(2 \times 2)$ and $c(2 \times 2)$ oxygen overlayers on Ni(001) with SEXAFS and found that the oxygen is situated $0.86 \pm 0.07 \text{ \AA}$ above the hollow site in both cases. Thus, the results of LEED, ISS, SEXAFS, and NPD (this work) indicate that the oxygen is well above ($0.85\text{--}0.90 \text{ \AA}$) the surface at the $c(2 \times 2)$ coverage.

Other techniques provide conflicting results, however. Azimuthal photoelectron diffraction (APD) studies by Petersson et al.²⁵ found that for a 15 L exposure of oxygen, which yielded a $c(2 \times 2)$ LEED pattern, the oxygen was nearly coplanar ($d_{\perp} = 0.1 \text{ \AA}$) with the nickel surface. Their data indicate that the oxygen sits $0.8\text{--}0.9 \text{ \AA}$ above the surface at low coverages (exposures less than 1 L) and then moves down into the nickel plane ($d_{\perp} = 0.1 \text{ \AA}$) as the exposure is increased to 15 L, at which point they noted a $c(2 \times 2)$ LEED pattern.

A second conflicting result has been found with high-resolution electron energy loss spectroscopy. A large shift in the oxygen-metal stretching frequency from 430 cm^{-1} for $p(2 \times 2)$ to 310 cm^{-1} for $c(2 \times 2)$ has been observed independently by Andersson²⁶ and Lehwald and Ibach.²⁷ No such shift was observed between $p(2 \times 2)$ and $c(2 \times 2)$ S on Ni(001), leading to speculation that both the electronic state and the binding geometry of the oxygen may have changed significantly. Generalized valence-bond calculations by Upton and Goddard²⁸ concluded that oxygen can adsorb on Ni(001) in two different states with equilibrium d_{\perp} distances of 0.88 \AA and 0.26 \AA . They concluded that the $d_{\perp} = 0.88 \text{ \AA}$ and the $d_{\perp} = 0.26 \text{ \AA}$ states are the dominant species at $p(2 \times 2)$ and $c(2 \times 2)$ coverages, respectively. Using Upton and Goddard's force constants, Rahman, Black, and Mills^{29,30} were able to calculate $p(2 \times 2)$ and $c(2 \times 2)$ EELS spectra which agree remarkably well with the experimental data. Both of these groups argued that the $c(2 \times 2)$ overlayer is situated 0.26 \AA above the nickel surface.

The wide variety of results obtained for the structure of $c(2 \times 2)$ 0 on Ni(001) is not surprising if one considers the different exposures

and conditions which have been used to produce the $c(2 \times 2)$ overlayers. In our experiment, the $c(2 \times 2)$ LEED pattern became sharp at 20 L exposure. The $c(2 \times 2)$ pattern has been shown to persist over the range of exposures up to 125 L, but there is evidence of significant NiO island formation at this coverage.^{10,31} Consequently, the interaction of the Ni(001) surface with oxygen changes from chemisorption to oxidation while the $c(2 \times 2)$ structure is present, at which point the oxygen has moved into the plane. The APD data²⁵ indicate that the oxygen moves down after a 15 L exposure even before the last evidence of a $p(2 \times 2)$ pattern is gone. However, the APD technique is much more sensitive to atomically adsorbed oxygen in or below the surface than to oxygen lying well above the surface. This is because there is a low probability at XPS energies for scattering at angles more than a few degrees from the forward direction.³² Thus, even though a $c(2 \times 2)$ overlayer may be predominant, a small amount of oxygen present in the surface plane could strongly affect the angular dependence of the angle-resolved XPS cross section and resultant surface structure determination. Clearly, the possibility of multiple chemisorption sites cannot be ruled out for a $c(2 \times 2)0$ coverage, especially at higher exposures (>40 L), where a transition from above plane to coplanar oxygen atoms occurs. Our NPD data, however, indicate for a 20 L exposure resulting in a sharp $c(2 \times 2)$ LEED pattern, most of the oxygen lies 0.85 \AA above the fourfold hollows.

The calculations of Upton and Goddard have been brought into question by the recent work of Bauschlicher et al.³³ They found that the inclusion of 4p functions and correlation in Upton and Goddard's

calculation will cause the $d_{\perp} = 0.88 \text{ \AA}$ state to be the lowest energy state for the $c(2 \times 2)$ overlayer. They concluded that the $d_{\perp} = 0.26 \text{ \AA}$ state does not exist on the surface at $c(2 \times 2)$ coverages, but they could not convincingly explain the large observed frequency shift in EELS. One possible explanation is that the $c(2 \times 2)$ overlayers in the experimental studies^{26,27} have undergone some oxide nucleation.³⁴ The possibility that a large frequency shift might be due to increasing the oxygen coverage without a change in d_{\perp} must also be explored theoretically. This possibility was discussed in Chapter III with respect to the O-Cu(001) system.

We conclude this subsection with the following observations. First, the NPD result for $c(2 \times 2)$ -O-Ni(001) is adsorption at $d_{\perp} = 0.85 \pm 0.04 \text{ \AA}$ above the fourfold hollow site. A perspective view of this structure is shown in Fig. 6. Our results agree with those of LEED, ISS, and SEXAFS. A small fraction of oxygen atoms at $d_{\perp} = 0.1 \text{ \AA}$ might go unnoticed in the NPD data but be dominant in APD. The interpretation of the EELS data has been controversial, placing the determination of $d_{\perp} = 0.26 \text{ \AA}$ in doubt. Finally, the existence of conflicting results may be partially due to the wide variety of sample preparation techniques used to obtain the $c(2 \times 2)$ oxygen overlayer.

2. The $c(2 \times 2)$ Sulfur Overlayer.

The second system which we will consider in this chapter is the $c(2 \times 2)$ sulfur overlayer on Ni(001). An NPD curve for this system, extending up to 100 eV above the S(2p) edge, has already been published.¹ Here we present a more extensive NPD curve (up to 200 eV kinetic energy) as well as calculations for the three symmetric adsorption sites. Since

the sulfur atom has a larger atomic radius than oxygen, it is believed to reside completely above the Ni(001) surface in the submonolayer regime. The experimental NPD curve is shown in Fig. 7, for the geometry shown in the inset. The measurements were made after cooling the $c(2 \times 2)S-Ni(001)$ sample (prepared at 300 K) to 120 K. Just as in the case of the oxygen overlayer, the NPD curve taken after cooling to 120 K had an increased peak/valley ratio, but essentially the same peak energies and relative intensities. The theoretical calculations shown are for the fourfold hollow site ($d_{\perp} = 1.30 \text{ \AA}$), the twofold bridge site ($d_{\perp} = 1.80 \text{ \AA}$) and atop site ($d_{\perp} = 2.19 \text{ \AA}$). As was the case in oxygen, the best agreement between theory and experiment is found to be the fourfold hollow site ($d_{\perp} = 1.30 \text{ \AA}$) on the (001) surface. A perspective drawing of this structure is given in Fig. 8. Using the method described in the previous subsection, the accuracy of the d_{\perp} value determined for the sulfur is $\pm 0.04 \text{ \AA}$, the same as in the oxygen case. The agreement is quite poor for the other two sites. Four of the peaks calculated for the fourfold hollow site match experimental peaks to within 1 eV. The only disagreement is in the low kinetic energy region, where the experimental peak at 35 eV does not match the calculated peak at 40 eV. In this region, the calculated peak positions are very sensitive to the choice of the sulfur scattering potential, whereas all other calculated peak positions (57, 82, 129, and 172 eV) are fairly insensitive to that potential. The theory also does not address the predominance of multiple scattering and other effects close to the edge. We note that above 50 eV kinetic energy, all of these complications become more manageable, and the experiment-

theory agreement improves dramatically. The relative intensities of the experimental peaks, as well as their positions, are closely reproduced by the theory.

The $c(2 \times 2)S-Ni(001)$ system has been the subject of several earlier structural studies. An ARP study by Plummer et al.³⁵ on the $S(3p)$ derived level for this system found a peak at $h\nu = 18$ eV. This peak was reproduced by Li and Tong's calculations only if the sulfur atoms were placed in fourfold hollow sites at $d_1 = 1.30$ Å.³⁶ The first LEED intensity analyses concluded that the sulfur is situated above the surface in the fourfold hollow site, although there was disagreement as to whether d_1 was 1.3 Å,^{18,37} (the hard-sphere radius result) or 1.7 Å.¹⁹ As in the case of the corresponding oxygen system discussed above, the hard-sphere radius result²⁰ was eventually agreed upon, and a recent experimental and theoretical study using iso-intensity maps of specular beam data confirmed that structure.³⁸ A photoelectron diffraction study of the $S(1s)$ level in $c(2 \times 2)S-Ni(001)$ carried out by our group led to the conclusion that $d_1 = 1.38 \pm 0.04$ Å for this system, which is within experimental error of our $S(2p)$ NPD results.⁸

D. FOURIER-TRANSFORM ANALYSIS

Our experimental data were compared to calculations in Section III. The calculations utilize a multiple-scattering approach to ultraviolet and soft x-ray photoemission spectroscopy.^{4,12} The initial state is calculated by choosing a cluster of atoms representing the postulated geometry of nickel atoms about the sulfur or oxygen adsorbate and sol-

ving for the cluster wave function using the $X\alpha$ scattered-wave method. The final-state scattering is modeled by using a multiple-scattering T matrix to propagate the photoelectron wave through the first few surface layers. Recently, Li and Tong have developed a simplified scheme, called the quasi-dynamical (QD) method, which produced very accurate intensity versus electron kinetic energy curves for energies greater than 60 eV when compared to the full dynamical calculation.³⁹ The QD calculation takes advantage of the fact that in the high-energy limit, forward scattering is the predominant process. The only scattering events considered besides all forward scatterings are (a) one backscattering from each layer, and (b) one scattering from each atom within a layer. All NPD calculations shown here utilize the full dynamical method, but the quasi-dynamical method gives consistent results. Unfortunately, even the QD approach is quite involved, and comparison with experiment is implicit.

To avoid the complexities of the calculations, we have searched for simpler methods of analyzing NPD data. The kinematical method, which assumes that single scattering is the predominant factor, has been tried without much success on the system $p(2 \times 2)\text{Se-Ni}(001)$. Li and Tong have done a kinematical calculation on that system in the kinetic energy range 150–400 eV and found substantial disagreement with their dynamical calculations over that energy range.³⁹

Another method which we have considered is the use of the Fourier transform (FT) to isolate the single scattering effects. The Fourier transform has been used with great success in interpreting extended x-ray absorption fine structure (EXAFS) data.⁴⁰ In EXAFS, the final-

state electron scattering intensity is isolated from the atomic-like initial state background by determining the function $\chi(k) = (I - I_0)/I_0$, where I is the total absorption and I_0 is a smooth atomic background. If the phase shift of the scattering atoms is independent of energy, then the FT has been shown to yield interatomic distances rigorously for s initial states, and approximately for other states under certain conditions.⁴⁰ Since EXAFS is an angle-integrated technique, it yields the nearest-neighbor distances from the central excited atom. By analogy, one might expect intuitively that an FT of NPD data would be sensitive to the one-dimensional structure normal to the crystal face, as NPD is an angle-resolved technique.⁴¹ In fact, our group has applied FT analysis to NPD curves calculated by Li and Tong for the $(\sqrt{3} \times \sqrt{3}) R30^\circ$ Se-Ni(111) system, with much success.⁴²

An analytical formula has been derived by Tong and Tang⁷ which indicates that multiple perpendicular distances from the overlayer to substrate layers can be extracted by Fourier transformation of experimental NPD data (see Chapter I, Section B). They derived the normalized modulation function

$$\chi(k) = \frac{I_{\text{NPD}} - I_0}{I_0} \approx 2 \sum_{\alpha=1}^N R_{\alpha} \cos \left\{ 2k[d_{\perp} + (\alpha-1)b] + \phi_{\alpha} + \phi^{+} + \phi^{-} \right\} \quad (11)$$

which is a sum of cosine functions, so that a Fourier transformation of $\chi(k)$ gives peaks related to the distances $2[d_{\perp} + (\alpha-1)b]$.

One of the criteria for a successful Fourier transform is the need for an extended k -space data set. Typical EXAFS spectra extend from about 50 eV to a few hundred eV above the absorption edge. If the

range of k -space data is too small, the FT may not be able to pick up a sufficient number of oscillations to yield accurate structural information. In particular, if the experimental data do not extend far enough above the edge, the smallest distance peaks in the Fourier transformed data may not be resolved.

With this limitation in mind, we nevertheless carried out fast Fourier transforms⁴³ of the function $\chi(k) = (I - I_0)/I_0$ for these NPD curves. The range of data used for both the $O(1s)$ in $c(2 \times 2)O-Ni(001)$ and the $S(2p)$ in $c(2 \times 2)S-Ni(001)$ cases was $50 \text{ eV} < E_{kin} < 200 \text{ eV}$, or roughly $4 \text{ \AA}^{-1} < k < 7.5 \text{ \AA}^{-1}$. Since the phase shifts in the NPD process have been predicted to be smaller than those in EXAFS,^{8,42} they were omitted for these initial calculations. Care was taken to terminate the data at points where $\chi(k) = 0$. The transform was found to be fairly insensitive to changes in the estimated atomic background I_0 .

In Fig. 9, we show the function $\chi(k)$ for $c(2 \times 2)S(2p)-Ni(001)$. Note that the large modulations in $\chi(k)$ (-0.4 to 0.4) for NPD are an order of magnitude greater than those typical in EXAFS. These large modulations make the analysis much less sensitive to the background subtraction. Due to experimental limitations such as the $1/E_{kin}$ dependence of the analyzer transmission function and especially the performance of the grasshopper monochromator at high photon energies (discussed above), the measurements were only taken up to 200 eV above threshold. In addition, the scattering cross-sections are decreasing functions of energy above 200 eV, resulting in a substantial reduction in the size of the modulations. The magnitude of the FT is shown in Fig. 10. There are two major peaks, showing maxima at 6.04 and 9.66 Å. NPD and LEED

analyses yield $d_1 = 1.30 \text{ \AA}$, and the interlayer spacing for Ni(001) is $b = 1.76 \text{ \AA}$. These two peaks are therefore attributed to the distances $2(d_1 + b) = 6.12 \text{ \AA}$ and $2(d_1 + 2b) = 9.64 \text{ \AA}$. There is no peak in the real-space distribution function for $2(d_1) = 2.60 \text{ \AA}$. The agreement for the two main peaks is very good considering the limited data range.

The FT technique was also applied to the NPD curve for $c(2 \times 2)0(1s)\text{-Ni}(001)$. The function $X(k)$ is shown in Fig. 11, and the corresponding transform in Fig. 12. For this system, the average of d_1 given by NPD and LEED is 0.88 \AA from which $2(d_1 + b) = 5.28 \text{ \AA}$, and $2(d_1 + 2b) = 8.80 \text{ \AA}$. Again, we find that the two main peaks in the transformed data, at 5.40 and 8.66 \AA , match up fairly closely with these previously determined values of $2(d_1 + b)$ and $2(d_1 + 2b)$.

These two examples support the idea that Fourier transformation of NPD data yields structural information directly. More recent work by other members of the Shirley group on the double crystal monochromator beam line at SSRL has advanced the state of Fourier transform photoelectron diffraction (FTPD) considerably.⁸ Their major experimental advance has been to take PD data with excellent statistics over a much wider kinetic energy range (400 eV). In addition, they have developed a new theory of FTPD which predicts that Fourier transforms of experimental PD data taken at well-chosen angles with respect to the crystalline axes will yield the distances from the adsorbate atom to a number of selected substrate atoms. This single scattering approach predicts that electrons are scattered by atomic centers, not layers, as predicted by Tong and Tang.

The new single scattering approach to PD has two major ramifications for NPD. First, the strong dominance of forward scattering and 180° scattering above 100 eV should ensure that only those substrate atoms directly or nearly below the adsorbate atom will contribute to the NPD oscillations. This explains why we do not observe a $2(d_1)$ peak in the FT of our S-Ni(001) and O-Ni(001) data. For adsorbate photoelectrons to scatter off the first layer (nearest neighbor) nickel atoms into the detector, they must undergo a scattering of 126° and 115° for S and O on Ni(001), respectively. The second layer peak, on the other hand, is large because a substrate atom is situated directly below the adsorbate (emitter). The third layer peak will not be seen as strongly because it requires scattering of 160° for S and 158° for O. These angles are close enough to 180° to provide a reasonable probability of backscattering, however.

The second ramification of the single scattering approach is that NPD measures the path length difference between the direct wave from the adsorbate to the detector and the wave which backscatters off a substrate atom, rather than twice the perpendicular distance between adsorbate and substrate layers. This concept of atom scattering is radically different than layer scattering, but does not have a large effect on the appearance of the data. This is because most backscattering occurs near 180° , so that at normal emission, interplanar distances are numerically close to path length differences. For example, the second layer atom directly below the hollow site will give an FT peak at the same distance in both theoretical approaches. The third layer has four atoms around the hollow which have slightly longer dis-

tances in the single scattering approach (9.95 Å for S, 9.08 Å for O) than in the interplanar approach (9.64 Å for S; 8.74 Å for O). The discrepancy between the experimental FT peaks (9.66 Å for S, 8.80 Å for O) and those predicted by theory is larger for the single scattering approach, but the agreement is still adequate. The discrepancy might be resolved by the inclusion of backscattering phase shifts and/or other scattering paths in the FT.

E. CONCLUSIONS

The normal emission photoelectron diffraction technique was used to determine that the c(2x2)O and c(2x2)S overlayers on Ni(001) sit above the fourfold hollow site in the surface with d_{\perp} spacings of 0.85 ± 0.04 Å and 1.30 ± 0.04 Å, respectively. These distances agree with LEED results. More work on the oxygen-nickel system as a function of coverage is needed to more fully understand the transition from chemisorbed oxygen to bulk nickel oxide. The similarity between NPD and EXAFS has been further confirmed by the successful application of the Fourier transform technique to experimental NPD data, and by the discovery of a theoretical framework to explain why these transforms are successful.

REFERENCES

- * Part of this chapter was published: D. H. Rosenblatt, J. G. Tobin, M. G. Mason, R. F. Davis, S. D. Kevan, D. A. Shirley, C. H. Li, and S. Y. Tong, in *Phys. Rev. B* 23, 3828 (1981).
Another part will be submitted to *Phys. Rev. B* for publication.
1. S. D. Kevan, D. H. Rosenblatt, D. Denley, B.-C. Lu, and D. A. Shirley, *Phys. Rev. Lett.* 41, 1565 (1978); *Phys. Rev. B* 20, 4133 (1979).
 2. G. P. Williams, F. Cerrina, I. T. McGovern, and G. J. Lapeyre, *Solid State Commun.* 31, 15 (1979).
 3. S. D. Kevan, R. F. Davis, D. H. Rosenblatt, J. G. Tobin, M. G. Mason, D. A. Shirley, C. H. Li, and S. Y. Tong, *Phys. Rev. Lett.* 46, 1629 (1981).
 4. C. H. Li, A. R. Lubinsky, and S. Y. Tong, *Phys. Rev. B* 17, 3128 (1978).
 5. S. D. Kevan, J. G. Tobin, D. H. Rosenblatt, R. F. Davis, and D. A. Shirley, *Phys. Rev. B* 23, 493 (1981).
 6. C. H. Li and S. Y. Tong, *Phys. Rev. Lett.* 42, 901 (1979).
 7. S. Y. Tong and J. C. Tang, *Phys. Rev. B* 25, 6526 (1982).
 8. J. J. Barton, C. C. Bahr, Z. Hussain, S. W. Robey, J. G. Tobin, L. E. Klebanoff, and D. A. Shirley, 1982, unpublished.
 9. S. D. Kevan, Ph.D. thesis, University of California, Berkeley, 1980, unpublished; S. D. Kevan and D. A. Shirley, *Phys. Rev. B* 22, 542 (1980).
 10. T. Fleisch, N. Winograd, and W. N. Delgass, *Surf. Sci.* 78, 141 (1978).

11. S. Y. Tong and M. A. Van Hove, Phys. Rev. B 16, 1459 (1977).
12. W. M. Kang, Ph.D. thesis, University of Wisconsin-Milwaukee, 1982, unpublished.
13. S. Y. Tong and K. H. Lau, Phys. Rev. B 25, 7382 (1982).
14. D. H. Rosenblatt, S. D. Kevan, J. G. Tobin, R. F. Davis, M. G. Mason, D. A. Shirley, J. C. Tang, and S. Y. Tong, Phys. Rev. B 26, 3181 (1982).
15. E. Zanazzi and F. Jona, Surf. Sci. 62, 61 (1977).
16. J. E. Demuth and T. N. Rhodin, Surf. Sci. 45, 249 (1974).
17. S. Andersson, B. Kasemo, J. B. Pendry, and M. A. Van Hove, Phys. Rev. Lett. 31, 595 (1973).
18. J. E. Demuth, D. W. Jepsen, and P. M. Marcus, Phys. Rev. Lett. 31, 540 (1973).
19. C. B. Duke, N. O. Lipari, and G. E. Laramore, Nuovo Cimento 23B, 241 (1974).
20. P. M. Marcus, J. E. Demuth, and D. W. Jepsen, Surf. Sci. 53, 501 (1975).
21. M. Van Hove and S. Y. Tong, J. Vac. Sci. Technol. 12, 230 (1975).
22. G. Hanke, E. Lang, K. Heinz, and K. Muller, Surf. Sci. 91, 551 (1975).
23. H. H. Brongersma and J. B. Theeten, Surf. Sci. 54, 519 (1976).
24. J. Stohr, R. Jaeger, and T. Kendelewicz, Phys. Rev. Lett. 49, 142 (1982).
25. L. G. Petersson, S. Kono, N. F. T. Hall, S. Goldberg, J. T. Lloyd, C. S. Fadley, and J. B. Pendry, Matl. Sci. and Engr. 42, 111 (1980).

26. S. Andersson, *Surf. Sci.* 79, 385 (1979).
27. S. Lehwald and H. Ibach, in Vibrations at Surfaces, ed. R. Caudano, J. M. Gilles, and A. A. Lucas (Plenum, New York, 1982), p. 137.
28. T. H. Upton and W. A. Goddard, III, *Phys. Rev. Lett.* 46, 1635 (1981).
29. T. S. Rahman, J. E. Black, and D. L. Mills, *Phys. Rev. Lett.* 46, 1469 (1981).
30. T. S. Rahman, J. E. Black, and D. L. Mills, *Phys. Rev. B* 25, 883 (1982).
31. P. H. Holloway and J. B. Hudson, *Surf. Sci.* 43, 123 (1974).
32. S. Kono, S. M. Goldberg, N. F. T. Hall, and C. S. Fadley, *Phys. Rev. B* 22, 6085 (1980).
33. C. W. Bauschlicher, Jr., S. P. Walsh, P. S. Bagus and C. R. Brundle, unpublished.
34. C. R. Brundle and H. H. Hopster, *J. Vac. Sci. Technol.* 18, 663 (1981).
35. E. W. Plummer, B. Tonner, N. Holzwarth, and A. Liebsch, *Phys. Rev. B* 21, 4306 (1980).
36. C. H. Li and S. Y. Tong, *Phys. Rev. Lett.* 40, 46 (1978).
37. J. E. Demuth, D. W. Jepsen, and P. M. Marcus, *Phys. Rev. Lett.* 32, 1182 (1974).
38. Y. Gauthier, D. Aberdam, and R. Baudoing, *Surf. Sci.* 78, 339 (1978).
39. C. H. Li and S. Y. Tong, *Phys. Rev. Lett.* 43, 526 (1979).

40. E. A. Stern, D. E. Sayers, and F. W. Lytle, Phys. Rev. B 11, 4836 (1975).
41. A. Liebsch, Phys. Rev. B 13, 544 (1976).
42. Z. Hussain, D. A. Shirley, C. H. Li, and S. Y. Tong, Proc. Natl. Acad. Sci. USA 78, 5293 (1981).
43. G. D. Bergland, IEEE Spectrum 6, 41 (1969).

FIGURE CAPTIONS

- Figure 1. Real space structures and LEED patterns for clean Ni(001) and the three ordered O-Ni(001) overlayers.
- Figure 2. Observed O-Ni(001) LEED patterns as a function of O₂ exposure. Upper panel indicates a possible three stage mechanism for oxidation of Ni(001).
- Figure 3. Experimental NPD curve for O(1s) electrons from c(2x2)O-Ni(001), for the geometry shown, compared with theoretical curves for d_⊥ = 0.5 Å to 1.2 Å (hollow site).
- Figure 4. Experimental NPD curve for c(2x2)O(1s)-Ni(001), compared with theoretical curves for d_⊥ = 0.00 Å to 0.40 Å (hollow site).
- Figure 5. Plot of normalized R factor (R_N) vs. d_⊥ spacing for c(2x2)O-Ni(001).
- Figure 6. Perspective drawing of the c(2x2)O-Ni(001) structure.
- Figure 7. NPD curve for S(2p) electrons from c(2x2)S-Ni(001), compared with hollow site theoretical curves for d_⊥ = 1.30, 1.80, and 2.19 Å for the experimental geometry shown. The binding energy for S(2p) is 170 eV with respect to the vacuum level. The inner potential in the calculation is 14 eV.
- Figure 8. Perspective drawing of the c(2x2)S-Ni(001) structure.
- Figure 9. Plot of $X(k) = (I - I_0)/I_0$ for S(2p) NPD data from c(2x2)S-Ni(001).
- Figure 10. Magnitude of the Fourier transform of the data in Fig. 9.
- Figure 11. Plot of $X(k) = (I - I_0)/I_0$ for O(1s) NPD data from c(2x2)O-Ni(001).
- Figure 12. Magnitude of the Fourier transform of the data in Fig. 11.

O-Ni (001) STRUCTURES

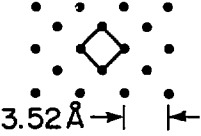
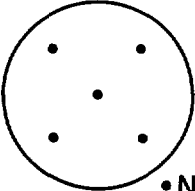

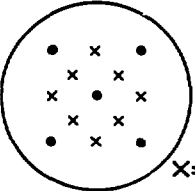

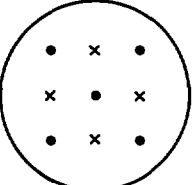
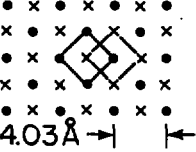
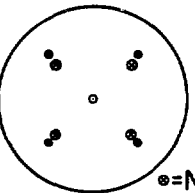
Real Space(top view)	Coverage	Reciprocal Space (LEED pattern)
 <p>3.52 Å → ←</p> <p>• Ni atoms</p>	<p>Clean Ni(001)</p>	 <p>• Ni</p>
 <p>X=O atoms</p>	<p>p(2x2) $\theta = 0.25$</p>	 <p>X=O</p>
 <p>X=O atoms</p>	<p>c(2x2) $\theta = 0.50$</p>	
 <p>4.03 Å → ←</p>	<p>NiO(001) surface $\theta = 1$ 15% expansion</p>	 <p>• NiO</p>

Fig. 1

XBL 8112-12083

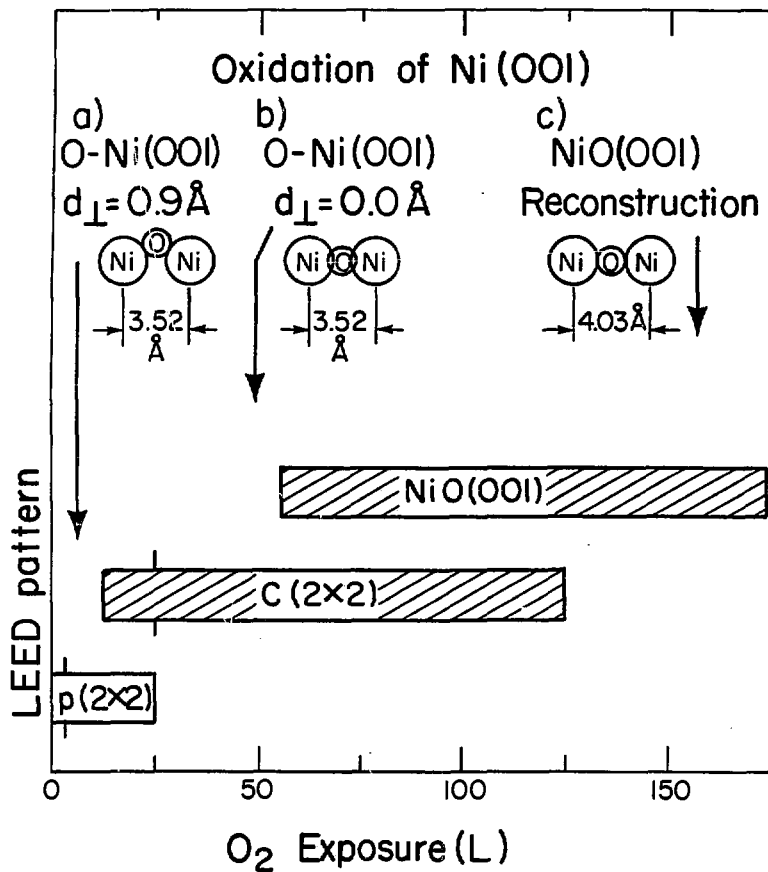


Fig. 2

XBL8112-12084

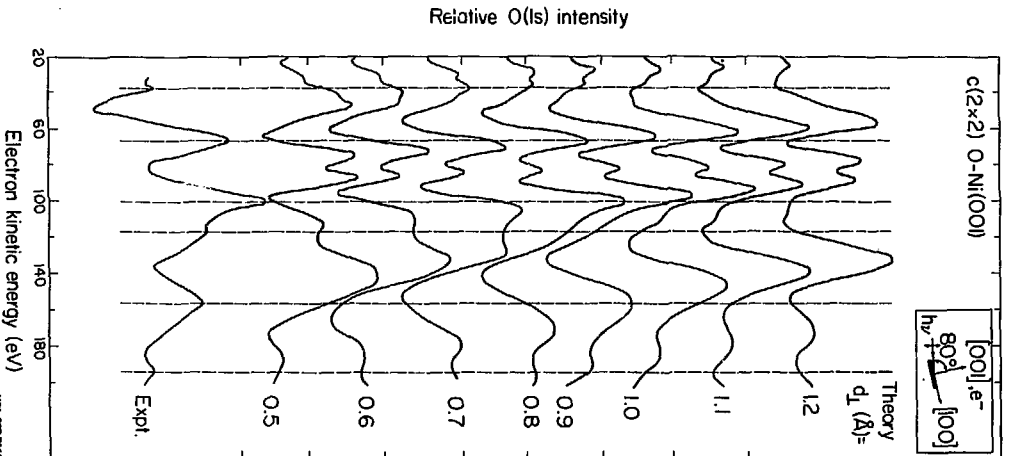


Fig. 3

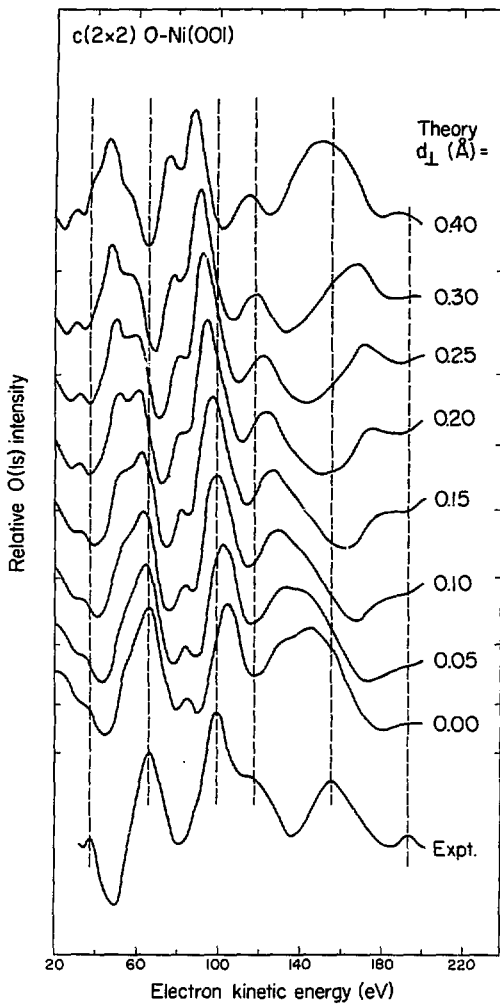
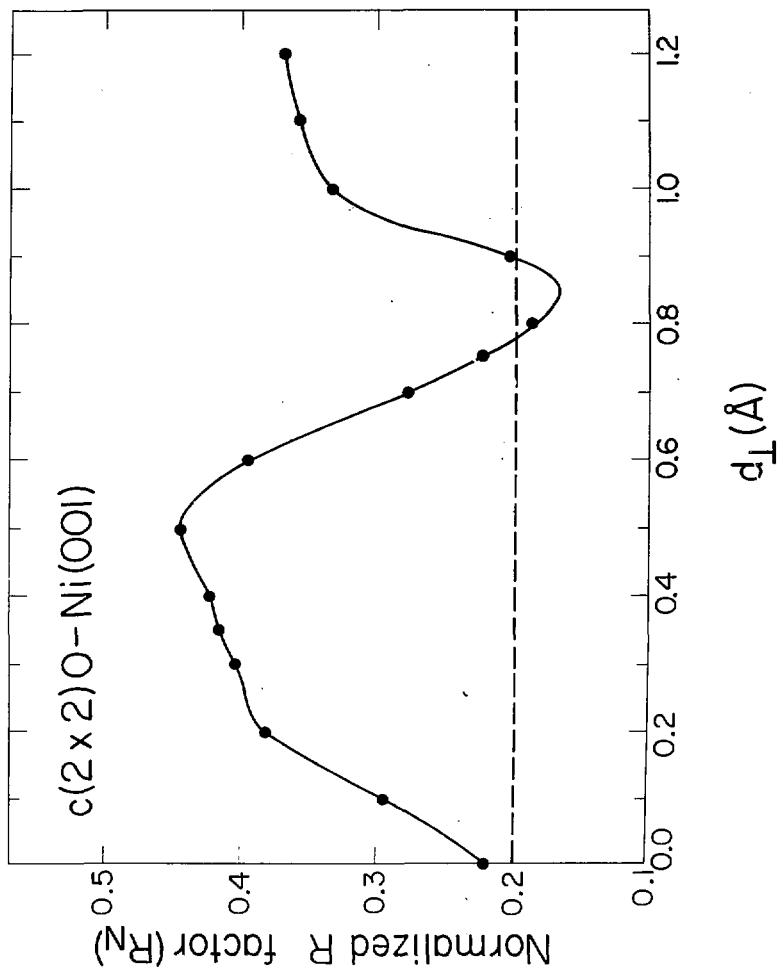
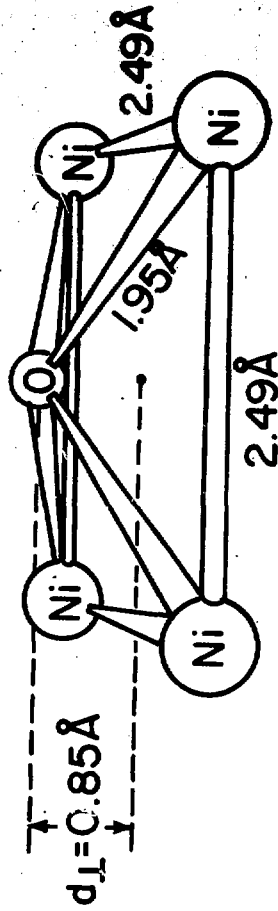


Fig. 4





CBB 821-217

Fig. 6

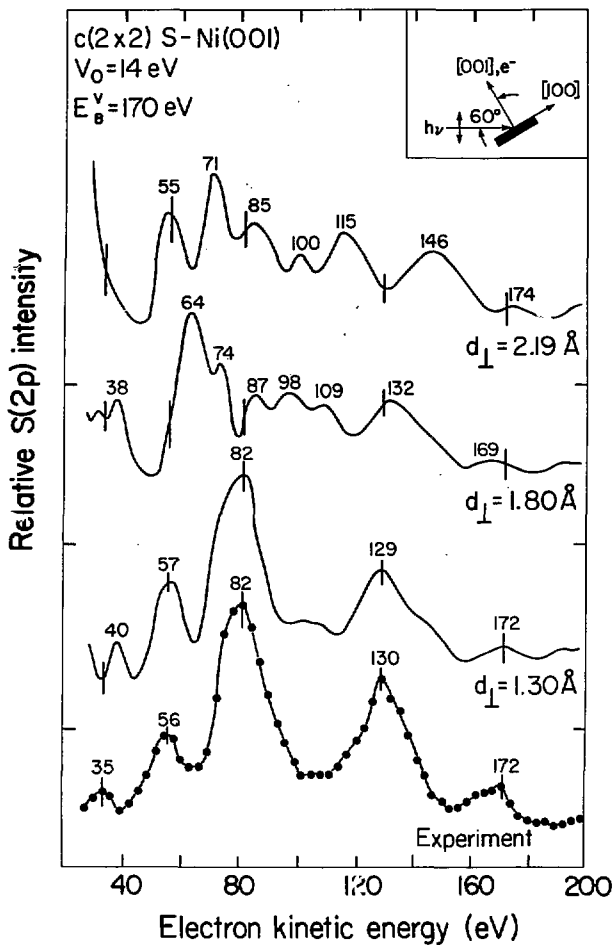
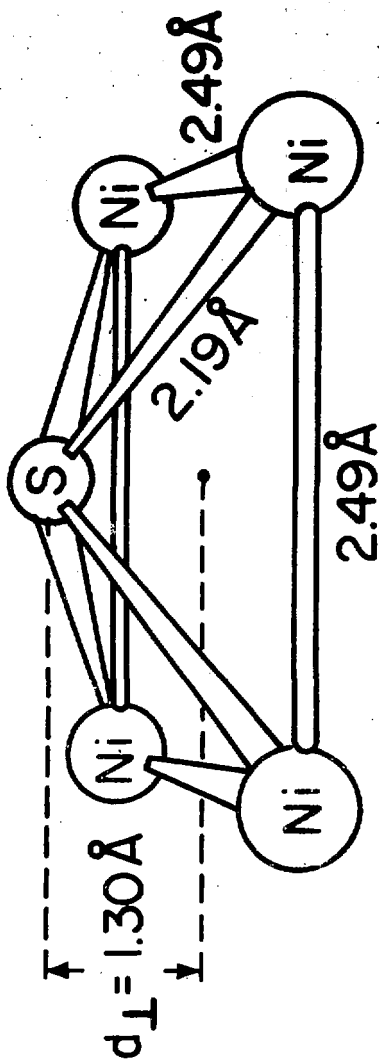


Fig. 7

XBL8010-2113



CBB 821-213

Fig. 8

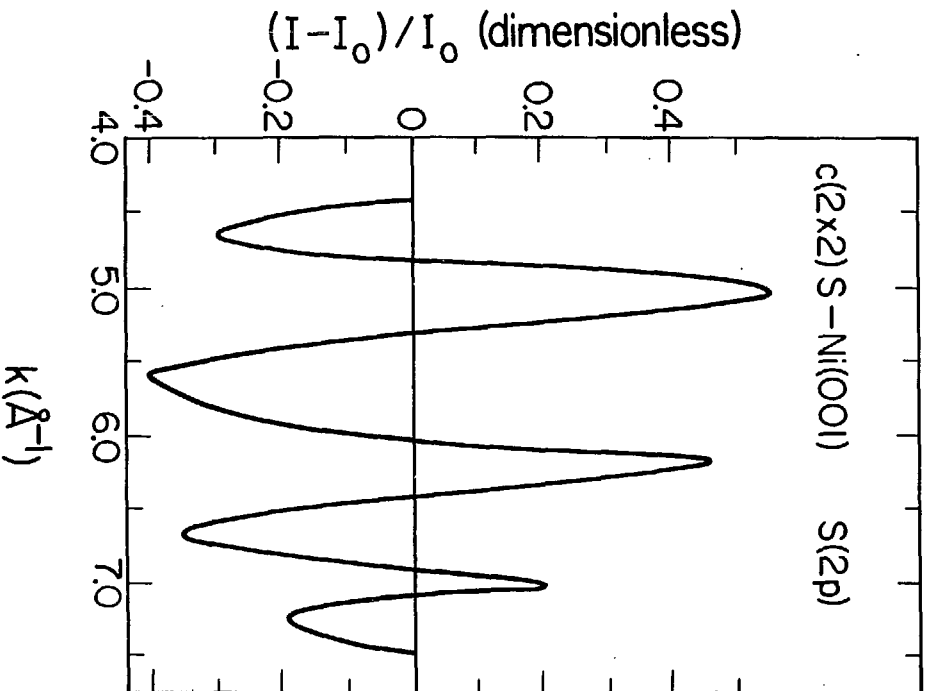


Fig. 9

XBL 8010-2114

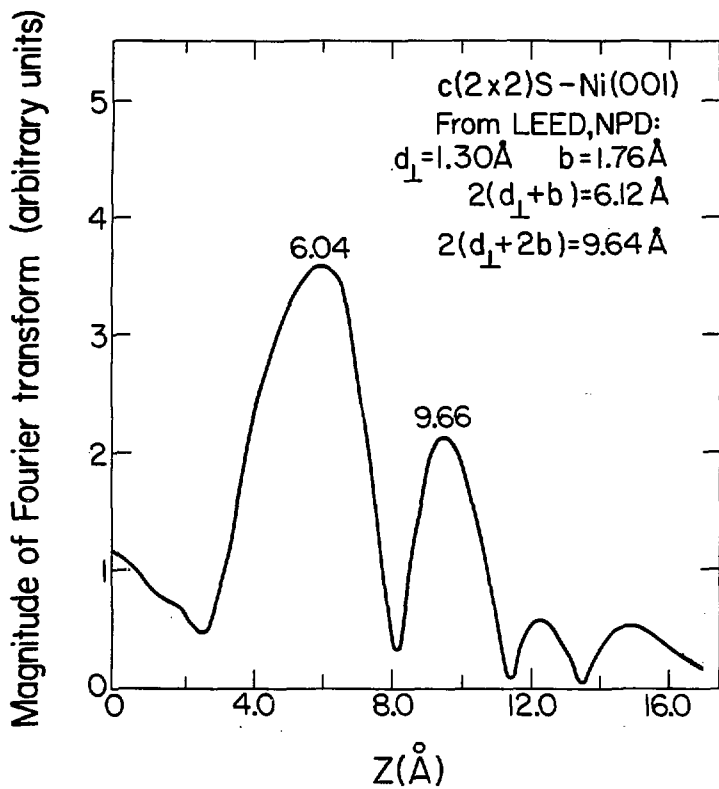


Fig. 10

XBL8010-2116A

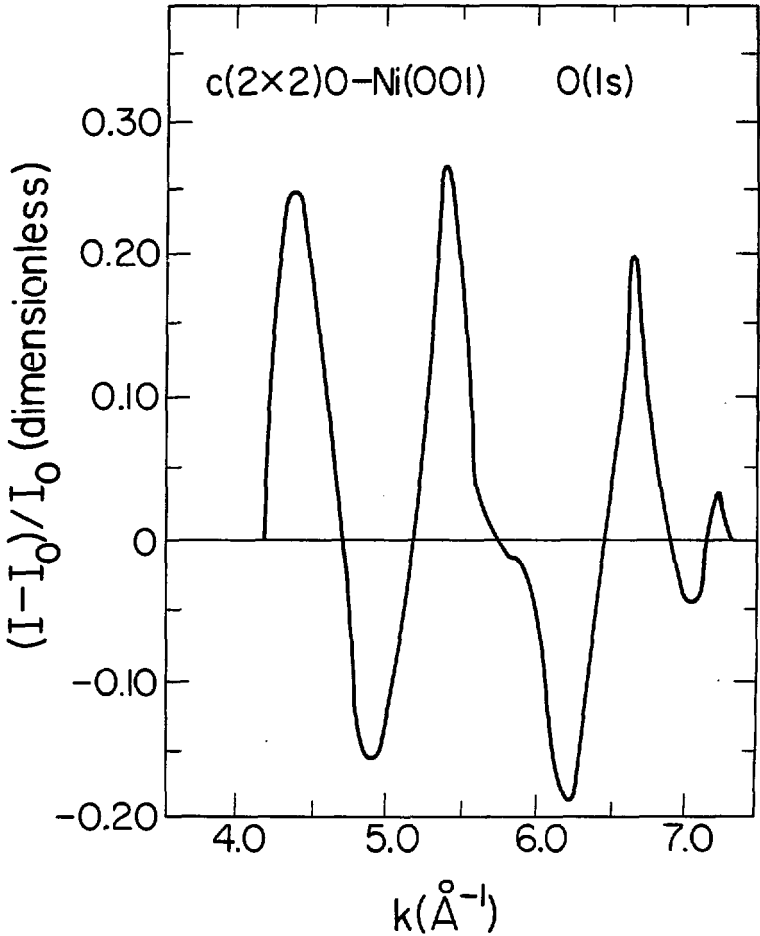


Fig. 11

XBL 8010 - 2115

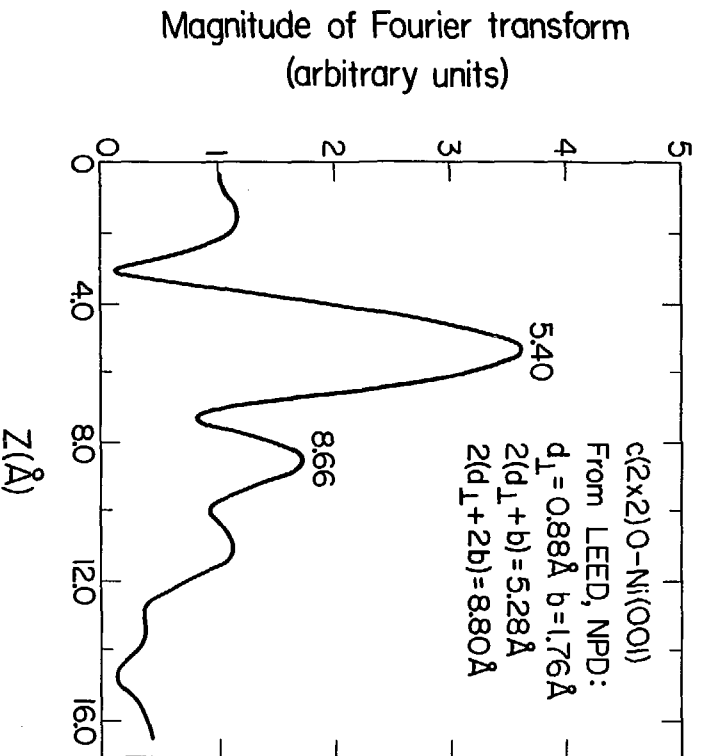


Fig. 12

XBL8010-2117B

V. NORMAL PHOTOELECTRON DIFFRACTION STUDIES OF SELENIUM AND SULFUR OVERLAYERS ON Ni(011) AND Ni(111)*

A. INTRODUCTION

Normal photoelectron diffraction (NPD) is now established as an accurate method of determining the structure of atomic¹⁻³ and molecular⁴ overlayers on single crystal metal surfaces. In an NPD experiment, the photoemission intensity of an adsorbate core level is measured normal to the surface as a function of photoelectron kinetic energy. Final-state diffraction phenomena superimpose modulations on the atomic cross-section of the core level. These modulations contain structural information, which can be obtained implicitly,¹⁻⁶ by comparison of experimental and calculated NPD curves, or explicitly,^{1,7} utilizing the Fourier transformation in a manner similar to its use in extended x-ray absorption fine structure (EXAFS). The structural parameter derived from an NPD experiment is d_{\perp} , the perpendicular spacing between the adsorbate and top substrate layers.

In this chapter we report applications of the NPD technique to two systems which have not been previously studied by any structural technique -- c(2x2)Se on Ni(011) and selenium adsorbed on Ni(111). Four different overlayers of Se on Ni(111) were studied and theoretical analyses are presented below. Two of these overlayers exhibit more complex NPD curves than would be expected from a Se atom in a single adsorption site. Theoretical analysis of one of these cases indicates that the selenium atom is adsorbed in two different sites. For c(2x2)Se on Ni(011), our NPD data clearly suggest adsorption of selenium in the hollow site with $d_{\perp} = 1.10 \text{ \AA}$. We also studied the adsorption of c(2x2)S

on Ni(011). An excellent theory-experiment fit for the hollow site at $d_{\perp} = 0.94 \text{ \AA}$ was obtained, in agreement with the earlier low-energy electron diffraction (LEED) result.⁸ However, our experimental data range is too limited to rule out the top site unambiguously.

Section B contains experimental information. In Section C we briefly describe the multiple scattering calculations used to fit the experimental data. In Section D we present the NPD data and a discussion of the surface structures which are derived, and in Section E a few conclusions about this work are given.

B. EXPERIMENTAL

All data reported here were obtained with an angle-resolved photoemission (ARP) spectrometer described elsewhere.⁹ The spectrometer has LEED and Auger electron spectroscopy capabilities, as well as an adsorbate introduction system which allows for effusive beam dosing. The base pressure of the vacuum chamber was 2×10^{-10} torr during all measurements. The pressure rose to as high as 5×10^{-9} torr during effusive beam dosing. The Ni(011) and Ni(111) crystals were oriented to within 1° of the appropriate crystal faces. Both crystals were cleaned by hot (1025 K) and room temperature cycles of argon-ion sputtering followed by annealing to 875 K, resulting in surfaces essentially free of impurities with sharp (1x1) LEED patterns. The c(2x2)S and Se overlayers on Ni(011) were prepared by exposing the clean Ni(011) crystal to 10-15 L of H₂S and H₂Se, respectively, with the crystal at 300 K.¹⁰ A p(2x2)Se overlayer (taken to be 0.25 monolayer) on Ni(111) with a sharp LEED pattern was obtained by cooling the sample

to 120K, exposing to about 2L of H_2Se and then annealing the sample to 500K.¹⁰ A $p(2 \times 2)$ LEED pattern was also obtained by exposing Ni(111) to H_2Se with the sample at 120K and not allowing it to warm up.¹¹ The quality of the latter LEED pattern was poorer, however. A $(\sqrt{3} \times \sqrt{3})R30^\circ$ Se overlayer (0.5 monolayer) was prepared by increasing the exposure to 5 L of H_2Se . The $(\sqrt{3} \times \sqrt{3})R30^\circ$ LEED spots were weak and there was a substantial diffuse background. Finally, a low coverage (0.1 monolayer) overlayer of Se on Ni(111) was produced with a 1 L exposure. This overlayer gave a LEED pattern indicative of a disordered overlayer (only LEED spots due to the substrate were present). The coverage of the latter two overlayers was determined by comparing their Se(3d) photoemission intensity (normalized by Ni(3p) intensity) to that of the $p(2 \times 2)$ overlayer (assumed to be 0.25 monolayer).

The experiments were performed on Beam Line I-1 at the Stanford Synchrotron Radiation Laboratory (SSRL). Low resolution ARP spectra were taken of the Se(3d) and S(2p) levels, which have binding energies of 62 eV and 170 eV below the vacuum level, respectively. Spectra were taken at photon energy intervals of 3 eV. The angle-resolved relative intensities of these levels were computed by calculating the area of the core level peaks (after background subtraction) and adjusting for photon flux and analyzer transmission. The kinetic energy range of the resulting NPD curves was generally 20–200 eV for the Se(3d) studies and was 20–150 eV for the one S(2p) system discussed below. Experimental geometries are indicated in the figures. The Se(3d) and S(2p) data shown below were presented in the doctoral

thesis of S. D. Kevan.⁹ They have been reanalyzed and interpreted in this chapter.

C. THEORY

We used a Green's function multiple scattering method⁵ to calculate the NPD intensity versus energy (IE) spectra. Wavefunctions for Se(3d) and S(2p) were generated from self-consistent $X\alpha$ scattered wave calculations of Ni_5Se and Ni_5S clusters. Inputs to the multiple scattering calculation include Ni phase shifts from the self-consistent potential of Wakoh,¹² and Se or S phase shifts from the same $X\alpha$ scattered-wave calculations that generated the initial state wavefunctions. The inner potentials used were $V_0 = 11.2$ eV for Se and $V_0 = 9.95$ eV for S overlayers.

Calculations were done with the overlayer placed at high symmetry sites, i.e., the top, hollow and bridge sites. At each site, 8 to 12 interlayer spacings (d_1) between the overlayer and the top substrate layer were tried. Calculations were carried out with increments in d_1 of 0.02 Å for S and Se on Ni(011) and 0.05 Å for Se on Ni(111). In Figs. 3 through 7, calculated curves are shown only at selected d_1 values.

D. RESULTS AND DISCUSSION

1. Selenium Overlayers on Ni(111).

In this subsection we present NPD results for four different overlayers of selenium adsorbed on Ni(111). The lowest coverage studied was a disordered overlayer. We also studied the two ordered overlayers for which LEED patterns have been previously observed; i.e.,

the $p(2 \times 2)$ and $(\sqrt{3} \times \sqrt{3})R30^\circ$ structures. The selenium on Ni(111) system is of special interest both because there has been no structural determination by LEED intensity analysis or any other technique to date and because of the possibility that multiple adsorption sites might be present at certain selenium coverages. Structural studies of adsorbates on fcc(111) surfaces are also of interest because of the existence of two types of threefold hollow sites. Half of the threefold hollow sites on a Ni(111) surface layer have substrate atoms directly below them in the second layer, while the other half have vacancies in the second layer. In this section, we show that NPD is sensitive to these two types of threefold hollow sites for selenium adsorbed on Ni(111).

The experimental geometry for all the NPD measurements of the Se-Ni(111) system is shown in Fig. 1. Figure 1(a) shows that the photon vector potential (\vec{A}) and the direction of emission (e^-) lie in the plane defined by the [111] and $[\bar{2}11]$ directions. The orientation of the atoms on the Ni(111) face is shown in Fig. 1(b). The positions of the four possible high symmetry adsorption sites for Se on Ni(111) are shown with respect to the first two layers of substrate atoms in Fig. 1(c). Using hard-sphere radii to determine the expected values of the structural parameter d_\perp , one obtains $d_\perp = 1.85 \text{ \AA}$ for both hollow sites, $d_\perp = 2.00 \text{ \AA}$ for the bridge site, and $d_\perp = 2.30 \text{ \AA}$ for the top site. Because of the close-packed arrangement of atoms on the Ni(111) surface, the d_\perp values for the three sites, as predicted by a hard-sphere model, are much closer to one another than for the Ni(001) and Ni(011) surfaces.

In Fig. 2, all four experimental NPD curves for Se-Ni(111) are plotted. The lowest coverage studied, shown at the bottom, was a disordered selenium overlayer, estimated to be 0.1 monolayer. The second curve from the bottom in Fig. 2 was obtained from a p(2x2) overlayer (0.25 monolayer). Both of these overlayers had been heated to 500 K after the H₂Se exposure and then cooled to 120 K during NPD data acquisition. Because the p(2x2) overlayer was heated (resulting in an improvement of the p(2x2) LEED pattern), we refer to it as the "annealed" p(2x2) overlayer. Just as in a previous study of Se on Ni(001) carried out in our laboratory,¹³ the NPD data for the low coverage and annealed p(2x2) overlayers of Se on Ni(111) are quite similar. Slight differences are seen in the peak at 65 eV kinetic energy, which are possibly the result of the experimental difficulties involved with lower coverages and the presence of a nickel Auger peak in that energy region.

In Fig. 3, the experimental results from the annealed p(2x2)Se-Ni(111) surface are compared to theoretical calculations for the four possible high symmetry adsorption sites. Excellent agreement is found for hollow site 1 (with a vacancy below) and $d_1 = 1.80 \text{ \AA}$. This value is slightly smaller (0.05 \AA) than the d_1 value obtained by using hard-sphere radii derived from the c(2x2)Se-Ni(001) surface.² The only experimental peak which shows a mismatch with theory is the first peak (~50 eV kinetic energy), and previous NPD work has indicated that there are substantial problems with both theory and experiment in this energy region.¹ Fair but definitely inferior agreement is also found for hollow site 2 (atom below) and $d_1 = 1.80 \text{ \AA}$. Poor

agreement is found for the top site and the bridge site (the curve shown is an average over non-equivalent bridge site curves). The main difference between the theoretical curves for the two hollow sites is found in the structure of the peak around 90 eV. Just as in the experimental curve, there is a single peak in the curve for hollow site 1 whereas that peak is split into two peaks separated by 12 eV in the case of hollow site 2. The other regions of the hollow site 1 curve also agree slightly better with experiment than the hollow site 2 curve does. Unfortunately, the differences between the two hollow site calculated curves are not as great at $d_{\perp} = 1.80 \text{ \AA}$ as they are at other values of d_{\perp} . To demonstrate this point, the theoretical hollow site NPD curves for $d_{\perp} = 1.60 \text{ \AA}$ and 2.00 \AA are shown in Fig. 4. The differences between sites 1 and 2 are significant at many energies for both cases. Certain peaks are shifted by 5-10 eV from one hollow site to the other. The accuracy of the d_{\perp} value was determined with a procedure outlined earlier.¹ We find $d_{\perp} = 1.80 \pm 0.04 \text{ \AA}$ for this case. If one assumes the bulk structure for the surface layer of nickel atoms, the Se-Ni bond length is $2.31 \pm 0.03 \text{ \AA}$.

We have presented a case in which NPD has been able to differentiate between a selenium atom in two different sites at the same d_{\perp} . By contrast, SEXAFS¹⁴ would not be particularly valuable for this case if only the first nearest neighbor distance were obtained, because that distance is essentially the same for the two hollow sites. Polarization-dependent SEXAFS¹⁵ can determine the surface-atom coordination number, allowing one to distinguish between top, bridge, and hollow sites, but not between the two different types of threefold

hollow sites. Second and third nearest neighbor distances¹⁶ would have to be obtained to determine the site unambiguously with SEXAFS. Azimuthal photoelectron diffraction (APD), on the other hand, could be applied successfully to this problem because of its sensitivity to the orientation of the substrate atoms relative to the adsorbate atoms. This was demonstrated in a recent APD study of the iodine on Ag(111) system,^{17,18} in which theoretical APD curves by Kang et al.¹⁸ for the two threefold hollow sites were similar in structure but out of phase by 60°. Comparison of these theoretical curves to the experimental data of Farrell et al.¹⁷ led to the conclusion that the iodine atoms occupy both hollow sites at low coverages. Unfortunately, APD was not particularly sensitive to the d_{\perp} spacing in that experiment, and in general APD has difficulty in determining d_{\perp} if the adsorbate is located substantially above the surface.¹⁹

The determination of hollow site 1 with $d_{\perp} = 1.80 \text{ \AA}$ as the geometry of the annealed p(2x2)Se overlayer on Ni(111) also, in effect, provides a structural determination of the low coverage, disordered overlayer shown in Fig. 2, as the two experimental curves are almost identical. This is an important result, as it again demonstrates that NPD can deal with disordered systems.² It is not surprising that the small number of selenium atoms on the surface in the low coverage regime (0.1 monolayer) find the same site to be energetically favorable as in the one-quarter monolayer coverage. In both cases, there is some distance between the selenium atoms and consequently adatom-adatom interactions should be fairly small. For this disordered Se overlayer on Ni(111), the selenium is situated in hollow site 1

(vacancy below) with $d_1 = 1.80 \pm 0.05 \text{ \AA}$. The Se-Ni bond length is $2.31 \pm 0.04 \text{ \AA}$.

Evidence for the presence of multiple adsorption sites was obtained from a temperature dependence study of the $p(2 \times 2)\text{Se-Ni}(111)$ system. The annealed $p(2 \times 2)\text{Se}$ overlayer for which an NPD curve is shown in Fig. 2 was prepared by heating the surface to 500 K after the H_2Se exposures. A second $p(2 \times 2)$ overlayer, which will be referred to as the frozen surface, was prepared at 120 K and held at that temperature before and during the NPD study. Both samples gave good $p(2 \times 2)$ LEED patterns, although that of the annealed surface exhibited sharper spots. The NPD result for the frozen surface is also shown in Fig. 2. Both the annealed and the frozen surface results were reproducible on three separate surface preparations. The frozen surface gave peaks within a few eV of those observed from the annealed $p(2 \times 2)$ surface, but there is an additional peak in the frozen surface NPD curve at 102 eV kinetic energy which is located in a valley of the annealed surface curve. Visual inspection of the curves leads to the hypothesis that the Se can be frozen into multiple binding sites by performing exposures at low temperatures, and that by heating the surface, the preferred site becomes populated exclusively.

The above interpretation is borne out by the theoretical calculations. If the calculated NPD curves for $p(2 \times 2)\text{Se-Ni}(111)$ from Fig. 3 are compared to the frozen $p(2 \times 2)$ data, no single theoretical curve is able to account for all the features in the experimental curve. Consequently, a combination of two or more theoretical curves is required to produce a good theory-experiment fit. Inspection of these curves

indicated that several of the peaks in the hollow 1, hollow 2, and top site curves correspond fairly closely with peaks in the experimental curve. This led to a more quantitative attempt to determine the structure by adding together the three curves with different weightings. Due to the relative closeness of the two hollow site curves in comparison to the top site curve, an average of the two hollow site curves was taken. This average (called "Hollow") is shown in Fig. 5, along with the top site curve (reproduced from Fig. 3). If the hollow and top site curves are normalized (by photoemission intensity per selenium atom) and added together with equal weighting, the resulting NPD curve ("Average of Top and Hollow") shows very good agreement with experiment, as indicated in Fig. 5. This curve actually contains the following contributions (after normalization): 50% top site ($d_1 = 2.30 \text{ \AA}$), 25% hollow site 1 ($d_1 = 1.80 \text{ \AA}$), and 25% hollow site 2 ($d_1 = 1.80 \text{ \AA}$). Note that the extra peak in the frozen $p(2 \times 2)$ curve at 10^2 eV is reproduced, as well as the energy difference between the two large peaks at 81 and 132 eV (51 eV). The difference between those same peaks in the averaged hollow site data is only 43 eV, so the top site contribution is important in establishing a good fit for those two peaks as well. It is reasonable to expect that both hollow site 2 and the top site will be occupied under these conditions, because at 120 K, atoms can be frozen into sites which are not as energetically favored as hollow site 1. We conclude that there are roughly an equal number of top and hollow bonded selenium atoms on the surface. This is the first evidence from NPD for multiple site behavior.

Finally, the higher coverage $(\sqrt{3}\times\sqrt{3})R30^\circ$ Se on Ni(111) system was also studied. The LEED patterns observed were not as sharp as those seen by other workers,¹¹ probably because the coverage of 0.5 monolayer is considerably greater than the 0.33 monolayer coverage for a perfect $(\sqrt{3}\times\sqrt{3})R30^\circ$ overlayer. Unfortunately, no coverage between 0.25 and 0.5 monolayers was studied. As shown in Fig. 2, the $(\sqrt{3}\times\sqrt{3})R30^\circ$ overlayer showed a smaller NPD effect than the other overlayers studied. The size of the modulations is so small in this case that it is very difficult to make an accurate structural determination. It appears that either three or more high symmetry sites are significantly occupied, or that the coverage is so high that the selenium atoms are occupying low symmetry sites as well. Calculations for the $(\sqrt{3}\times\sqrt{3})R30^\circ$ overlayer were carried out, but no successful fit with the experimental data was obtained by assuming either a single high symmetry adsorption site or a combination of two such sites.

2. The $c(2\times 2)$ Selenium and Sulfur Overlayers on Ni(011)

In this subsection we report the results of the first NPD studies of adsorption on a (011) surface. The adsorbates Se and S were chosen in part because of the ease in which the $c(2\times 2)$ overlayers can be prepared on Ni(011) and the relatively large photoemission cross-sections of the Se(3d) and S(2p) levels.

A LEED pattern for the $c(2\times 2)$ Se overlayer on Ni(011) has been observed¹⁰ but no intensity analysis has been published. The experimental NPD curve for this system is presented in Fig. 6, along with calculated curves for selenium in the hollow site ($d_1 = 1.10 \text{ \AA}$), the

long bridge site ($d_{\perp} = 1.54 \text{ \AA}$), the short bridge site ($d_{\perp} = 2.00 \text{ \AA}$), and the top site ($d_{\perp} = 2.30 \text{ \AA}$). The experimental geometry is indicated in the figure. Excellent agreement is found for the hollow site, with poor agreement for all other sites. Thus, NPD produces a clear preference for selenium in the hollow site with $d_{\perp} = 1.10 \text{ \AA}$, with an uncertainty of $\pm 0.04 \text{ \AA}$. The Se-Ni bond length is $2.42 \pm 0.02 \text{ \AA}$. It should be emphasized that this is the first structural determination of a selenium overlayer on Ni(011).

The structure of the $c(2 \times 2)S$ overlayer on Ni(011) has been studied previously by LEED intensity analysis. The sulfur was found to bond in the hollow site above the (011) surface with $d_{\perp} = 0.93 \text{ \AA}$.⁸ The experimental NPD curve for the system is shown in Fig. 7. Above the experimental data, theoretical curves for the hollow site ($d_{\perp} = 0.94 \text{ \AA}$), the long bridge site ($d_{\perp} = 1.30 \text{ \AA}$), the short bridge site ($d_{\perp} = 1.80 \text{ \AA}$), and the top site ($d_{\perp} = 2.20 \text{ \AA}$) are plotted. Excellent agreement is found for both the hollow site and the top site, because the theoretical curves for those two sites are very similar in the energy range studied; i.e., 20–150 eV. Extending the curve to higher kinetic energies would have allowed us to choose between hollow and top sites, as the theoretical curves do show differences above 150 eV. This case provides an example of an accidental coincidence between two theory curves over a short energy range,²⁰ and shows the need to take as wide a data range as possible. This work therefore only partially confirms the LEED result in the sense of excluding both bridge sites, but a unique structure would require a longer data range, with more NPD peaks, to distinguish between the hollow and the top site. The

accidental coincidence could also be obviated by taking photoelectron diffraction curves at off-normal emission angles.²¹

E. CONCLUSIONS

In this chapter, we have reported the results of a series of experiments designed to further assess the value of NPD as a surface structure sensitive technique. Some conclusions are given below:

1. NPD has been used successfully to study systems that have not yet been studied by any other accurate structural technique.
2. NPD seems to be particularly well suited for studying disordered adsorbate systems and systems which have two-dimensional order but contain domains of two adsorption sites.
3. NPD has the potential to select between sites which have the same geometry with respect to the first substrate layer but have a different geometry with respect to the second layer.
4. The importance of taking an extended range of data has been demonstrated by the inability of NPD to select between two different sites which have similar theoretical curves over a short energy range.

REFERENCES

- *This chapter was published: D. H. Rosenblatt, S. D. Kevan, J. G. Tobin, R. F. Davis, M. G. Mason, D. R. Denley, D. A. Shirley, Y. Huang, and S. Y. Tong, Phys. Rev. B 26, 1812 (1982).
1. D. H. Rosenblatt, J. G. Tobin, M. G. Mason, R. F. Davis, S. D. Kevan, D. A. Shirley, C. H. Li, and S. Y. Tong, Phys. Rev. B 23, 3828 (1981), and references therein.
 2. S. D. Kevan, D. H. Rosenblatt, D. R. Denley, B.-C. Lu, and D. A. Shirley, Phys. Rev. B 20, 4133 (1979).
 3. C. H. Li and S. Y. Tong, Phys. Rev. Lett. 42, 901 (1979).
 4. S. D. Kevan, R. F. Davis, D. H. Rosenblatt, J. G. Tobin, M. G. Mason, D. A. Shirley, C. H. Li, and S. Y. Tong, Phys. Rev. Lett. 46, 1629 (1981).
 5. C. H. Li, A. R. Lubinsky, and S. Y. Tong, Phys. Rev. B 17, 3128 (1978).
 6. See, for example, S. Y. Tong and C. H. Li, Crit. Rev. Solid State Sci. 10, 209 (1981).
 7. Z. Hussain, D. A. Shirley, S. Y. Tong, and C. H. Li, Proc. Natl. Acad. Sci. USA 78, 5293 (1981).
 8. J. E. Demuth, D. W. Jepsen, and P. M. Marcus, Phys. Rev. Lett. 32, 1182 (1974).
 9. S. D. Kevan and D. A. Shirley, Phys. Rev. B 22, 542 (1980); S. D. Kevan, Ph.D. thesis, University of California, Berkeley, 1980, unpublished.
 10. G. E. Becker and H. D. Hagstrom, Surface Sci. 30, 505 (1972).
 11. T. Capehart and T. N. Rhodin, J. Vac. Sci. Technol. 16, 594 (1979).
 12. S. Wakoh, J. Phys. Soc. Jpn. 20, 1894 (1965).

13. S. D. Kevan, J. G. Tobin, D. H. Rosenblatt, R. F. Davis, and D. A. Shirley, *Phys. Rev. B* 23, 493 (1981).
14. P. H. Citrin, P. Eisenberger, and R. C. Hewitt, *Phys. Rev. Lett.* 41, 309 (1978).
15. P. H. Citrin, P. Eisenberger, and R. C. Hewitt, *Phys. Rev. Lett.* 45, 1948 (1980).
16. A second nearest neighbor distance has recently been observed. (S. Brennan, J. Stohr, and R. Jaeger, *Phys. Rev. B* 24, 4871 (1981)).
17. H. H. Farrell, M. M. Traum, N. V. Smith, W. A. Royer, D. P. Woodruff, and P. D. Johnson, *Surface Sci.* 102, 527 (1981).
18. W. M. Kang, C. H. Li, and S. Y. Tong, *Solid State Commun.* 36, 149 (1980).
19. P. J. Orders, R. E. Connelly, N. F. T. Hall, and C. S. Fadley, *Phys. Rev. B* 24, 6163 (1981).
20. C. H. Li and S. Y. Tong, *Phys. Rev. B* 19, 1769 (1979).
21. D. H. Rosenblatt, S. D. Kevan, J. G. Tobin, R. F. Davis, M. G. Mason, D. A. Shirley, J. C. Tang, and S. Y. Tong, *Phys. Rev. B* 26, 3181 (1982).

FIGURE CAPTIONS

- Figure 1. (a) Experimental arrangement for all Se-Ni(111) studies, showing the orientation of the incident photon beam ($h\nu$), the photon vector potential (\vec{A}), and the outgoing photoelectron direction (e^-). b) View of the Ni(111) crystal face showing the orientation of the first layer of atoms. c) Positions of the four possible high symmetry adsorption sites with respect to the first and second layer of substrate atoms.
- Figure 2. Experimental NPD results for the four overlayers of Se on Ni(111) studied.
- Figure 3. Experimental NPD curve for the annealed $p(2 \times 2)$ Se-Ni(111) system compared with calculated curves.
- Figure 4. Comparison of calculated curves for a $p(2 \times 2)$ Se-Ni(111) overlayer situated in hollow site 1 and in hollow site 2 at two different d_{\perp} spacings.
- Figure 5. Experimental NPD curve for the frozen $p(2 \times 2)$ Se-Ni(111) surface compared with calculated curves.
- Figure 6. Experimental NPD results for $c(2 \times 2)$ Se-Ni(011) compared with calculated curves for the experimental arrangement shown.
- Figure 7. Experimental NPD curve for $c(2 \times 2)$ S-Ni(011) compared with calculated curves. The experimental arrangement is the same as in Fig. 6.

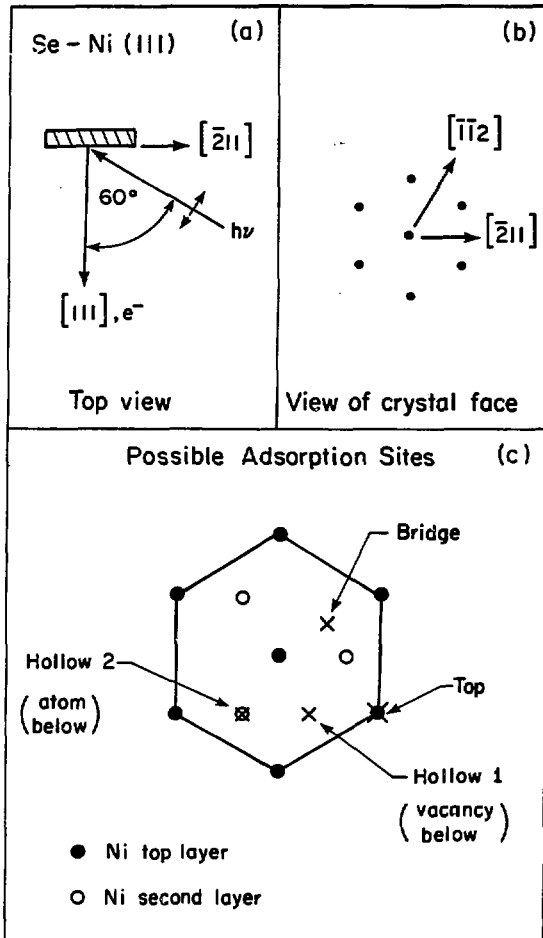


Fig. 1

XBL8111-12014

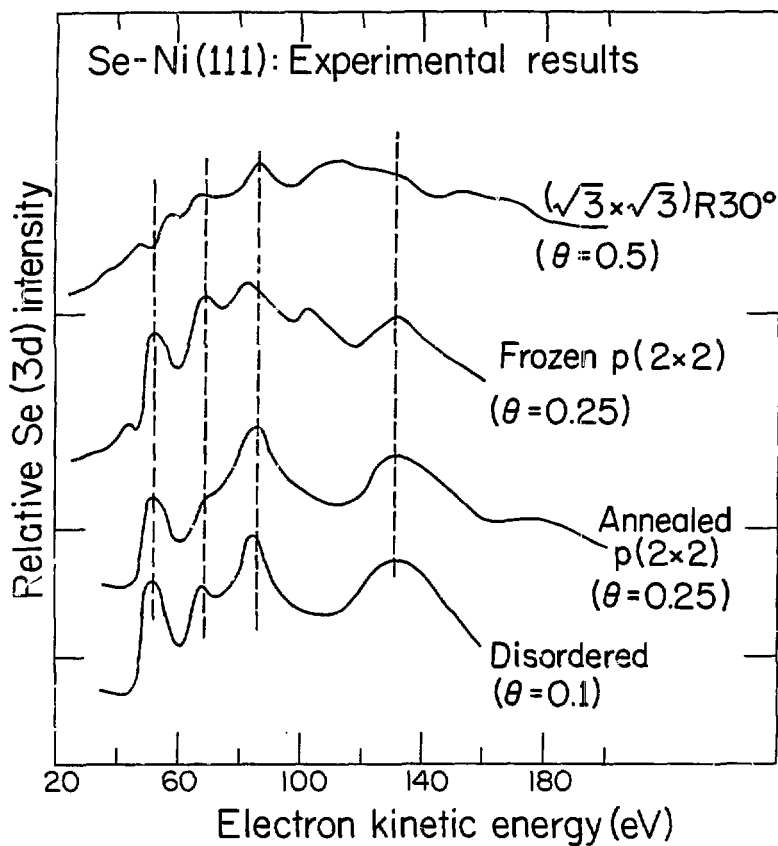
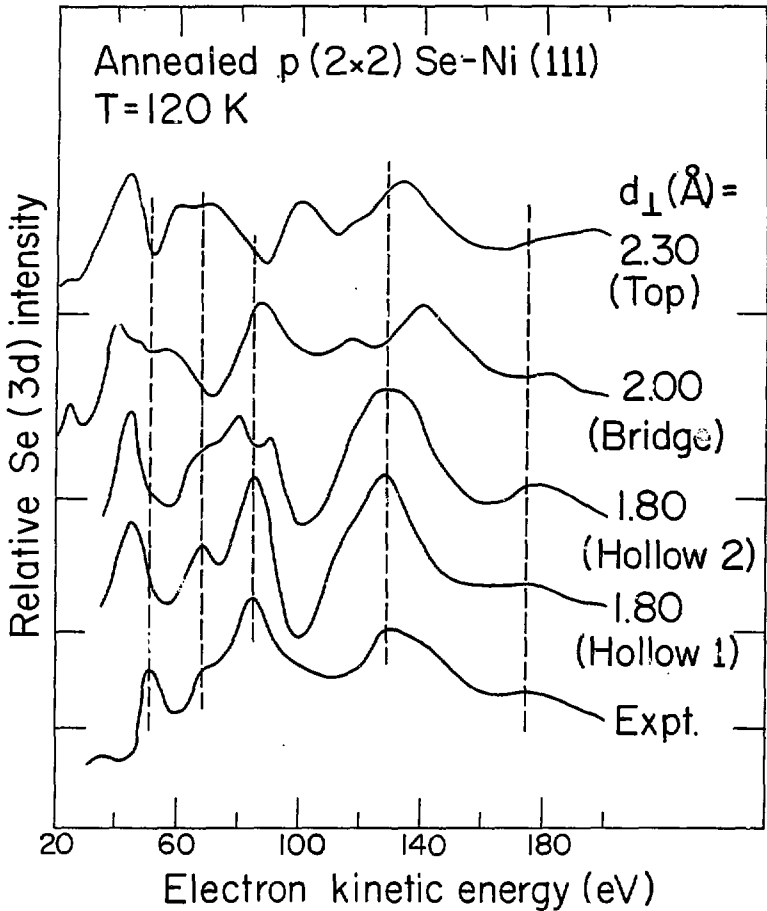


Fig. 2

XBL0111-12020



XBL 8/11-12019

Fig. 3

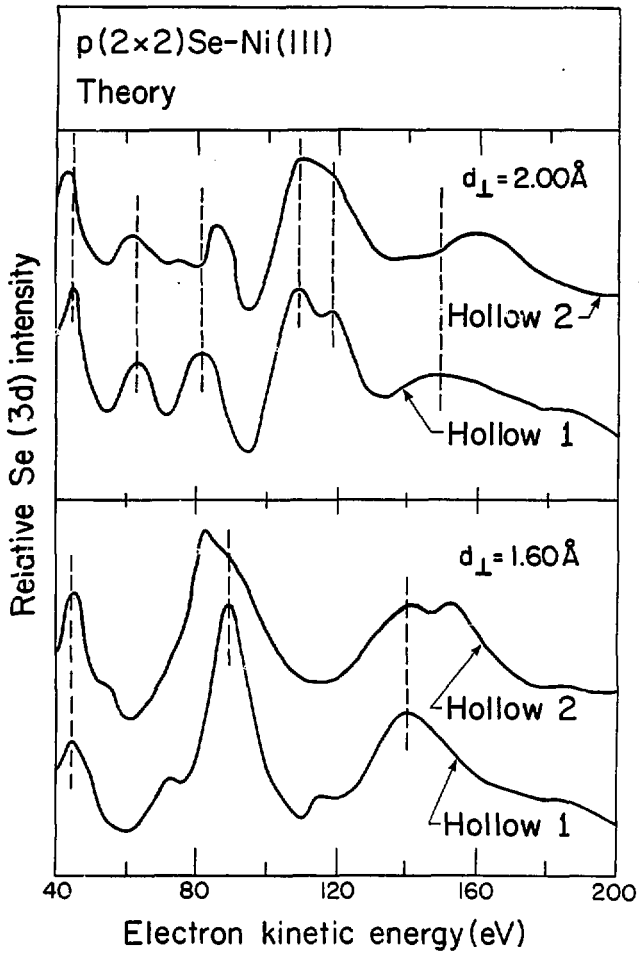


Fig. 4

XBL8111-12016

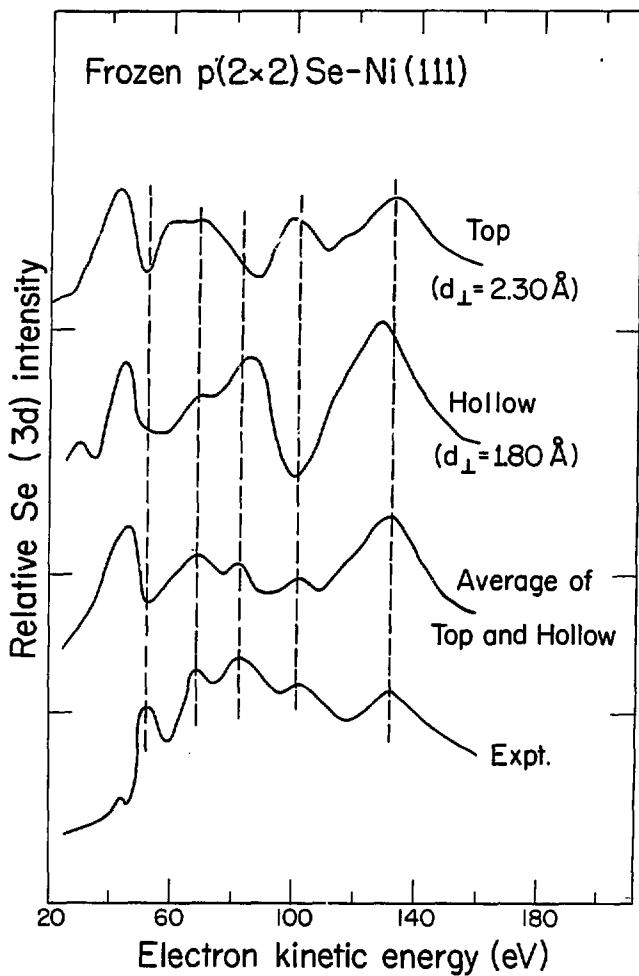


Fig. 5

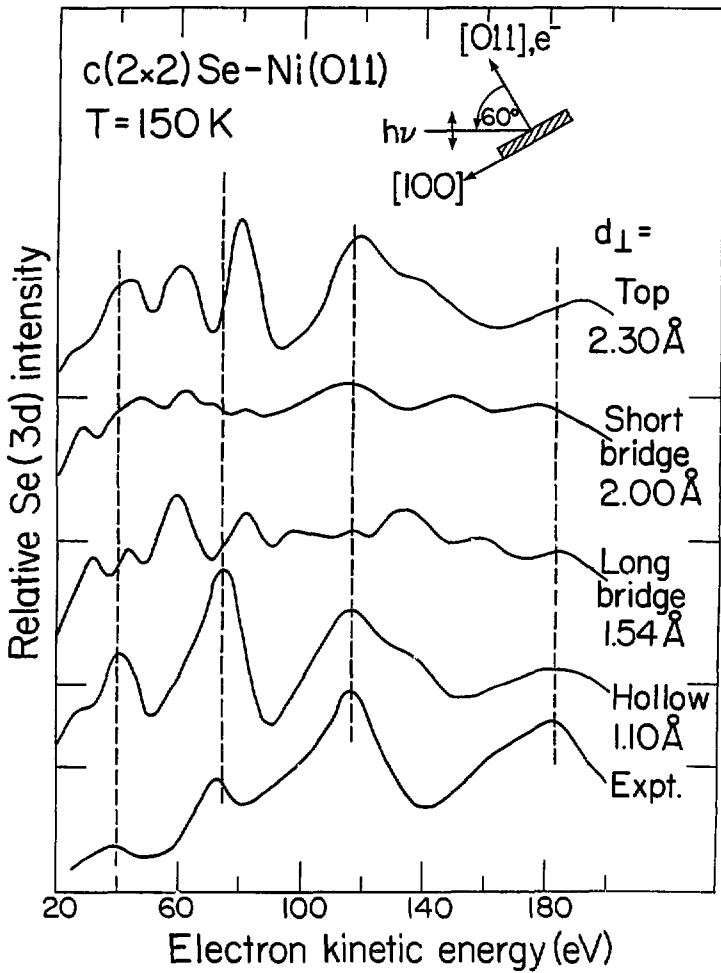
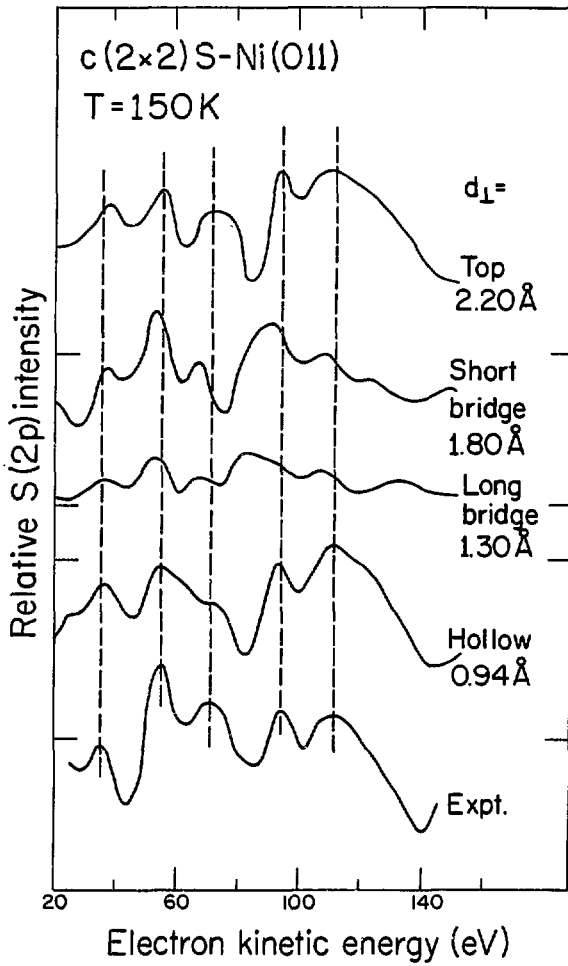


Fig. 6



XBL 81-11-12023

Fig. 7

VI. OFF-NORMAL PHOTOELECTRON DIFFRACTION STUDY OF THE
c(2x2) SELENIUM OVERLAYER ON Ni(001)*

A. INTRODUCTION

Photoelectron diffraction (PD) can be observed by measuring the angle-resolved photoemission intensity from a core level of an adsorbate atom or molecule bonded to a single crystal metal surface. If the photon energy $h\nu$ is varied and the core-level photoelectrons are collected in the direction normal to the crystal face, diffraction of the photoelectrons can yield a strongly oscillatory dependence of the photoelectron intensity on kinetic energy. This specialized case of PD, termed normal photoelectron diffraction (NPD), has been used to determine the structures of overlayers adsorbed on metal surfaces.¹⁻⁶ The first experimental observation of NPD from a core level was made in 1978.¹ Dynamical scattering theory with calculated dipole matrix elements and phase shifts was used to analyze the data and illustrate their usefulness. This effect has now been observed in a large number of adsorbate-substrate systems and is found to be particularly suitable for accurate determination of the spacing between an adsorbate layer and the substrate (d_1). Structural information has been generally derived from a comparison of experimental and theoretical NPD curves,¹⁻⁷ although a more explicit method has been developed recently.^{3,8} In this chapter, we demonstrate for the first time that off-normal energy-dependent PD can also be used to derive accurate surface structures.

In an earlier paper,⁴ we observed that the modulations in off-normal PD were not nearly as pronounced as those in NPD, making an accurate structural determination more difficult. In that work, off-normal data for the $c(2 \times 2)\text{Se}(3d)\text{-Ni}(001)$ system, taken at a coarse angular mesh, were presented. In this chapter, we report off-normal PD curves of the same system, taken at intervals of 5° in polar angle, for two different azimuthal orientations. The finer angular mesh in the new data allows us to follow the evolution of the PD peaks with polar angle more carefully. More importantly, the experimental data have been fitted by multiple scattering theory, allowing an implicit structural determination of the adsorption site of the $c(2 \times 2)\text{Se}$ overlayer on $\text{Ni}(001)$.

Section B contains experimental information. In Section C we briefly discuss the method and inputs of the multiple scattering calculations used to fit the experimental data. In Section D we present and discuss the PD data. An R-factor analysis of the theory-experiment fit is presented in Section E, and conclusions from this work are given in Section F.

B. EXPERIMENTAL

All the data reported here were obtained with an angle-resolved photoemission (ARP) spectrometer described earlier.⁹ The spectrometer has low energy electron diffraction (LEED) and Auger electron spectroscopy capabilities, as well as an adsorbate gas introduction system which allows for effusive beam dosing. The base pressure of the vacuum chamber was 2×10^{-10} torr during all the measurements.

The pressure rose to as high as 5×10^{-9} torr during effusive beam dosing. The Ni(001) crystal was oriented to within 1° of the [001] direction. The crystal was cleaned by hot (1025 K) and room temperature cycles of argon-ion sputtering followed by annealing to 875 K, resulting in a surface essentially free of impurities with a sharp (1x1) LEED pattern. The c(2x2)Se overlayer on Ni(001) was prepared by directing an effusive beam of H_2Se at the crystal, which was heated to 500 K. An exposure of 20-30 L was required to produce a sharp c(2x2) LEED pattern on Ni(001).

The experiments were performed on Beam Line I-1 at the Stanford Synchrotron Radiation Laboratory (SSRL). Low resolution ARP spectra were taken of the Se(3d) level, which has a binding energy of 62 eV with respect to the vacuum level. Spectra were taken at intervals of 3 eV in photon energy. The angle-resolved relative intensity of this level was deduced by calculating the area of the core level peaks (after background subtraction) and adjusting for photon flux and analyzer transmission. The kinetic energy range of the resulting PD curves was generally 40-200 eV. Experimental geometries are indicated in the figures.

C. THEORY

The multiple scattering theory used to calculate the photoemission intensity versus energy (IE) curves was described earlier.^{7,10} The 3d initial state wavefunction of Se was obtained from a self-consistent X_α scattered-wave calculation of a Ni_5Se cluster. Dipole transition matrix elements were calculated at each photon energy. The final

state was calculated at each kinetic energy by a Green's function method corresponding to the $c(2 \times 2)\text{Se-Ni}(001)$ slab geometry. All multiple scattering of the photoelectron was included until numerical convergence was reached.

Inputs to the multiple scattering method include: (1) substrate (nickel) phase shifts obtained from the self-consistent band structure potential of Wakoh,¹¹ and (2) Se phase shifts obtained from the same $X\alpha$ scattered-wave calculation that generated the Se(3d) wavefunction. The imaginary part of the optical potential for the final state was taken to be $V_I = 3.8[(E + V_0)/(90 + V_0)]^{1/3}$, where E is the energy in electron volts above the vacuum, and the inner potential used was $V_0 = 13.2$ eV. Earlier, we had used $V_0 = 11.7$ eV for Se on Ni(001),¹² but the R-factor analysis described in Section V gave a slightly better value for $V_0 = 13.2$ eV. For example, the normalized R factor at the optimal structure (see Section E) is 0.789 for $V_0 = 11.2$ eV and 0.760 for $V_0 = 13.2$ eV, indicating a 4% improvement. Although the 2 eV shift slightly improved the R factor, the same d_1 spacing was chosen by either $V_0 = 11.2$ eV or 13.2 eV.

The Se(3d) level was placed at 62 eV below vacuum. Calculations of the IE curves were made for the same energy range as the data, i.e., 40–200 eV. The Se atom was placed at the fourfold hollow site at Se-Ni perpendicular spacings (d_1) of 1.45, 1.55, 1.65 and 1.75 Å. Earlier analyses have convincingly shown that the adsorption site is the fourfold hollow.^{2,4,12-14} In this study, we did not place the Se at other binding registries, except for $d_1 = 2.34$ Å in the top site (see Section D and Fig. 4).

D. RESULTS AND DISCUSSION

In an earlier paper,⁴ we presented limited off-normal photoelectron diffraction data on $c(2 \times 2)\text{Se-Ni}(001)$. In that work, data were taken for emission into the [100] azimuth at polar angles of 15° , 30° , and 45° , and into the [110] azimuth at polar angles 18° , 36° , and 54° . The curves were rich in structure, but the intensity modulations were much smaller than those at normal emission. When the photoemission is normal, waves scattered to the detector by atoms arranged symmetrically around the emitting atom interfere constructively with each other at the detector. Therefore, the conditions of constructive interference between the direct wave and the wave scattered by each of these symmetrically arranged neighbors are the same, leading to a series of large, well-separated peaks in the NPD curve. However, at off-normal angles of emission, the conditions of constructive interference between direct and scattered waves are different for each of these neighbor atoms, leading to a collection of overlapping peaks. Consequently, as the detector is rotated off normal, new peaks are seen, and the overall peak-to-valley ratio decreases. The latter can be seen in Fig. 1, where PD curves are shown for emission in the [100] azimuth with polar angles $\theta = 0^\circ, 5^\circ, 10^\circ, 15^\circ, 20^\circ$ and 25° . The experimental geometry for this data set is shown in Fig. 2. The NPD curve ($\theta = 0^\circ$) exhibits the greatest peak-to-valley ratio. As the detector is rotated off normal, the modulations get smaller. At $\theta = 25^\circ$, the modulations are small enough that the underlying atomic cross-section is becoming apparent. An example of a new peak which emerges at off-normal emission is seen in Fig. 1. This peak is first seen at

$\theta = 10^\circ$ in the [100] azimuth at 111 eV kinetic energy, and becomes the most prominent feature in the NPD curve by $\theta = 25^\circ$. The peak disperses from 111 eV at $\theta = 10^\circ$ to 103 eV at $\theta = 25^\circ$. The main peaks present in the PD curve at normal emission (kinetic energy 89 and 138) decrease in intensity while dispersing slightly in energy with polar angle.

Similar effects are seen if the crystal is rotated azimuthally about the sample normal by 45° , so that the photon beam and emission direction are both located in the [110] azimuth. This experimental geometry is shown in Fig. 3. These experimental PD curves are also shown in Fig. 1. Again, the peak-to-valley contrast is greatest at normal emission. The two main peaks in the normal emission curve are at kinetic energy 89 and 137 eV. A new peak at 110 eV appears at $\theta = 10^\circ$ and grows in intensity through $\theta = 25^\circ$.

A comparison between the PD curves for the two azimuths studied is of interest at this point. For core level emission from an adsorbate in a fourfold hollow site (C_{4v} symmetry) the PD intensity at normal emission is independent of the azimuthal angle ϕ of the incident photon beam. Thus, the two curves at $\theta = 0^\circ$ of Fig. 1 indicate the high degree of reproducibility of the data at equivalent but non-identical conditions. As the detector is moved off normal, we are comparing two sample geometries which differ by 45° not only in the azimuthal orientation of the photon polarization vector, but also in the azimuthal orientation of photoelectron emission. The second effect induces significant differences between pairs of curves with the same polar angle, especially for $\theta \geq 15^\circ$. At $\theta = 5^\circ$ the differences are minor and at $\theta = 10^\circ$ the major difference is in the position of the first PD

peak. At $\theta = 15^\circ$ and $\theta = 20^\circ$, the curves are still similar above 90 eV kinetic energy. Only at $\theta = 25^\circ$ do PD curves for the two azimuths look substantially different at all energies.

We now turn to the theoretical analysis of the data in Fig. 1. The data for the [100] azimuth are reproduced in Fig. 2 and compared with PD calculations for Se in the fourfold hollow site at $d_{\perp} = 1.55 \text{ \AA}$, where d_{\perp} is the perpendicular distance between the $c(2 \times 2)$ Se overlayer plane and the nickel surface. The agreement is quite good for all angles sampled. Visual inspection indicates that the quality of the fit is extremely good at small polar angles ($\theta \leq 15^\circ$) but worsens somewhat at the larger polar angles sampled. Theoretical calculations for emission into the [110] azimuth are shown in Fig. 3 along with the experimental curves, which are reproduced from Fig. 1. Calculated PD curves for Se in the fourfold hollow site with $d_{\perp} = 1.55 \text{ \AA}$ are presented. The fit with the experimental data is again quite good. Just as for the [100] azimuth, the fit is excellent for smaller polar angles and deteriorates as θ gets large. An R factor analysis was carried out for the d_{\perp} values of 1.45, 1.55, 1.65, and 1.75 \AA using all data from both azimuths studied. The $d_{\perp} = 1.55 \text{ \AA}$ spacing was found to give the optimum (lowest) R factor. Details of the R factor analysis are given in the next section. The determination of $d_{\perp} = 1.55 \text{ \AA}$ is in excellent agreement with our previous NPD study on this system⁴ and with LEED intensity analyses in the literature^{13,14}.

A major benefit of studying off-normal photoelectron diffraction is that a comparison of many experimental curves to theory provides a self-consistency check of the NPD results, in the same manner that

LEED intensity analysis at off-normal incidences can be used to confirm results obtained by studying the LEED beams at normal incidence. At the same time, caution should be taken in examining the PD fits at large polar angles, as both experimental and calculated curves exhibit smaller oscillations and it is more difficult to establish whether a good fit exists. The peak positions and intensities change more rapidly with angle at large polar angles because there are more inequivalent atoms around the emitting site. Consequently, small errors in the measurement of the polar angle will cause shifts in the NPD peaks which reduce the quality of the theory-experiment fit at large polar angles.

The close similarity between all six experimental PD curves with $\theta \leq 10^\circ$ ($\theta = 0^\circ, 5^\circ, \text{ and } 10^\circ$ in both azimuths) presents the possibility that NPD data could be taken into a much larger solid angle of emission (resulting in a dramatic reduction of data collection time) without significantly degrading the structural accuracy of NPD. In a previous paper,⁴ we used NPD to determine that selenium is situated above the hollow sites on Ni(001) with $d_{\perp} = 1.55 \pm 0.04 \text{ \AA}$. In that study (as well as this work), the angular acceptance of our electron energy analyzer was a half-angle of 3° . If the angular acceptance is increased to 10° half-angle, the number of photoelectrons collected will increase by more than 10 times if one assumes an isotropic angular distribution of photoelectrons over the range $0^\circ \leq \theta \leq 10^\circ$. We estimate that the corresponding decrease in structural accuracy will be considerably less than the current experimental error; i.e., the increased angular acceptance should introduce an additional error of

about $\pm 0.02 \text{ \AA}$ to the d_{\perp} determination for Se on Ni(001). We conclude that future NPD experiments could benefit from using a larger angular acceptance of photoelectrons.

Occasionally, the theoretical NPD curves for two different sites exhibit an "accidental coincidence" in peak positions which makes it more difficult to distinguish the correct site geometry. In these cases, most or all of the peaks in one curve have energy positions which differ by 5 eV or less from the energies of peaks in the second curve. For example, in an earlier paper, Li and Tong¹⁵ noted that for normal emission from the c(2x2)Se-Ni(001) system, there is an accidental coincidence of diffraction peaks between $d_{\perp} = 1.55 \text{ \AA}$ (hollow site) and $d_{\perp} = 2.34 \text{ \AA}$ (top site). These authors expected that this accidental coincidence would be lifted when off-normal emission data became available. This is indeed the case, and we show in Fig. 4 the comparison at $\theta = 15^{\circ}$ of experimental data with calculated PD curves for $d_{\perp} = 1.55 \text{ \AA}$ (hollow site) and $d_{\perp} = 2.34 \text{ \AA}$ (top site). The emission direction is along the [100] azimuth. The peak at 88 eV of the hollow site curve is split into two peaks (80 eV and 100 eV) in the top site curve. Near 88 eV, there is a valley for the top site. This comparison definitely rules out the top site as the binding location of c(2x2)Se on Ni(001).

E. R-FACTOR ANALYSIS

To facilitate comparison between theory and experiment, and to compare the "fit" obtained here with other structural analyses, we performed an R-factor analysis on this system. We used a normalized

R factor,¹⁶ which was based on individual R factors defined by Van Hove et al.,¹⁷ Zanazzi and Jona,¹⁸ and Pendry.¹⁹ The normalized R factor (R_N) is defined in Chapter IV, Section C. The only difference between the R_N used here and that defined in Chapter IV is that in this case, the weights A_1, \dots, A_6 are chosen such that the average value of each R factor over the geometries considered in this work is 1.0. The R_N is not normalized to the Zanazzi-Jona R factor,²⁰ as was done in Chapter IV (see below).

The value of R_N , evaluated over the 11 PD curves shown in Figs. 2 and 3 (the two $\theta = 0^\circ$ curves are degenerate, so we took only the one in Fig. 2), is plotted as a function of d_1 in Fig. 5. A well-defined minimum is seen at $d_1 = 1.55 \text{ \AA}$. This result agrees with the determination by visual judgment, and it also agrees with earlier PD analysis at normal emission and with LEED.^{13,14}

To compare the degree of fit with other structural analyses, the value of the Zanazzi-Jona R factor (R_{ZJ})²⁰ for $d_1 = 1.55 \text{ \AA}$ is 0.05. From previous experience, a structural analysis is acceptable if $R_{ZJ} < 0.2$. With this criterion, the overall fit here is substantially above average.

F. CONCLUSIONS

In this chapter, we have demonstrated, for the first time, the use of off-normal energy-dependent photoelectron diffraction curves to determine surface structure. Off-normal PD curves show smaller oscillation amplitudes than NPD curves, but these curves can nevertheless be used to accurately determine the structural parameter d_1 . In the event of an accidental coincidence at normal emission, we have demon-

strated that off-normal PD curves can be used to resolve the coincidence. Due to the rapid decrease of the amplitude of the oscillations at larger θ , the most useful range seems to be between $\theta = 0^\circ$ and $\theta = 15^\circ$.

REFERENCES

- *This chapter was published; D. H. Rosenblatt, S. D. Kevan, J. G. Tobin, R. F. Davis, M. G. Mason, D. A. Shirley, J. C. Tang, and S. Y. Tong, Phys. Rev. B 26, 3181 (1982).
1. S. D. Kevan, D. H. Rosenblatt, D. Denley, B.-C. Lu, and D. A. Shirley, Phys. Rev. Lett. 41, 1565 (1978).
 2. C. H. Li and S. Y. Tong, Phys. Rev. Lett. 42, 901 (1979).
 3. D. H. Rosenblatt, J. G. Tobin, M. G. Mason, R. F. Davis, S. D. Kevan, D. A. Shirley, C. H. Li, and S. Y. Tong, Phys. Rev. B 23, 3828 (1981).
 4. S. D. Kevan, D. H. Rosenblatt, D. R. Denley, B.-C. Lu, and D. A. Shirley, Phys. Rev. B 20, 4133 (1979).
 5. S. D. Kevan, R. F. Davis, D. H. Rosenblatt, J. G. Tobin, M. G. Mason, D. A. Shirley, C. H. Li, and S. Y. Tong, Phys. Rev. Lett. 46, 1629 (1981).
 6. S. Y. Tong and C. H. Li, Crit. Rev. Solid State Sci. 10, 209, 1981.
 7. C. H. Li, A. R. Lubinsky, and S. Y. Tong, Phys. Rev. B 17, 3128 (1978).
 8. Z. Hussain, D. A. Shirley, S. Y. Tong and C. H. Li, Proc. Natl. Acad. Sci. USA 78, 5293 (1981).
 9. S. D. Kevan and D. A. Shirley, Phys. Rev. B 22, 542 (1980).
 10. S. Y. Tong, C. H. Li and A. R. Lubinsky, Phys. Rev. Lett. 39, 498 (1977).
 11. S. Wakoh, J. Phys. Soc. Jpn. 20, 1894 (1965).
 12. C. H. Li and S. Y. Tong, Phys. Rev. Lett. 43, 526 (1979).

13. M. Van Hove and S. Y. Tong, J. Vac. Sci. Technol. 12, 230 (1975);
S. Andersson, J. B. Pendry, B. Kasemo, and M. Van Hove, Phys. Rev. Lett. 31, 595 (1973).
14. J. E. Demuth, D. W. Jepsen and P. M. Marcus, Phys. Rev. Lett. 31, 540 (1973).
15. C. H. Li and S. Y. Tong, Phys. Rev. B 19, 1769 (1979).
16. S. Y. Tong and K. H. Lau, Phys. Rev. B 25, 7382 (1982).
17. M. A. Van Hove, S. Y. Tong, and M. H. Elconin, Surface Sci. 64, 85 (1977).
18. E. Zanazzi and F. Jona, Surface Sci. 62, 61 (1977).
19. J. B. Pendry, J. Phys. C 13, 937 (1980).
20. Our R_5 is derived from the Zanazzi-Jona R factor (Ref. 18),
except for a different coefficient A_5 .

FIGURE CAPTIONS

- Figure 1. Experimental PD data for $c(2 \times 2)\text{Se}(3d)\text{-Ni}(001)$ for emission in the [100] azimuth (solid curves) and the [110] azimuth (dashed curves) as a function of polar angle θ . The experimental geometries for the [100] and [110] azimuths are shown in Figs. 2 and 3, respectively.
- Figure 2. Experimental PD data for the [100] azimuth (solid curves) compared with theoretical calculations for the hollow site with $d_{\perp} = 1.55 \text{ \AA}$ (dashed curves).
- Figure 3. Experimental PD data for the [110] azimuth (solid curves) compared with theoretical calculations for the hollow site with $d_{\perp} = 1.55 \text{ \AA}$ (dashed curves).
- Figure 4. Comparison of (a) experimental PD data for $c(2 \times 2)\text{Se}(3d)\text{-Ni}(001)$ with calculated curves for (b) Se in the hollow site, $d_{\perp} = 1.55 \text{ \AA}$ and (c) Se in the top site, $d_{\perp} = 2.34 \text{ \AA}$. The polar angle of emission is $\theta = 15^{\circ}$ in the [100] azimuth.
- Figure 5. Plot of the normalized R factor versus d_{\perp} spacing.

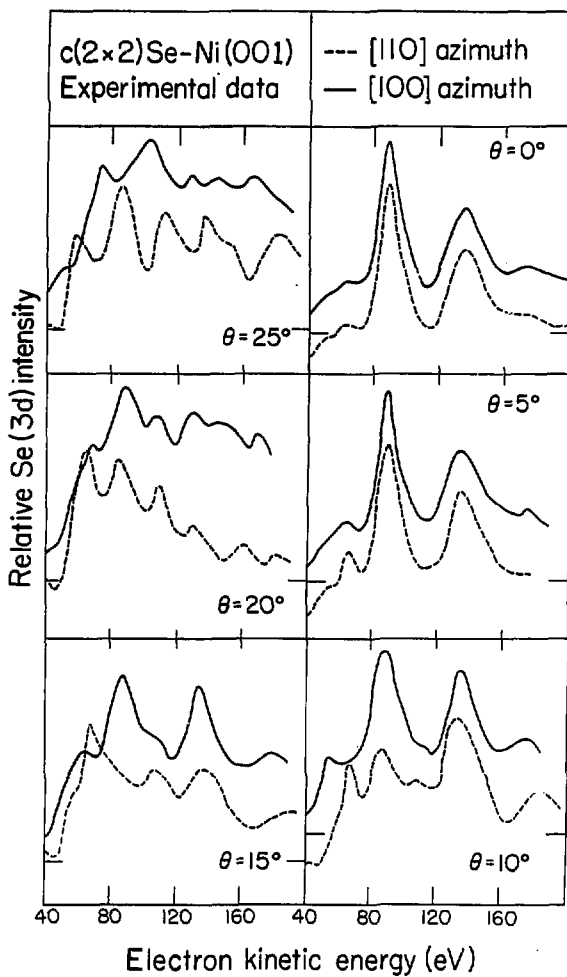
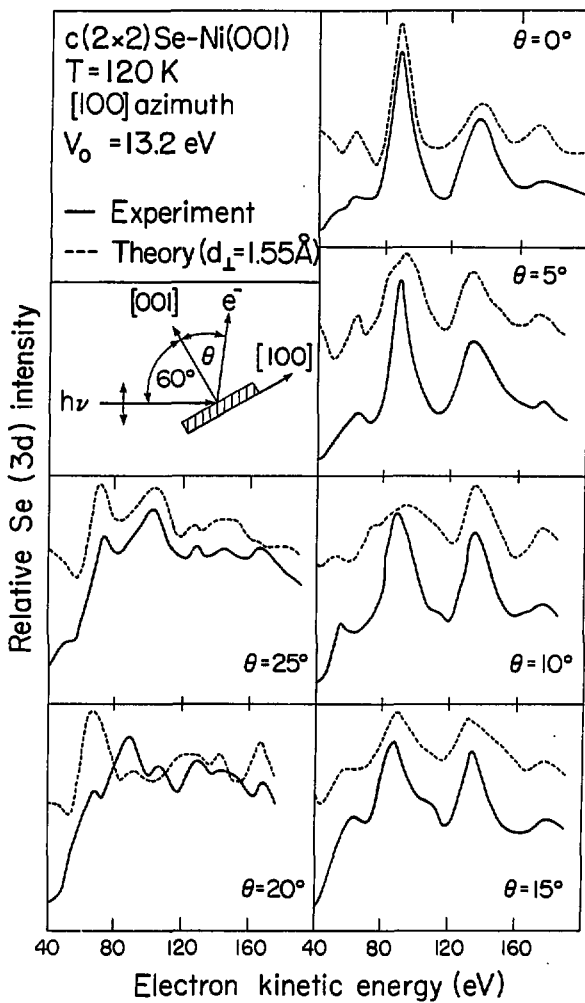


Fig. 1



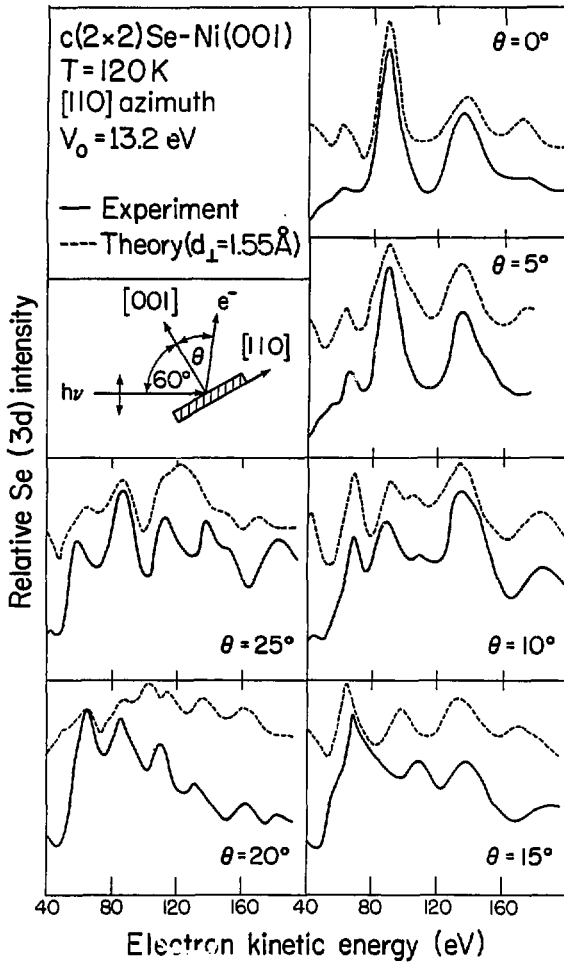


Fig. 3

XBL9111-1201B

c(2×2)Se-Ni(001)

$\theta = 15^\circ$ $V_0 = 13.2$ eV

[100] azimuth

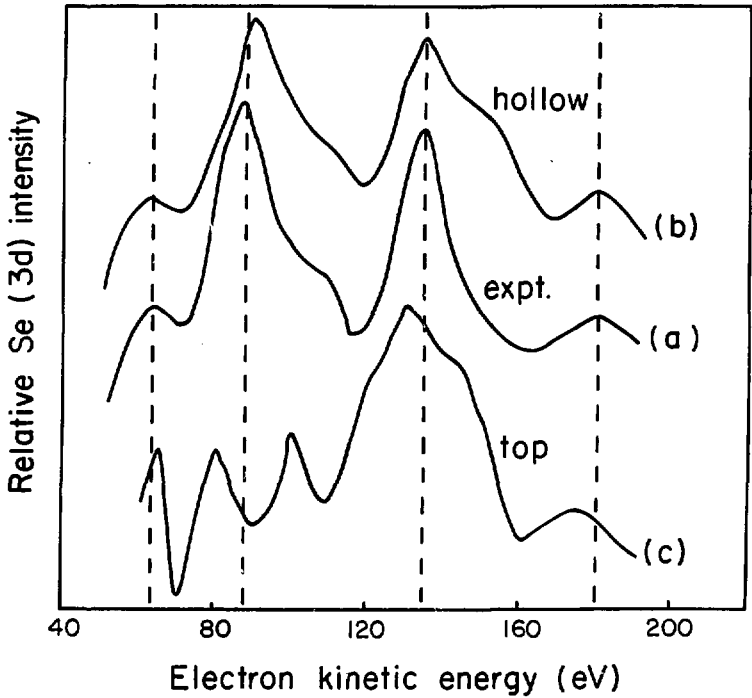


Fig. 4

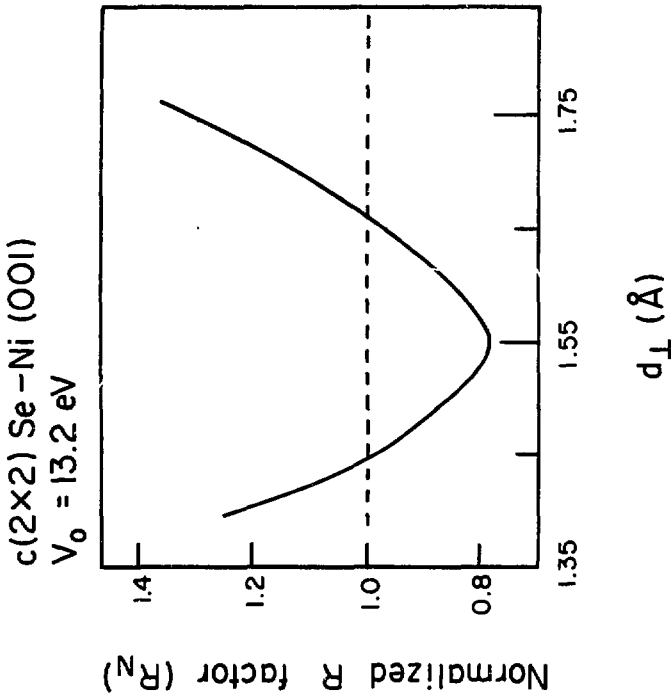


Fig. 5

XBL 822-153

VII. STRUCTURAL DETERMINATION OF A MOLECULAR OVERLAYER SYSTEM
WITH NORMAL PHOTOELECTRON DIFFRACTION: $c(2 \times 2)CO-Ni(001)^*$

A. INTRODUCTION

The determination of molecular adsorbate bonding geometry is of major importance in surface science, but few structures are known to date. One popular experimental strategy combines photoemission, to establish the molecular species and orientation, with low energy electron diffraction (LEED), for subsequent, quantitative structure studies. Recently it has been shown that normal photoelectron diffraction (NPD) alone is sufficient for structure determination in atomic overlayer systems.^{1,2} In this chapter we report experimental evidence that NPD can be used to determine molecular adsorbate structure. We chose to study $c(2 \times 2)CO-Ni(001)$ because it has become a model molecular adsorption system and because LEED structure analysis has been difficult and the subject of controversy prior to the recent establishment of a generally accepted result.³ An NPD structural study has certain advantages relative to LEED. Radiation damage is minimal, long-range order is unnecessary, and the localized nature and phase coherence of NPD permits an independent structural determination for each atomic species in the molecule.

B. EXPERIMENTAL AND THEORY

Experiments were performed on Beam Line I-1 at the Stanford Synchrotron Radiation Laboratory (SSRL) with an apparatus described elsewhere.⁴ By using a grazing-incidence "grasshopper" monochromator equipped with a 1200 line/mm holographic grating during dedicated

operation, we obtained photon flux and resolution sufficient to perform NPD experiments on both the C(1s) and O(1s) adsorbate core levels in the photon energy range $300 \leq h\nu \leq 650$ eV. These experiments, together with our recent C(1s) shape resonance measurements,⁵ are the first systematic ARP studies of these light-element core levels with intermediate energy x-rays. The C(1s) and O(1s) data shown below were presented in the doctoral thesis of S. D. Kevan.⁴ They have been reanalyzed and interpreted in this chapter.

The Ni(001) crystal was cleaned and exposed to CO using standard procedures.⁵ LEED was not performed on the overlayer systems prior to NPD measurements, to avoid the usual primary beam damage.³ No time-dependent degradation of the overlayers (as determined by photoemission) was apparent over several hours of NPD experimentation. LEED measurements after the NPD studies confirmed the c(2x2) structure. This is a significant advantage of NPD in the study of molecular overlayers.

The NPD calculations were performed using a multiple scattering algorithm detailed elsewhere.^{6,7} All orders of multiple scattering were included. Carbon and oxygen phase shifts were generated using the χ_α scattered-wave technique,⁶ while those of nickel were derived from the Wakoh self-consistent band structure potential.⁸ The inner potential (V_0) used was 11.2 eV. The calculations were done for CO with the generally accepted orientation⁵ (bond axis normal to the surface, with the carbon end down), in the top, bridge, and hollow sites, allowing the C-Ni interplanar distance (d_{CNi}^{\perp}) and the CO bond

distance (d_{CO}^{\perp}) to vary in steps of 0.1 Å in a systematic search for the best fit to the experimental curves.

C. RESULTS AND DISCUSSION

From the systematics of these calculations for the C(1s) level in the CO-Ni(001) prototype system, we can draw important conclusions about the NPD process in molecular adsorbates. The theoretical results indicate⁷ that if d_{CO}^{\perp} is held constant and d_{CNi}^{\perp} is varied in successive calculations, the characteristic C(1s) NPD modulation peak energy positions are shifted to higher kinetic energy as d_{CNi}^{\perp} is decreased, in agreement with the trend observed in earlier NPD studies of atomic overlayer systems.¹ In contrast, the peak positions do not disperse with d_{CO}^{\perp} in calculations where d_{CNi}^{\perp} is held constant. These observations imply that the C(1s) experimental NPD curve should be extremely sensitive to d_{CNi}^{\perp} , but not to d_{CO}^{\perp} . This may be understood in terms of the localized nature of the NPD process. For the C(1s) NPD curve the yield structural sensitivity to d_{CO}^{\perp} , the electron would have to undergo at least one scattering event off the oxygen atom. But the dominant scattering from oxygen is a small angle forward scattering, and the phase difference between the scattered wave and the direct wave is essentially independent of the position of the oxygen atom, yielding little sensitivity to d_{CO}^{\perp} .⁷ The situation is manifestly different for large-angle backscattering off nickel, which provides the sensitivity to d_{CNi}^{\perp} . Here, the backscattered wave accumulates phase in twice traversing the distance between ab-

sorbing and scattering atoms, so that substantial structural sensitivity is expected and observed.

The experimental NPD curve for the C(1s) level, shown in the inset in Fig. 1 and in Fig. 3, illustrates the above expectations. It represents the combined results of several experiments on different overlayer preparations and nickel crystals. Individually, peak positions were reproducible to $\pm 1-2$ eV from one experimental curve to another. The match between experimental and theoretical peak positions for $d_{\text{CNi}}^{\perp} = 1.8 \text{ \AA}$ and $d_{\text{CO}}^{\perp} = 1.13 \text{ \AA}$ in the top geometry is excellent; peaks (1,2,3,4) fall at (85,105,126,154) and (88,106,127,154) eV kinetic energy in theory and experiment, respectively. The quality of the experimental-theory fit can be examined quantitatively by observing the trend in $\Delta E = E(\text{theo}) - E(\text{expt})$ for each of the four NPD peaks, as d_{CNi}^{\perp} is varied. These trends are summarized in Fig. 1. The criterion for a perfect match between theory and experiment, $\Delta E = 0$ for each NPD peak, is most nearly met by the $d_{\text{CNi}}^{\perp} = 1.8 \text{ \AA}$ calculation. The systematic behavior shown in Fig. 1 simplifies the assessment of error limits for d_{CNi}^{\perp} . On the low side, which is more important for this case, the 1.7 \AA curve is far outside the acceptable range. We adopt a very conservative lower limit of $d_{\text{CNi}}^{\perp} = 1.76 \text{ \AA}$. On the high side, the longer distances shown are not credible for a C-Ni bond, on chemical grounds. However, even the 1.9 \AA curve is off by several standard deviations. To raise it would require shifting the inner potential by ~ 5 eV, from 11.2 eV to ~ 6 eV, which is physically unacceptable. Our final adopted value is $d_{\text{CNi}}^{\perp} = 1.80 \pm 0.04 \text{ \AA}$, with CO in the top site.

From the above discussion it is clear that the O(1s) NPD curve must be measured to determine d_{CO}^{\perp} from NPD alone. Theoretical and experimental results are summarized in Fig. 2. We were able to collect data over only the limited kinetic energy range $0 \leq E_k \leq 100$ eV because of poor photon flux and monochromator resolution above 650 eV photon energy. In general, measurement of C(1s) and O(1s) NPD intensities near $E_k = 61$ eV was hampered by interference from the Ni(M_{23}, V, V) Auger peak¹ (see e.g., the dashed portion of the experimental curve in Fig. 2b). The theoretical curves (Fig. 2a) for fixed d_{CNi}^{\perp} and various CO bond distances illustrate that NPD structural results are less accurate in this lower energy range because modulation peak position dispersion with d_{\perp} is lower, and additionally, the theoretical NPD curve shape is more model-dependent for $E_k \leq 60$ eV.^{1,7} In spite of these limitations, a good fit of peak positions for $d_{CNi}^{\perp} = 1.8$ Å and $d_{CO}^{\perp} = 1.13$ Å is shown in Fig. 2b. It is encouraging that the fit improves at higher energies. The NPD data show an excellent fit for the isolated molecule bond distance $d_{CO}^{\perp} = 1.13$ Å, consistent with the LEED result of $d_{CO}^{\perp} = 1.1$ Å,³ but an O(1s) study over a wider kinetic energy range is desirable.

A summary of the best theory-experiment fit for both C(1s) and O(1s) levels is shown on the same energy scale in Fig. 3. The C(1s) data close to the edge have been omitted from this study because the shape resonance in the C(1s) level dominates the NPD curve at lower kinetic energies.⁵ A perspective drawing of the c(2x2)CO-Ni(001) structure is shown in Fig. 4.

In conclusion, using normal photoelectron diffraction, the top-bonded CO structure for $c(2 \times 2)\text{CO-Ni}(001)$ has been found, confirming recent detailed LEED investigations.³ Based on these observations and considerations discussed above, NPD shows promise for determining bonding geometries of molecular adsorbates, as a complementary or alternative method to LEED.

REFERENCES

- *This chapter was published: S. D. Kevan, R. F. Davis, D. H. Rosenblatt, J. G. Tobin, M. G. Mason, D. A. Shirley, C. H. Li, and S. Y. Tong, Phys. Rev. Lett. 46, 1629 (1981).
1. D. H. Rosenblatt, J. G. Tobin, M. G. Mason, R. F. Davis, S. D. Kevan, D. A. Shirley, C. H. Li, and S. Y. Tong, Phys. Rev. B 23, 3828 (1981); and references therein.
 2. C. H. Li and S. Y. Tong, Phys. Rev. Lett. 42, 901 (1979).
 3. S. Andersson and J. B. Pendry, Surf. Sci. 71, 75 (1978); Phys. Rev. Lett. 43, 363 (1979); and M. Passler, A. Ignatiev, F. Jona, D. W. Jepsen, and P. M. Marcus, Phys. Rev. Lett. 43, 360 (1979).
 4. S. D. Kevan and D. A. Shirley, Phys. Rev. B 22, 542 (1980); S. D. Kevan, Ph.D. thesis, University of California, Berkeley, 1980, unpublished.
 5. R. F. Davis, S. D. Kevan, D. H. Rosenblatt, M. G. Mason, J. G. Tobin, and D. A. Shirley, Phys. Rev. Lett. 45, 1877 (1980); and references therein.
 6. C. H. Li, A. R. Lubinsky, and S. Y. Tong, Phys. Rev. B 17, 3128 (1978).
 7. C. H. Li and S. Y. Tong, Phys. Rev. Lett. 43, 526 (1979).
 8. S. Wakoh, J. Phys. Soc. Jpn. 20, 1896 (1965).

FIGURE CAPTIONS

- Figure 1. Plot of $\Delta E = E(\text{theory}) - E(\text{experiment})$ versus NPD curve peak number for the C(1s) level in c(2x2)CO-Ni(001) with fixed CO bond length and various carbon-nickel spacings, with CO in the top site. A comparison of calculated ($d_{\text{CNi}}^i = 1.8 \text{ \AA}$, $d_{\text{CO}}^i = 1.13 \text{ \AA}$) and experimental NPD curves is shown in the inset.
- Figure 2. a) Calculated NPD curves for the O(1s) level in c(2x2)CO-Ni(001) for fixed carbon-nickel spacing and various CO bond lengths (top site).
 b) Comparison of the experimental result to the best-fit calculation from (a). The dashed portion of the experimental curve suffers from Ni(M₂₃,V,V) Auger interference.
- Figure 3. Comparison of the best-fit calculation to experiment for both C(1s) and O(1s) levels in c(2x2)CO-Ni(001).
- Figure 4. Perspective drawing of the c(2x2)CO-Ni(001) structure.

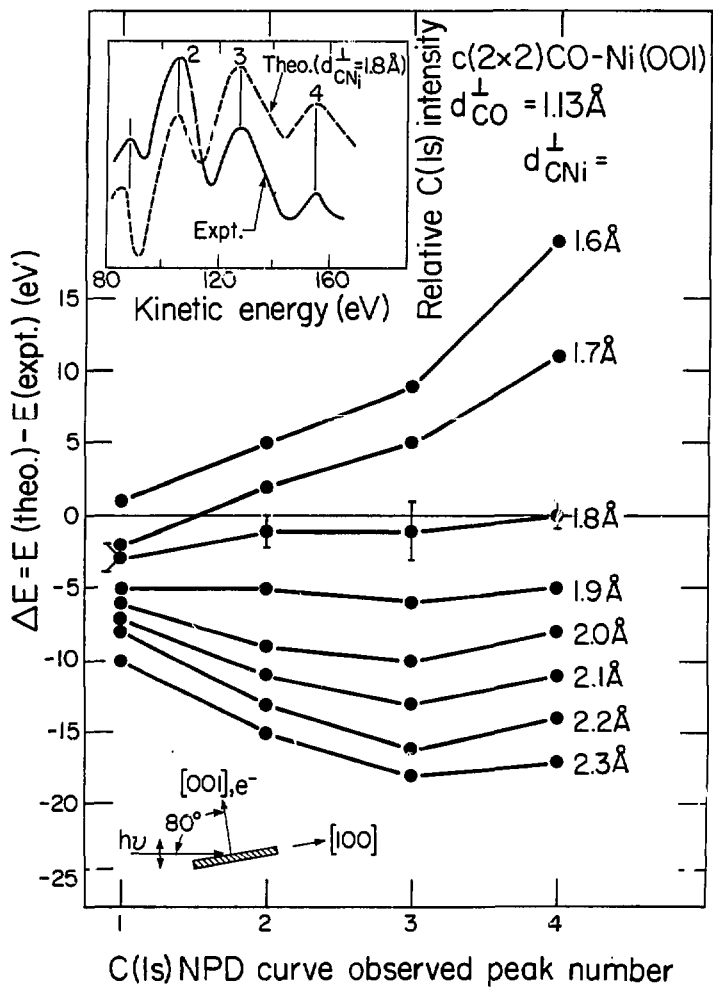


Fig. 1

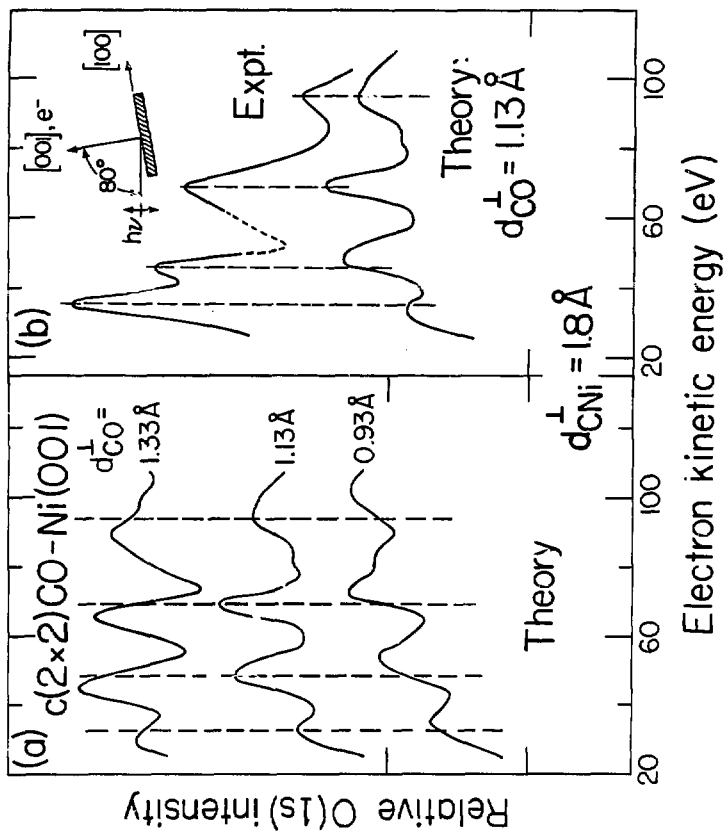


Fig. 2

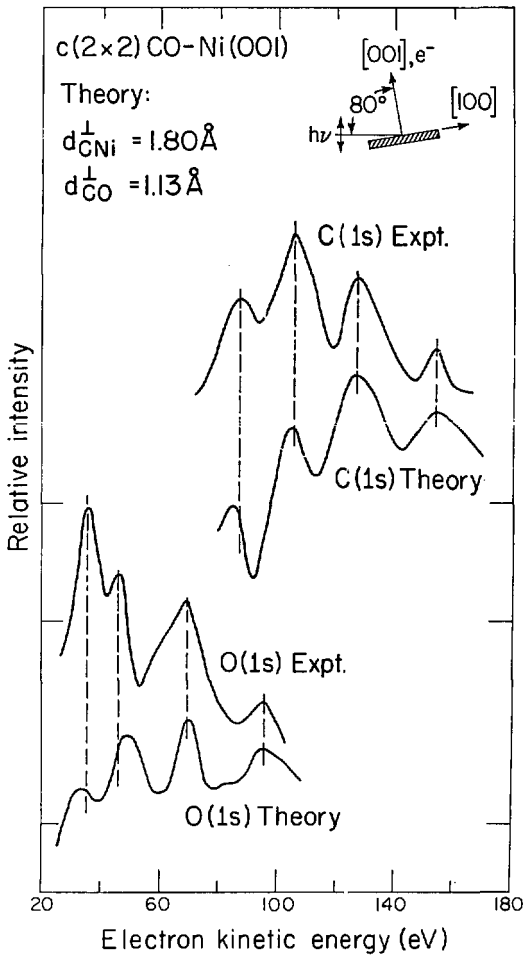


Fig. 3

XBL8112-12057

VIII. CONCLUDING REMARKS

A. RECOMMENDATIONS FOR THE FUTURE: ELECTRON ENERGY LOSS SPECTROSCOPY

In this section, I will propose some general guidelines which should be considered in the design of future EELS spectrometers. This will be followed by more specific suggestions for improving our own spectrometer. Finally, there will be a discussion of the future of EELS from a scientific standpoint.

It is clear that the main shortcoming of EELS is its relatively low resolution in comparison to photon-based infrared spectroscopy. Future spectrometer improvement should concentrate on improving the FWHM resolution to less than 10 cm^{-1} and substantially reducing the number of background electrons in the low frequency region ($< 500 \text{ cm}^{-1}$). Many spectrometers have extremely low background signal above 500 cm^{-1} , so there is not much need for improvement in that region. At the present time, a great deal of vibrational information is hidden in the background of the inelastic tail of hundreds of spectra in the literature.

The following list of guidelines should be considered in the design of a new spectrometer:

(1) Resolution. The 180° hemispherical sector should be used for all energy selectors due to its superior resolution characteristics: There should be a dramatic increase in the size of the sectors used. Most current spectrometers utilize 127° cylindrical sectors or 180° hemispherical sectors with mean radii of 2-4 cm. This could be increased to 10-15 cm, resulting in about a factor of five increase in

theoretical resolution. This will be necessary if second generation spectrometers are to operate at considerably less than 1 meV or 8 cm^{-1} FWHM resolution. The use of such large sectors will create severe space and mobility problems in current vacuum chambers. One solution would be to build a cylindrical vacuum chamber which has a stationary lower part and a rotatable upper section, separated by a differentially pumped teflon o-ring seal. This type of rotatable seal is now commercially available.¹ Experimental rotations could be accomplished by mounting the analyzer on a flange in the rotatable section and the monochromator in the stationary section. The sectors would be quite large, so they could be housed in separate chambers outside of the main chamber. Almost all the motion required to do an experiment would be supplied by the chamber itself. Fine adjustment of the beam location could be accomplished with small linear translations of the analyzer and with electrostatic deflection lenses during tuning up. Elimination of most of the analyzer and monochromator motion with respect to their mounting flanges would remove problems brought on by the use of springs, sliding contacts, dangling wires, etc.

(2) Background. The background of scattered electrons in the low frequency region must also be reduced substantially over current designs. This can be accomplished primarily by using both a double monochromator (pre-monochromator and monochromator in tandem) and a double analyzer. The use of pre-filters has been very successful in the past.^{2,3} Using the rotatable chamber setup described above, the double sectors could both have their own auxiliary housings, with only their

zoom lenses penetrating into the main chamber. Another method of reducing background (by as much as a factor of 10) is to cut a blazed groove pattern into the sectors themselves.^{4,5} These grooves will reflect scattered electrons back towards the direction in which they came, ensuring that most of them will never reach the detector. In addition, all optical surfaces should be coated with graphite, to reduce scattering by lenses and slits. Improvements in lens design which lead to better collimation and smaller beam pencil angles should also produce a lower background.

(3) Sensitivity. Large improvements in sensitivity can be obtained by using the multichannel detection scheme presently being used in several photoelectron spectrometers.^{2,6} Multichannel detection would allow one to acquire an EELS spectrum of a good part of the entire infrared region simultaneously, leading to a potential improvement in sensitivity by a factor of 10-100. The capability to accumulate an entire spectrum without scanning would also simplify the tuning process considerably.

(4) Construction. More care must be taken to shield stray electric and magnetic fields in a sub-1-meV-resolution spectrometer. No stainless steel or other permeable material should be used in the spectrometer regions. All mumetal shielding should be as far away from the electron path as possible. If possible, the entire vacuum chamber should be completely surrounded by a set of shields.

Unfortunately, many of these guidelines can not be easily incorporated into our present design. There are, however, several improvements which will not require major alterations to our spectrometer.

The following is a discussion of possible improvements:

(1) Resolution. There is certainly room to improve the FWHM resolution of the spectrometer. Its current sensitivity is quite high, so count rate could be traded for resolution by reducing the slit size on all hemispherical sectors. Better resolution could also be obtained by running at lower pass energies than those currently used. It is uncertain how much further resolution would improve, however, as our energy selectors do not seem to disperse theoretically at pass energies less than 1 eV. An effort should be made to better understand the causes of this non-ideal behavior. This problem may be partially attributed to the lack of adequate field termination at the entrance and exit planes of the three 180° hemispherical sectors (two in the monochromator, one in the analyzer). At present, only one of these six termination planes has field termination electrodes. These could be installed in all locations without great difficulty. Unfortunately, it will be nearly impossible to increase the size of the hemispherical sectors (as suggested above) due to physical constraints imposed by our current vacuum chamber.

(2) Background. The background of scattered electrons may be reduced in a number of ways. The most ambitious improvement would be to install a pre-analyzer before the analyzer. The design of the pre-analyzer could be similar to that of the analyzer, and their combined assembly could be modeled after the monochromator assembly. Due to the position of the carriage track, which provides the vertical motion of the existing analyzer, it is now impossible to install another 180° hemispherical sector. If the vertical motion capability were modi-

fied, however, a pre-analyzer could be installed. The current vertical motion could be replaced by a mechanism which confines the analyzer to the region of EELS horizontal plane but allows for small translations above and below that plane. This would not affect the EELS capabilities of the analyzer. A second improvement would be the machining of sawtooth grooves^{4,5} in the hemispherical sectors to reject electrons hitting the hemispherical surfaces. Sawtooth patterns can be routinely machined in cylinders, but hemispheres present a more difficult technological challenge, so the job will probably require a computer-controlled machine. Lens improvements should also reduce the background. All lenses which determine the pencil angle of acceptance of hemispherical sectors should meet the Kuyatt and Simpson criteria. This requires that an angle-defining aperture be installed in the C (analyzer) lens (see Chapter II). The background will also be reduced if a lens is installed between the analyzer exit slit and the electron multiplier. This lens will reduce the count rate but ensure that all electrons counted by the multiplier will have left the analyzer with a very small pencil angle. It is less likely that an electron has been scattered by the optics if it meets this pencil angle requirement. As an alternative to placing a lens before the multiplier, a minor modification could be made to the present double exit slit setup. This would involve moving the second exit slit to a position 2 mm behind the first slit, which would reduce the maximum pencil half-angle to 7° . In addition, the second slit could be biased at a more negative potential than the first, leading to further rejection of unwanted electrons.

(3) Sensitivity. The sensitivity of the spectrometer is high at present, although steps taken to improve the resolution and background may lower it to less than desirable levels. The count rate is currently limited by the Spiraltron electron multiplier, which will suffer reduced gain if operated above 50-100 kHz. This limit could be raised by at least a factor of five by switching to a high-current Channeltron (Galileo 4816). In the future, it may be necessary and desirable to switch to a multichannel detection scheme. We have tried a multichannel position-encoder,⁶ made up of dual microchannel plates and a resistive anode, in place of the single channel detector currently installed. The main problems with the multichannel detector were that the background was considerably higher, the linearity (positional accuracy) was poor, and the speed of the electronics (5 μ sec per count) limited the count rate over the entire detector to less than 10 kHz, much too low for EELS. The background problem in multichannel detection may be circumvented by the use of a pre-analyzer² and the machining of grooves in the hemispheres. The linearity and speed limitations can be overcome by using a new wedge-and-strip metal anode⁷ in place of the resistive anode. This metal anode and associated fast electronics (0.5 μ sec per count) should make the maximum count rate comparable to that of single channel detection. A metal anode designed for our spectrometer has been fabricated and awaits testing.

(4) Construction. The task of removing the analyzer from the vacuum chamber is extremely difficult and risky because the analyzer carriage track comes within a few mm of the knife edge of the chamber

bottom flange. If the modified vertical motion discussed above were installed, this would no longer pose a problem. At present, there are a few remaining holes and gaps in the mumetal shielding around the outside of the vacuum chamber which should be eliminated. To further reduce the amount of permeable material in the spectrometer, stainless steel should be replaced with OFHC copper wherever possible.

(5) Miscellaneous. The base pressure of the vacuum chamber may be improved by the addition of a liquid helium cryopump which has been purchased but not utilized. The cryopump pumps many gases faster than the ion pump does, and would be especially useful for pumping out argon after sputtering and adsorbate gases during dosing. Also, our liquid nitrogen cooling mechanism, which has been built and tested, should be installed on our sample manipulator.

Despite all of the suggested improvements, the present state of the spectrometer is satisfactory and should enable a number of interesting experiments to be carried out in the future. These experiments should be designed with the advantages of EELS over competing techniques in mind. For example, EELS can usually distinguish the presence of more than one adsorbed state on the surface. This fact points to studies of multiple adsorption site overlayers, surface oxide nucleation, and adsorbates bonded to stepped or kinked crystals. The vibrational spectroscopy of adsorbates on semiconductor surfaces not well known, especially with regard to hydrogen chemisorption.⁸ Another relatively untouched area is off-specular scattering. Very few impact scattering modes have been observed to date.⁹ Theoretical predictions¹⁰ concerning the usefulness of these modes for determin-

ing surface structure have not yet been experimentally verified. Studies of heavy atom adsorption, such as metal or semiconductor overlayers adsorbed on metal surfaces, might also be fruitful if carried out on an EELS spectrometer with extremely low background in the low frequency region of the spectrum.

B. RECOMMENDATIONS FOR THE FUTURE: PHOTOELECTRON DIFFRACTION

Since our group is essentially unique in having the only ongoing experimental research effort in energy-dependent photoelectron diffraction (EDPD), discussions of the future of the technique and of the future of our group's effort will have a great deal of overlap. With this in mind, I present some thoughts on the EDPD technique.

The rapid development of Fourier-transform PD and the discovery that PD is sensitive to (adsorbate atom)/(substrate atom) distances instead of perpendicular layer spacings have been the most significant theoretical advances made since the experiments described in this thesis were carried out.^{11,12} The use of FTPD will free the experimenter from his reliance on multiple scattering calculations. It will also significantly improve the structural accuracy of PD because the analysis may be done along several emission angles, each of which yields the distance from the adsorbate to a different substrate atom. A more quantitative understanding of the backscattering phase shift function will improve the accuracy of the technique even further.

Experimental advances have occurred equally as fast. The most serious problems incurred in making the measurements described in this thesis can be directly attributed to the grasshopper monochromator on

Beam Line I-1 at SSRL. The photon beam delivered by this line suffers from low flux (especially near the carbon K-edge), poor resolution, and a high percentage of scattered light. These problems prohibited us from making EDPD measurements over a wide enough energy range to use Fourier-transform analysis to obtain a high degree of accuracy. Many of the problems of the grasshopper are not present in the newer JUMBO monochromator, on Beam Line III-2 at SSRL.¹³ Barton et al. have been able to take extended (400 eV wide) kinetic energy range intensity-energy (IE) curves of the S(1s) level on this beam line.¹² The JUMBO monochromator is not presently able to provide photons below 800 eV, so that the near K-edge region of C, N, O, and F cannot be accessed. To carry out successful FTPD experiments on adsorbates containing these low-Z elements, we must look to new monochromators in the 250-1000 eV photon energy range. A promising candidate for these studies is the vacuum ultraviolet (VUV) branch of the EXXON-LBL beam line to be built at SSRL. Because the VUV monochromator on this line will be of the double grating type, it is expected to have properties similar to JUMBO, i.e. high flux and high resolution over a wide energy range.

Using new synchrotron beam lines, FTPD experiments on molecular adsorbates such as CO, NO, CO₂, O₂, CH₃O, and hydrocarbons should be possible. Multiple-carbon hydrocarbons present a significant challenge because C(1s) emission will originate from more than one location on each adsorbed molecule. The acquisition of many IE curves at different emission angles may be able to circumvent this problem,

especially in the case of a two carbon molecule such as ethylene or acetylene.

Structural determination of semiconductor surfaces is another possibility for future FTPD study. Semiconductor surfaces are more open than metal surfaces, due to larger bond distances. Therefore, the size of PD oscillations should be large if data is collected close to directions in which the emitter atom and a nearby scatterer line up, but may be very small at other emission angles. We have observed the latter in the form of a negative PD result for GaAs(110).¹⁴ IE curves of the Ga(3d) and As(3d) levels were measured at normal emission from a GaAs(110) single crystal which exhibited a sharp LEED pattern. Virtually no oscillatory structure was observed in either of the IE curves. This can be understood by recognizing that there are no nearby scatters directly below the top Ga layer or top As layer atoms in GaAs(110). If data were collected at well-chosen off-normal emission angles, we would expect to see substantial PD oscillations. A number of experiments on clean and adsorbate covered semiconductor surfaces could be carried out in this fashion.

In closing, I would like to give an indication of how far photoelectron diffraction has come in the last four years. Table I lists all of the PD experiments in which I participated during the period from 1978 thru 1980. Note that all of the systems listed but one were studied with NPD only. During that time period, it was believed that normal emission (NPD) data were considerably more useful than off-normal data. However, more recent work by other Shirley group members has shown that it is advantageous to obtain data at selected off-nor-

mal angles. They have added to the list of systems explored by PD with a study of the S(1s) core level in sulfur adsorbed on Ni(001) and on Cu(001).¹² In that work, Fourier-transform analysis provided the entire basis for the structure determination. In the coming years, the list should continue to grow as PD is applied to new adsorbate/substrate systems, including those with core levels other than the C(1s), O(1s), S(1s), S(2p), and Se(3d).

REFERENCES

1. Thermionics Laboratory, Inc., Hayward, CA
2. J. E. Pollard, D. J. Trevor, Y. T. Lee, and D. A. Shirley, Rev. Sci. Instrum. 52, 1837 (1981); J. E. Pollard, Ph.D. thesis, University of California, Berkeley, 1982, unpublished.
3. S. Lehwald, H. Ibach, and J. E. Demuth, Surf. Sci. 78, 577 (1978).
4. H. Froitzheim, H. Ibach, and S. Lehwald, Rev. Sci. Instrum. 46, 1325 (1975).
5. L. H. Dubois, Ph.D. thesis, University of California, Berkeley, 1980, unpublished.
6. S. D. Kevan and D. A. Shirley, Phys. Rev. B 22, 542 (1980); S. D. Kevan, Ph.D. thesis, University of California, Berkeley, 1980, unpublished.
7. C. Martin, P. Jelinsky, M. Lampton, R. F. Malina, and H. O. Anger, Rev. Sci. Instrum. 52, 1067 (1981).
8. L. H. Dubois and G. P. Schwartz, Phys. Rev. B 26, 794 (1982).
9. W. Ho, R. F. Willis, and E. W. Plummer, Phys. Rev. B 21, 4202 (1980); J. A. Gates and L. L. Kesmodel, J. Chem. Phys. 76, 428 (1982).
10. S. Y. Tong, C. H. Li, and D. L. Mills, Phys. Rev. Lett. 44, 407 (1980); Phys. Rev. B 21, 3057 (1980), Phys. Rev. B 24, 806 (1981).
11. J. J. Barton and D. A. Shirley, 1982, unpublished.
12. J. J. Barton, C. C. Bahr, Z. Hussain, S. W. Robey, J. G. Tobin, L. E. Klebanoff, and D. A. Shirley, 1982, unpublished.

13. Z. Hussain, E. Umbach, D. A. Shirley, J. Stohr, and J. Feldhaus,
Nucl. Instrum. Methods 195, 115 (1982).
14. This work is unpublished.

Table I. Partial list of systems studied by NPD

SYSTEM	LEVEL	SITE
c(2x2)CO-Ni(001)	C(1s),O(1s)	Top, $d_{\text{CNi}}^{\perp} = 1.80 \text{ \AA}$, $d_{\text{CO}}^{\perp} = 1.13 \text{ \AA}$
$(\sqrt{3} \times \sqrt{3})R30^{\circ}$ CO-Ni(111)	C(1s),O(1s)	Bridge, $d_{\text{CNi}}^{\perp} = 1.27 \text{ \AA}$, $d_{\text{CO}}^{\perp} = 1.13 \text{ \AA}$
c(2x2)O-Ni(001)	O(1s)	Hollow, $d_{\perp} = 0.85 \text{ \AA}$
c(2x2)O-Cu(001)	O(1s)	Hollow, $d_{\perp} = 0.80 \text{ \AA}$
$(\sqrt{2} \times \sqrt{2})$ O-Cu(001)	O(1s)	Hollow, $d_{\perp} = 0.80 \text{ \AA}$
c(2x2)S-Ni(001)	S(2p)	Hollow, $d_{\perp} = 1.30 \text{ \AA}$
c(2x2)S-Ni(011)	S(2p)	Hollow, ($d_{\perp} = 0.94 \text{ \AA}$) OR Top ($d_{\perp} = 2.20 \text{ \AA}$)
p(2x2)Se-Ni(001)	Se(3d)	Hollow, $d_{\perp} = 1.55 \text{ \AA}$
c(2x2)Se-Ni(001) (annealed)	Se(3d)	Hollow, $d_{\perp} = 1.55 \text{ \AA}$
c(2x2)Se-Ni(001) (unannealed)	Se(3d)	Hollow, $d_{\perp} = 1.65 \text{ \AA}$
c(2x2)Se-Ni(001) OFF-NORMAL PD	Se(3d)	Hollow, $d_{\perp} = 1.55 \text{ \AA}$
Disordered Se-Ni(001) (low coverage)	Se(3d)	Hollow, $d_{\perp} = 1.55 \text{ \AA}$
c(2x2)Se-Ni(011)	Se(3d)	Hollow, $d_{\perp} = 1.10 \text{ \AA}$
p(2x2)Se-Ni(111) (annealed)	Se(3d)	Hollow (vacancy below), $d_{\perp} = 1.80 \text{ \AA}$
p(2x2)Se-Ni(111) (unannealed)	Se(3d)	Hollow ($d_{\perp} = 1.80 \text{ \AA}$) AND Top ($d_{\perp} = 2.30 \text{ \AA}$)
$(\sqrt{3} \times \sqrt{3})R30^{\circ}$ Se-Ni(111)	Se(3d)	Multiple sites
Disordered Se-Ni(111) (low coverage)	Se(3d)	Hollow (vacancy below), $d_{\perp} = 1.80 \text{ \AA}$

ACKNOWLEDGEMENTS

The most important people in my life for the past five years, as well as the previous twenty-one, have been my parents, Minna and Sidney Rosenblatt. Without their love and support, this work could never have been accomplished. The emotional closeness I feel towards them helps to overcome the large physical distance between us, and I dedicate this thesis to them.

The other members of my family have also been quite supportive during my graduate career. In particular, I wish to thank my two brothers, Joshua and Richard, and all of the Goldmans, who are my only relatives in California.

I wish to acknowledge a number of people in the Chemistry Department at Berkeley. First of all, I thank my research director, Dave Shirley, for his guidance and support of my work. Albert Baca has been my co-worker on the EELS project for the past three years and deserves a great deal of credit for the progress we have made. It has been a great pleasure to work with Albert and to share his insights. Dennis Trevor was extremely helpful and generous with his brilliant ideas about virtually any topic. Steve Kevan deserves credit for teaching me a great deal about photoemission and experimental science in general.

All of the photoelectron diffraction work in this thesis was carried out in collaboration with others. Many long hours were spent at Stanford with Steve Kevan, Rich Davis, Gary Mason, Jim Tobin, and Dave Denley. I thank them for their patience with me under those stressful

conditions. Many thanks go to Dave Tong at the University of Wisconsin, Milwaukee, with whom I have carried on a long collaboration.

There is a long list of graduate students who were not scientific collaborators but who have been my friends as well as my mentors during all or part of the last five years. This list includes Jim Pollard, Steve Southworth, Carlton Truesdale, Chris Parks, Paul Kobrin, Dennis Lindle, Lennie Klebanoff, Steve Robey, John Barton, Charlie Bahr, Janice Reutt, Phil Heimann, Trish Ferrett, and John Crowell.

Many members of the support staff at LBL made important contributions to my work. Wini Hepler and Barbara Moriguchi have been very helpful in many ways and have made the atmosphere in our lab very pleasant. Joe Katz and Don Malone were indispensable due to their contributions in the areas of electrical and mechanical engineering, respectively. Their help has been crucial to the functioning of the EELS spectrometer. Other valuable support was provided by Charlie Taylor, Bert Watkins, Larry Ornelas, John Anderson, and Ed Voronin of the Mechanical Shops, Dick Escobales and Warren Harnden of Mechanical Engineering, and Richard Whiteman and Richard Strudwick of Electrical Engineering.

Many people in the Technical Information Department of LBL deserve credit for the production of this thesis. Most notable among these are Mirriam Schwartz and John Flambarb of Technical Illustration and June DeLaVergne, Jean Wolslegel, Connie Silva, Diana Morris, and Shirley Ashley of Word Processing. Whatever anyone may think of this thesis, he or she has to admit it looks pretty!

Finally, I must thank the many close friends who helped me overcome the last five years: Danny Ruberman, Ann Borst, Tom Tufano, Helen Schwartz, Kent Olson, Bob Connell, Peter-Lu Abbey, Mike Scarano, Stuart Sechrest, Robert and Ruth Katz, Mike and Dana Cable, Carol Zettas, Gerald Katz, and Pete Lawrence. And special thanks to Alfred E. Newman, for his words of wisdom: "What me worry!"